THE UNIVERSITY OF OKLAHOMA HEALTH SCIENCES CENTER

GRADUATE COLLEGE

CHARACTERIZATION OF 3D PRINTING MATERIALS FOR USE IN RADIATION THERAPY

A THESIS

SUBMITTED TO THE GRADUATE FACULTY

in partial fulfillment of the requirements for the

degree of

MASTER OF SCIENCE

BY

REGAN JANAE HIME

Oklahoma City, Oklahoma

2020

APPROVED BY:

_____

_____

_____

_____

_____

_____

ACKNOWLEDGMENTS

I have many people I would like to thank. First and foremost, thank you to my thesis advisor, Dr. Rutel, for taking me as a student. I could not have asked for a better mentor and person to guide me through this process. Thank you for always being available for my broken wires, questions, and concerns, and for encouraging me and believing in me when the process got frustrating.

I also want to thank my committee members. Dr. Johnson, thank you for helping me get the ball rolling on my project and teaching me the art of 3D printing. Dr. Chen, thank you for taking the time out of your busy schedule to help me make my photon measurements.

I had so many people support me through my thesis process. I would like to thank my mentor, Dr. Sonnad, for the encouragement and advice. Thank you for keeping up with my progress, and making sure things kept moving. Thank you to Dr. Jin, Zach Richards, and Mark Newpower for helping with measurements. And thank you to my husband, Brock, for the support through the entire process. I could not have finished without the great support system I was blessed with having.

TABLE OF CONTENTS

LIST OF TABLES

LIST OF FIGURES

LIST OF FIGURES CONTINUED

LIST OF FIGURES CONTINUED

CHAPTER I

INTRODUCTION

Additive manufacturing is the category of technologies which produce physical objects layer by layer from three-dimensional Computer-Aided Design (3D CAD) data [1]. The CAD data can be derived from the volumetric digitization of an object, and can be subsequently modified on a computer to create a CAD model. 3D printing, also known as additive manufacturing, uses the CAD data to physically create the object layer by layer [2]. Bill Masters was the first to generate an object using 3D printing [3]. The first patent in 3D printing was obtained by Charles Hull in 1986 [4]. As many of the initial patents expire [5], 3D printing is an increasingly viable and cost effective means of production, becoming a topic of research in many fields of study.

Starting in the early 1990s with the creation of skeletal models for surgical preparation and rehearsal using patient computed tomography (CT) and magnetic resonance imaging (MRI) scans, 3D printing is increasingly being used in the medical field. 3D printing has been used to fabricate dental prosthesis and tooth models used for casting, as well as the production of patient specific surgical implants [6, 7]. In the field of radiation oncology, 3D printing is becoming more commonplace, as some facilities find it can be a cost-effective alternative to traditionally vendor-sourced products.

Patient-specific boluses have been created using 3D printing for both photon and electron beam therapy [8-11]. Customizing boluses using 3D printing allows for fewer air gaps between device and patient, boluses of differentiated thicknesses, and can aid in the reproducibility of patient positioning [11]. Fujimoto et al. (2017) examined the efficacy

and accuracy of 3D printing techniques as a viable option for creating patient-specific boluses against those commercially available and found their performance to be comparable [12]. Zou et al. (2015) compared a 3D printed electron bolus and proton compensator against those manufactured via the alternative milling method. They demonstrated that 3D printed objects could be created with an increased accuracy over those generated through milling, as the physical size of the cutting bit determines the dimensional accuracy; however, samples created via fused deposition modelling (FDM) printing did show material inhomogeneities resulting in dose perturbations unwelcome in proton therapy [13]. Mouthpiece fixation and other immobilization devices have also been manufactured using 3D printing [14-16]. One study found negligible differences in patient position and dose distribution accuracy between 3D printed mouthpieces and those created by traditional means [14].

In brachytherapy, the 3D printing of personalized gynecological applicators allows for optimal fit and distribution of interstitial needles, especially for patients whose anatomies are not conducive for commercial applicators [17-19]. Sethi et al. (2016) fabricated personalized applicators using a biocompatible, sterilizable material for three patients: one with a vaginal canal too small for the smallest commercially available applicator, one with a vaginal canal in-between available applicator sizes, and one too wide. The applicators enabled adequate target coverage and normal tissue sparing, and the fabrication process was smoothly adapted into the clinical workflow [19].

The fabrication and customization of radiographic phantoms can also be implemented using 3D printing. This can be accomplished at a fraction of the cost and with a higher degree of physical complexity than those commercially available. In addition

to phantoms being produced for image quality testing [20-23], phantoms have also been printed for specific use in radiation therapy including: patient specific dosimetry quality assurance [24]; treatment delivery comparisons between phase-gated and amplitude-gated volumetric modulated arc therapy (VMAT) [25]; accuracy checks for stereotactic radiosurgery systems [26]; and a full-scale patient analog by Craft and Howell (2017) for use in various clinical and research applications [27].

Although work has been done to characterize 3D printing materials radiographically, the availability and variety of materials is ever-expanding. With this increase in the amount of materials that can be 3D printed, and the number of modalities with which to use them, the task of material selection becomes non-trivial. With regards to physical attributes, the density of the material is a key characteristic in determining how a material responds to x-ray imaging. Many investigators have examined printed materials using CT, and while there is much agreement between results, fewer studies focus specifically on radiation therapy modalities. To best use 3D printing materials clinically in radiation therapy, they must first be characterized for the treatment modality in which they are to be applied. Treatment planning system commissioning includes characterizing specific treatment beams under reference conditions, typically via direct measurements of ionization and dose within a water tank. This commissioning data is used to extrapolate predictions for scenarios which differ from the reference conditions. In order to clinically implement new 3D printing materials, knowing the response of the treatment beam for these materials is essential. As the Hounsfield unit (HU) [Equation 2.1] value of a material has a direct relationship to the electron density the material,

treatment planning systems use CT data to calculate dose to various materials more accurately [28].

The goal of our investigation is to characterize materials, for potential for use, in radiation therapy by determining their response to clinical electron, photon, and proton treatment beams and CT imaging. Each material will undergo a CT scan prior to being 3D printed into standard blocks; a subsequent CT of each block will permit pre- and post-printed comparisons. The materials will be characterized for electron beams via percent depth dose (PDD) curve; for photon beams, the materials will be characterized by a tissue-maximum ratio (TMR) comparison relative to commercially available *Plastic Water*® [29]; and for proton beams, the materials will be characterized by determining their water equivalent relative-stopping-power. For each respective modality, the geometry and setup conditions of the water measurements and material measurements will be unchanged. In this way, the materials' response relative to water will be substantiated, as results can be extrapolated to other setup conditions for the given treatment beam. Through these measurements, the response of these materials will be characterized for future clinical use, increasing the efficiency of clinical implementation, and may increase modeling accuracy within treatment planning systems.

CHAPTER II

BACKGROUND

Treatment Beam Modalities

In the modern medical linear accelerator, electrons are generated through thermionic emission in an electron-gun x-ray tube via the high-voltage radiofrequency (RF) pulse-excited cathode. The electrons are accelerated past the anode by an electromagnetic field and into a waveguide. The waveguide derives its power from a klystron radiofrequency generator/amplifier. RF pulses are sent into the accelerating waveguide. The electrons interact with the electromagnetic field induced by the RF waves within the waveguide, and are accelerated, gaining energy via a sinusoidal electric field oscillation. The high energy electrons exit the accelerator tube as a 3 mm narrow cone-shaped pencil beam with an energy ranging between 4 and 20 MeV. This beam is subsequently bent and focused using a 270° bending magnet system before exiting the treatment head. As the beam passes through the treatment head, the beam passes through primary collimators and a scattering foil composed of a high-Z material in order to spread the beam uniformly across the treatment field. The electron beam is additionally shaped by secondary collimators and a scatter-reducing 'electron cone', which defines the effective treatment field size. Additional electron aperture blocks placed within the 'cone' define the clinical treatment field on the target surface [30]. A schematic is shown Figure 2.1, B.

Photon beams are produced in the same fashion as electron beams until their exit from the treatment head. At this point, the electron beam strikes a target composed of a high-Z material in order to produce a forward-peaked poly-energetic photon beam through Bremsstrahlung interactions. The beams made available have a maximum energy typically ranging between 4 and 18 MV in radiation therapy. The photon beam then passes through a primary collimator and a flattening filter in order to generate a more uniform intensity across the field. The beam is further shaped by secondary collimators, including multi-leaf collimators (MLCs), before incidence upon the target surface [30]. A schematic is shown in Figure 2.1, A.

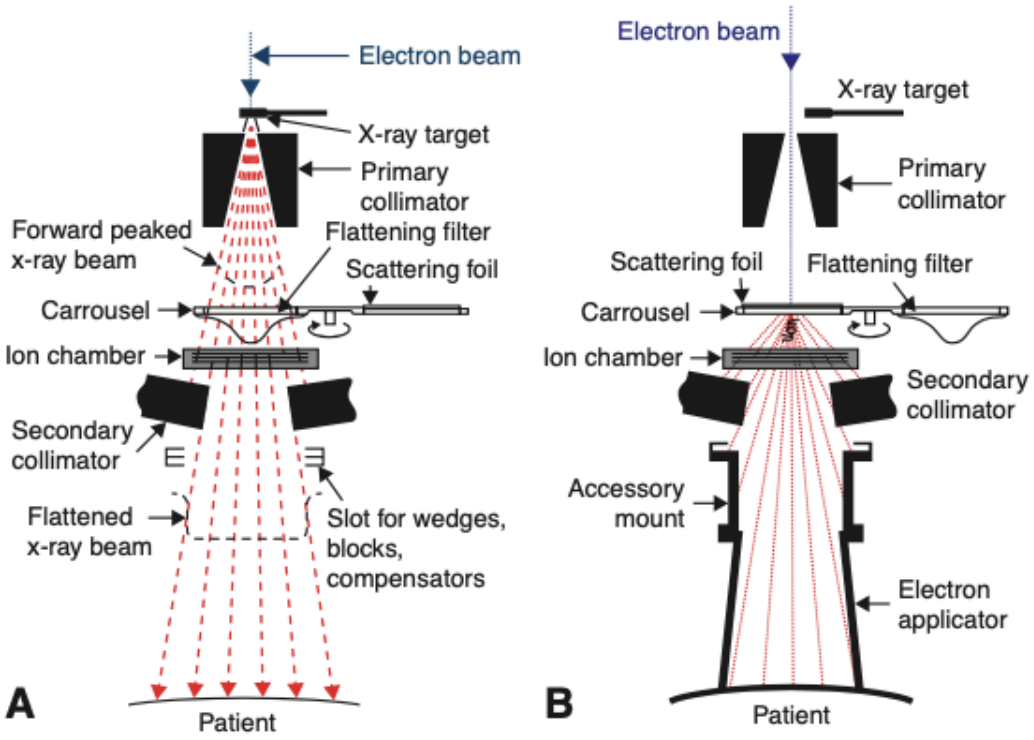

Figure 2.1: Schematic showing the beam-line components of (A) a photon treatment setup and (B) an electron treatment setup within a typical medical linear accelerator. The details of beam production are presented in the text above. Note: relative component size and position are not to scale. (Republished with permission of C.J Karzmark and Robert Morton, from A Primer on Theory and Operation of Linear Accelerators in Radiation Therapy, Karzmark, 2nd edition, 1998, permission conveyed through John Wiley and Sons) [30].

The traditional accelerating source of proton beams in radiotherapy is an isochronous cyclotron. The cyclotron is composed of a strong RF system, which produces an oscillating electric field of constant frequency, and a strong magnetic field to continuously accelerate the protons in a spiral trajectory as the magnetic field strength increases with increasing radius. The protons are initially generated within the center of the cyclotron by ionizing hydrogen gas. The protons then enter the cyclotron and are accelerated as the particles pass across the *Dees*, gaps accelerating the particles via electric field. The spiral pattern continues until the particles reach the electro-static deflector that extracts the protons at a fixed energy, typically between 230 and 250 MeV for general clinical use. A schematic is shown in Figure 2.2. Within many commercial systems, the proton beam is then transported in vacuum via beamline to the proton delivery system. In a pencil-beam-scanning proton system, the beam is transmitted through a range modulator to modify the beam energy and range, and two pairs of perpendicular dipole magnets steer the beam across the target [31].

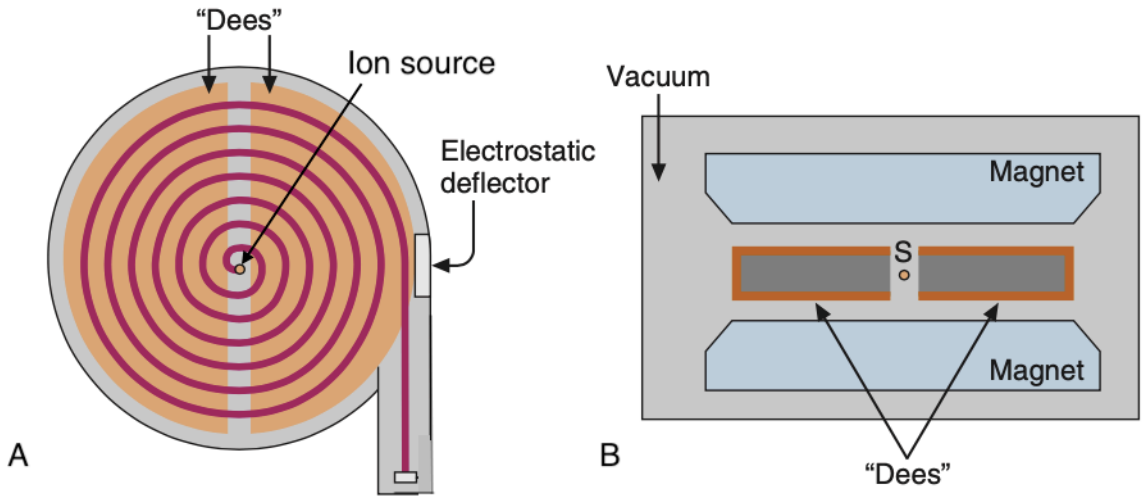

Figure 2.2: A schematic of a proton producing cyclotron from (A) the top view and (B) the side view. (Republished with permission of Saunders, from Physics in Nuclear Medicine, Cherry et al., 5th edition, 2012, permission conveyed through Copyright Clearance Center, Inc.) [32].

Computed Tomography (CT) and Hounsfield Units (HU)

CT is the most commonly used imaging modality in radiation therapy [28]. In CT, a diverging x-ray beam between 20 to 150 keV penetrates the patient being imaged. Within this energy range, photoelectric and Compton scattering dominate the x-ray interactions within the patient. Based on the attenuation properties of the tissues, varying amounts of radiation are transmitted through the patient to the detector. The x-ray beam rotates about the patient as the patient is longitudinally moved through the bore to acquire data from multiple angles. Images are created from the collected data via reconstruction algorithms, creating 2D trans-axial slices across the 3D imaged region. The gray scale value assigned to each pixel in the resulting images are called CT numbers, determined by the calculated linear attenuation coefficient. Typically, CT numbers are normalized to a scale by setting the CT number of air to -1000 and water to 0. A CT number normalized in this way is called the Hounsfield unit (HU), defined by

$$HU = 1000\, x \frac{(\mu_x - \mu_w)}{\mu_w}, \tag{2.1}$$

where μ_x is the linear attenuation coefficient of the given tissue, x, and μ_w is the linear attenuation coefficient of water, w. HU values can be calibrated to known equivalent electron density values for a given tissue due to the approximately linear relationship [28, 30].

Percent Depth Dose (PDD), Tissue-Maximum Ratio (TMR), and Relative Stopping Power (RSP)

PDD curves are used to characterize how dose changes with depth in a medium relative to the maximum dose. These curves generally represent the normalized dose

distribution versus depth along the central axis of the beam at a fixed source-to-surface distance (SSD). PDD is defined as

$$PDD = \frac{D_d}{D_{d_0}} \, x \, 100\%, \tag{2.2}$$

where D_d is the absorbed dose at any depth within a material, *d*, and D_{d_0} is the absorbed dose at a reference depth, d_0, typically the depth of maximum dose, d_{max}. Beyond the depth of maximum dose, PDD values increase with an increase in beam energy, SSD, and field size [30]. The SSD setup used to calculate PDD is shown in Figure 2.3.

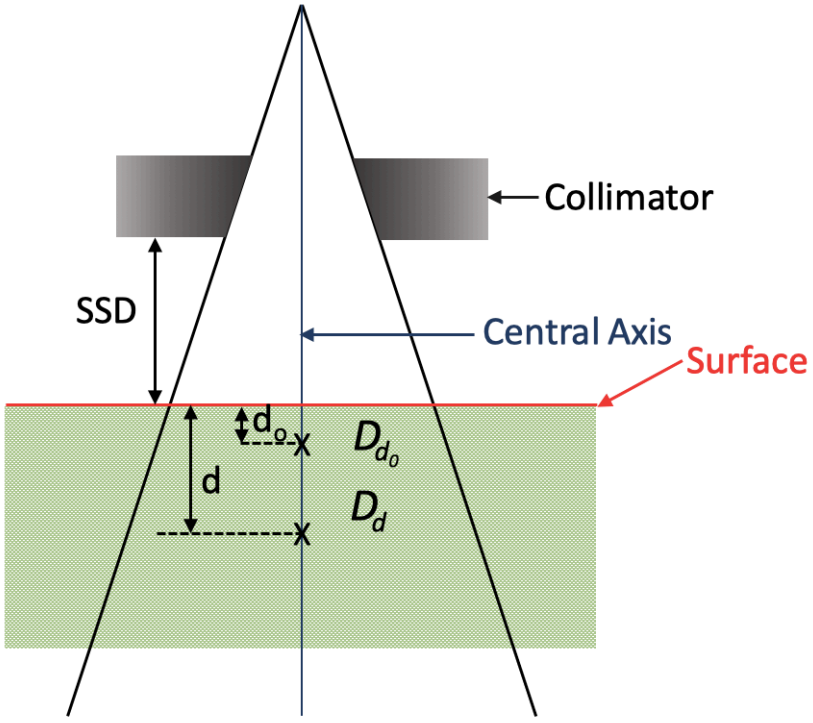

Figure 2.3: PDD variables using SSD setup. (Inspired by [30].)

TMR curves are used to characterize dose distributions by making measurements at a fixed position in a phantom within a source-to-axis distance (SAD) setup along the central axis of the beam. In this way, as the depth of the detector increases, the SSD

decreases, removing from the data a dependence on the distance between the source and detector. TMR is defined as

$$TMR = \frac{D_d}{D_{d_{max}}}, \tag{2.3}$$

where D_d is the absorbed dose at a given depth in a phantom, and $D_{d_{max}}$ is the absorbed dose at the depth of maximum dose. TMR increases with field size and beam energy and, as mentioned above, has no inverse-square law dependence [30]. The SAD setup used to calculate TMR is shown in Figure 2.4. TMR and PPD are related by the equation

$$TMR(d, r_d) = \frac{PDD(d, r, SSD)}{100}\left(\frac{SSD + d}{SSD + d_{max}}\right)\left(\frac{S_p(r_{d_m})}{S_p(r_d)}\right), \tag{2.4}$$

where $S_p(r_{d_m})$ and $S_p(r_d)$ are phantom scatter factors for given field sizes [30].

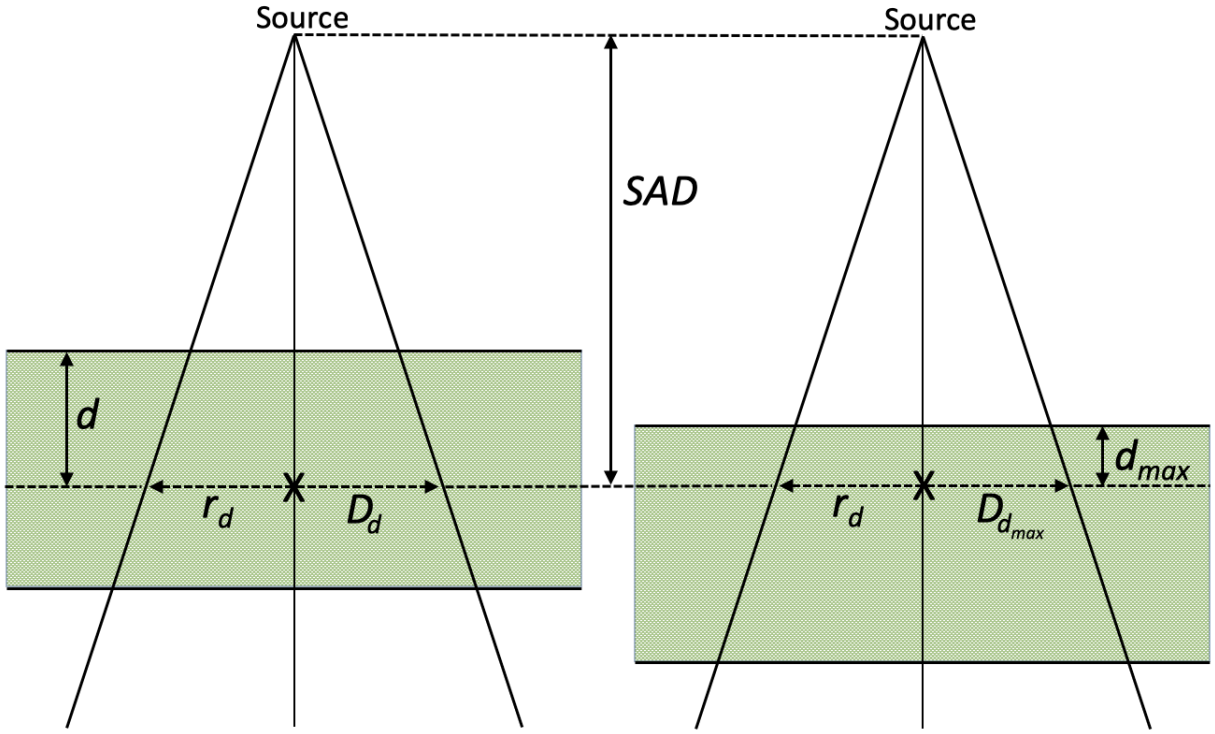

Figure 2.4: TMR variables using SAD setup. (Inspired by [30].)

Stopping power is a value which defines the amount of energy a charged particle loses per unit path length during ionization interactions within a given medium. This value

is proportional to the square of the particle's charge and inversely proportional to the square of its velocity [30]. Additionally, as ionization interactions predominately occur with orbital electrons, the stopping power is approximately proportional to electron density [33]. As the energy losses increase, the absorbed dose to the material proportionally increases. For protons, this creates the Bragg Peak, whereby the absorbed dose peaks at the end of the particle's path in the given material [30]. The relative stopping power (RSP) is a comparison of the stopping powers of a particle within two different mediums. For beamline materials, this is done by making measurements to determine two range values. The first set of measurements determines the depth to a point along the particle's path in a medium, usually determined by an isodose line in radiation therapy. The medium is typically water, because it is the reference material used in treatment planning systems. The second set of measurements determines the depth to the same isodose point in the reference medium, with a piece of material placed in front. The relationship is given by the equation

$$RSP = \frac{R_w - R_m}{t_m}, \tag{2.5}$$

where R_w is the depth in water, R_m is the depth in water behind the material slab, and t_m is the physical thickness of the material slab [33].

3D Printing Technologies

3D printing (or *additive manufacturing*) can be performed using various types of 3D printing technologies. Common commercially available technologies include selective laser sintering (SLS), selective laser melting (SLM), stereolithography (SLA), and fused deposition modelling (FDM) each with their own advantages and disadvantages [4]. SLS and SLM printers operate by having two adjacent containers filled with a powdered

material. A laser (or similarly focused heat source) sinters (melts) the top layer of the powder in a predetermined pattern. Next, the container holding the lasered powder is lowered as other container is raised. A leveling drum then transfers a layer of fresh powder from the raised container to the lowered container. This layer-by-layer process is repeated until the desired product has been created, when it can be removed from the surrounding excess powder. The principle advantage this printer offers is the ability to print materials that require in situ structural support by using the surrounding powdered material, as opposed to printing disposable supports ad-hoc. Also of note, the final product's surface may have a granular texture, due to powder adhering to the exterior of the printed object during sintering [34].

The first commercial 3D printer, based on Charles Hull's 1986 patent, was an SLA configuration. This printer type operates in a similar fashion to the SLS and SLM printers. Using a photosensitive liquid resin as print medium, the printed object is formed by curing the material layer-by-layer, using either scanning laser or digital light projector. The build platform is incrementally lowered to begin the subsequent layer. These printers require a relatively extensive setup, and while the material selection maybe a limiting factor, SLA printers offer high dimensional resolution and accuracy [4].

FDM, also known as fused filament fabrication (FFF), is the most popular type of 3D printer, due to low cost, simple fabrication process, and plethora of available printable materials [35]. Although the printing resolution and precision is lower than other modalities, the availability and simplicity of the technology has led to its popularity with hobbyists and academicians for rapid prototyping. To print a 3D object, a digital model is converted to 'gcode', outlining commands for printable slices to be created by the specific

printer. During printing, thermoplastic filament is pushed through a heated extrusion head. The filament melts as it is forced through the nozzle of the extruder's 'hot-end', and is deposited, layer-by-layer, on the print bed, matching the cross-sectional geometry generated by the sliced gcode file. The printer is a three-axis system in which the print bed moves in the y direction, and the extrusion head moves in the x and z directions (as a specific example of multiple potential implementations of movement configurations). Subsequent layers are deposited in the same way. As each layer is deposited, it fuses with the underlying layers [4, 35].

Common 3D Printing Materials

The two most common 3D printing materials are Polylactic Acid (PLA) and Acrylonitrile Butadiene Styrene (ABS). PLA is the most popular material and can be printed by nearly all FDM printers, as it does not require a heated bed, has a lower melting temperature, and is not as prone to warping. These qualities make PLA a common base material, as it is often blended with other materials to create new filaments with different characteristics. PLA is, however, relatively brittle, whereas ABS is more durable, resistant to impact, and is as low in cost. ABS can be prone to warping and can shrink as it cools during printing, causing dimensional inaccuracies [36]. Both materials are relatively tissue equivalent, based on HU values determined via CT scans [37], making them attractive for use in radiation therapy. Another common material that is more flexible is Thermoplastic Polyurethane (TPU). This material also has good impact resistance, but must be printed much more slowly [36].

Characterization of Materials

It is important to know the physical and radiological properties of the materials being used in radiation therapy [38, 39], and efforts to characterize common 3D printing materials have been made. Meyer et al. (2018) outlines a framework for commissioning 3D printed materials before clinical use [40], and various physical properties of 3D printed materials have been investigated by Pilipovic et al. (2009). These authors compared the dimensional accuracy, surface roughness, flexural properties, and tension properties between 3D printed materials printed on two different printers [41]. Using four different printing techniques, Michiels et al. (2016) characterized the printing accuracy, mechanical response, and effects of radiation on the mechanical response of eight materials, including ABS. They also investigated the photon linear attenuation coefficients and proton range shift of the materials [15]. Printing results were examined for both FDM and SLA printing techniques in regards to density and precision. The authors found the FDM printed material to have a reduced effective density of 13% post-print compared to the material density, even when printing at 100% infill, indicating the inclusion of air pockets within the printed object [38]. How 3D printed materials' density and HU values varied between print jobs and how the values changed over time was examined by Craft et al. (2018). Four materials were printed into multiple blocks. The variation in HU and density values were compared between the blocks of each material and over five weeks of storage of the materials in either an open box or with a desiccant. The group of investigators also compared PDD measurements to the treatment planning system (TPS) calculations in which the density of the material was input into the TPS versus using the

HU value acquired. They found the calculated results to be within 2 mm compared with the measured PPD values [42].

Investigation into infill percentage effects have been made by many authors [39, 43, 44]. Ricotti et al. (2016) and Ricotti et al. (2017) examined how the dose distributions changed using different infill percentages for high dose rate brachytherapy applicators and boluses, respectively. Both studies took a CT scan of each material, used the median HU unit value, and found the HU value increased with an increase in infill density [39, 43]. Ricotti et al. (2016) determined that brachytherapy applicators using ABS material could be 3D printed with a low infill percentage, saving time and material, and have a dose distribution comparative to commercial applicators with negligible differences [43]. Ricotti et al. (2017) determined that infill percentages of 20% and greater were dense enough for the treatment planning system (TPS) to treat the material as homogenous [39].

The HU values of various materials have also been investigated by multiple authors. Bibb et al. (2011) took 120 kVp CT scans of 100% infill 3D printed materials both in an air-equivalent polystyrene foam support and next to a tissue equivalent phantom. These values were compared to the material density and found to be approximately linearly related [1]. Dancewicz et al. (2017) investigated the HU values of various 3D printed materials using an 80 kVp beam, a 120 kVp beam, and a megavoltage (MV) beam, and found similar results when comparing relative infill density of each material [45]. Both authors related the HU values back to given values of equivalent human tissues [1, 45]. Solc et al. (2018) examined the variation between prints of the same material. Multiple materials were printed at 100% infill using different 3D printers and/or printing temperatures from three companies. The linear attenuation coefficient and HU values

were determined for each material at different energies. The results showed large deviations in the effective mass density of some of the printed materials compared with the mass density of the material due to poor printing quality. There was also a variation in HU value between prints of the same material depending on the 3D printer that was used [37]. Table 2.1 shows a summary of the work that has been done by the authors mentioned.

Table 2.1: Summary of previous work.

Property	Investigators
Density	Bibb (2010), Fujimoto (2017), Lindsay (2015), Zhou (2015)
Density infill variations	Dancewicz (2017), Ricotti (2016), Ricotti (2017)
Density variations over time	Craft (2018)
Variation between prints of same material	Craft (2018), Solc (2018)
Infill pattern variations	Madamesila (2016)
Mechanical properties	Michiels (2017), Pilipovic (2009), Ricotti (2017)
Dimensional accuracy	Fujimoto (2017), Kitamori (2019), Lindsay (2015), Michiels (2017), Pilipovic (2009), Ricotti (2016)
Relative electron density	Kitamori (2019), Zou (2015), Madamesila (2016), Michiels (2017)
Linear attenuation coefficient	Michiels (2017), Solc (2018)
HU values	Bibb (2011), Craft (2018), Dancewicz (2017), Fujimoto (2017), Kitamori (2019), Lindsay (2015), Madamesila (2016), Michiels (2017), Ricotti (2016), Ricotti (2017), Solc (2018), Zou (2015)
Photon PDDs	Craft (2018), Ricotti (2017), Fujimoto (2017)
Stopping power	Lindsay (2015), Zhou (2015), Michiels (2017)
Comparison with TPS	Craft (2018), Fujimoto (2017)
Comparison to equivalent tissues	Bibb (2011), Dancewicz (2017), Solc (2018)

The density of the 3D printed material is the most important characteristic in implementing 3D printed materials into the TPS for use in patient treatment in radiation oncology. Craft et al. (2018) illustrates that assuming materials are water equivalent in the TPS is a very poor assumption to make, resulting in large deviations from the measured PDD curve. Using HU-to-density calibration curves can also produce large

errors in the TPS dose calculation. These values, however, can potentially be used, depending on the material and accuracy needed. Inputting the physical density of the material is the most accurate of the three options when implementing the material into the TPS, according to the examination done by Craft et al. (2018) [42]. Measurement of the radiological response using the 3D printed material is important because of the variation which could occur due to printing inconsistencies, causing air gaps within the print, and geometry inaccuracies [39]. Knowing the density and radiological response of the materials being used for patient treatment should allow the material to be accurately modelled in the TPS.

CHAPTER III

MATERIALS AND METHODS

3D Printing the Materials

Two FDM 3D printers were used, the Maker's Tool Works *Fusematic* [46] and the Artillery3D (enovo) *Sidewinder X1* [47]. Both printers have a heated bed to help reduce warping of the printed filament, a 0.4 mm nozzle diameter, and require a 1.75 mm diameter filament. The *Fusematic* printer has a 200x225x200 mm^3 bed and a 0.1 mm layer resolution in the z direction (not specifying the resolution in the x and y directions). The Artillery Sidewinder has a 300x300x400 mm^3 bed and a 0.05 mm, 0.05 mm, and 0.1 mm position resolution in the x, y, and z direction, respectively.

An extensive search was conducted to determine the materials available that have potential for use or have been used in radiation therapy. The full list of materials and hyperlinks for where to buy them is given in Appendix A. The list was narrowed to the materials printed for this study, shown in Table 3.1.

Table 3.1: Printing parameters and purchasing information for each material printed.

Material	Abbrev.	Printer	Nozzle Temp Used (°C)	Bed Temp Used (°C)	Print Speed (mm/s)	Price ($)/kg	Bed Adhesion Used	Manufacturer
Acrylonitrile Butadiene Styrene	ABS	Artillery	245	110	50	18.99	Hairspray	Hatchbox
Algae based PLA	Algae PLA	Artillery	205	45	100	34.99	None	3DPrintLife
Composite Iron PLA	Iron PLA	Artillery	245	70	100	80	None	Proto-Pasta
Polylactic Acid	PLA	Fusematic	225	70	100	18.99	None	Hatchbox
Armadillo Thermoplastic Polyurethane	TPU	Artillery	220	45	30	62	Hairspray	NinjaTek
Wood particles in PLA	Wood PLA	Artillery	240	70	100	34.99	None	Hatchbox

The printed materials were determined based on ease of print, potential relevancy, cost, and differences in initial HU values. The materials used were 1.75 mm +/- 0.03 mm in diameter. For each material, four 20x10x1 cm^3 blocks were printed using 100% infill and a rectilinear pattern. The speed, bed temperature, nozzle temperature, etc. were dependent upon the material. A stereolithography (STL) file of the block was imported into Slic3r [48], a 3D slicing engine, to create the gcode file used for printing the blocks. The print parameters for each material are given in Table 3.1. The electron measurements were made with the blocks of the printed dimensions. The blocks were then cut in half using a band saw, resulting in eight blocks with dimensions approximately 10x10x1 cm^3. The remaining measurements were made with these blocks.

CT

HU Measurements

CT scans of pre-printed material spools were performed using 120 kVp, 600 mA, a pitch of 1.375 and a slice thickness of 2.5 mm on a Discovery CT590 RT. HU values of

the materials were assessed by assigning the maximum HU value as an accurate representation of each material. A subset of the materials to be printed were then determined, in part by choosing materials with dissimilar HU values.

Eight blocks of each post-printed material were scanned individually. The blocks were taped together and placed edgewise on the scanner table with the front face of the blocks parallel with the axial slice direction. CT markers were placed on each block to enable differentiation of the blocks in the scan. The setup allowed for multiple slices to be imaged within one block. The parameters used were 120 kV, 600 mA, a pitch of 0.938, and a slice thickness of 2.5 mm. A 40x40 mm^2 region of interest (ROI) was centered on the axial slices of the CT scan, shown in Figure 3.1.

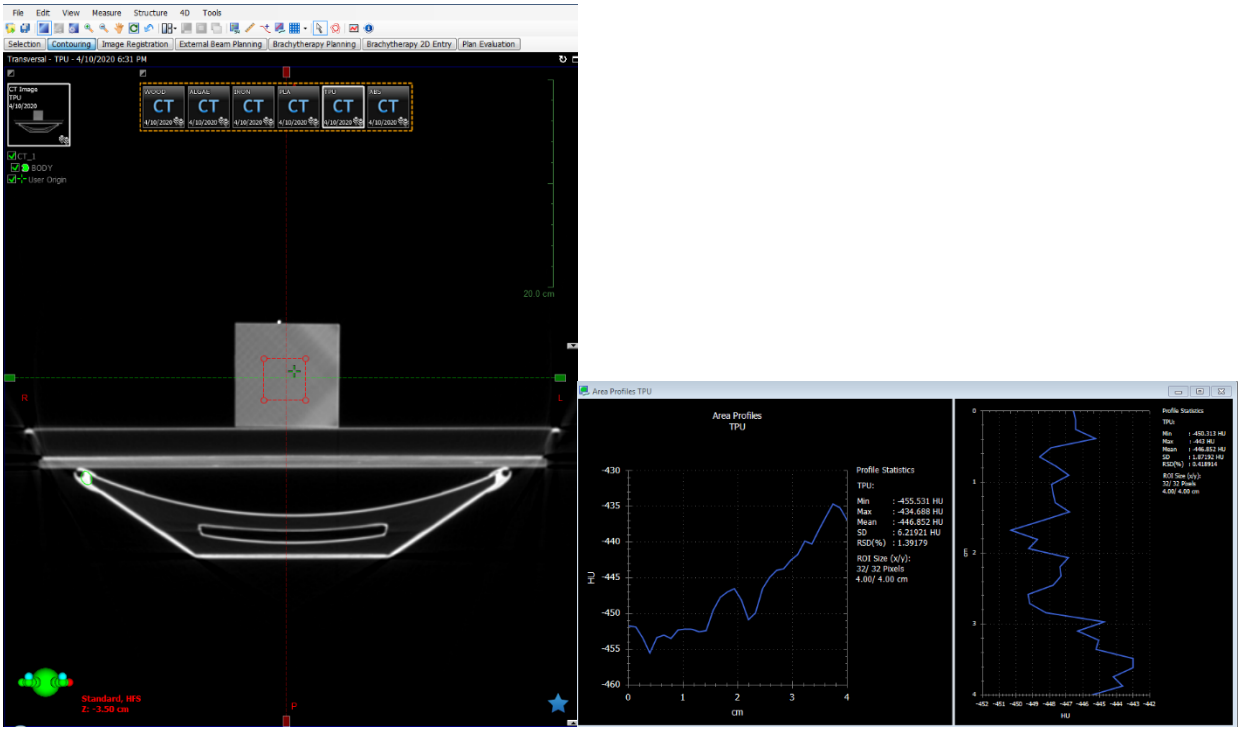

Figure 3.1: The extraction of data using the CT scan.

The mean HU and standard deviation values were recorded for two slices for each block of material, giving sixteen HU and standard deviation values for each material.

HU Calculations

The sixteen HU values for each material were averaged to obtain a representative HU value for each block using

$$\bar{x} = \frac{1}{N}\sum_{i=1}^{N} x_i, \tag{3.1}$$

where $\bar{x}$ is the average, N is the number of measurements, and x is each individual measurement [49]. This gives

$$\overline{HU}_{material} = \frac{1}{16}\sum_{i=1}^{16} (HU_{material})_i, \tag{3.2}$$

where $\overline{HU}_{material}$ is the average HU value for the given material and $HU_{material}$ is each individual HU value for the given material. An example is shown in Appendix B.

HU Uncertainty Calculations

The uncertainty of the average value was determined using

$$\sigma = \sqrt{\frac{1}{N}\sum_{i=1}^{N} (x_i - \bar{x})^2}, \tag{3.3}$$

where σ is the standard deviation [49]. This equation gives

$$\sigma_{\overline{HU}_{material}} = \sqrt{\frac{1}{16}\sum_{i=1}^{16N} ((HU_{material})_i - \overline{HU}_{material})^2}, \tag{3.4}$$

where $\sigma_{\overline{HU}_{material}}$ is the uncertainty of the average HU value of the given material. An example is shown in Appendix B.

Electron

Electron Measurements

The electron measurements were made using 2x20 cm^2 strips of Ashland's EBT-3 Gafchromic™ film on a Varian Trilogy linear accelerator using electron beams. The film has an optimal dynamic range of 0.2 to 10 Gy and a spatial resolution of approximately 25 μm [50]. The evaluation of each material under electron beams was performed as follows. The printed blocks were stacked on a polystyrene foam block of approximate air equivalence (-985 HU). The gantry was set to 270°, the collimator to 0°, and a 10x10 cm^2 electron-cone was used to define the field geometry. Using a 'front-pointer', a physical rod defining a set distance from the radiation source during installation, the SSD was set to 100 cm and centered upon of the block stack. The treatment table was indexed longitudinally to ensure the blocks were orthogonal to the beam along the face of the blocks. The position of the first set of blocks was outlined on the foam to ensure reproducibility of the setup. A film strip was then place within the center of the printed block stack, and aligned flush to the edge closest to the beam using the front-pointer. The final setup is depicted in Figure 3.2.

At the treatment console, a 6 MeV electron beam was delivered in 'service' mode of 300 MU at a 1000 MU/min dose rate. The film was then replaced with a new piece of film and placed in a light-tight box. This process was repeated for energies of 9, 12, 16, and 20 MeV.

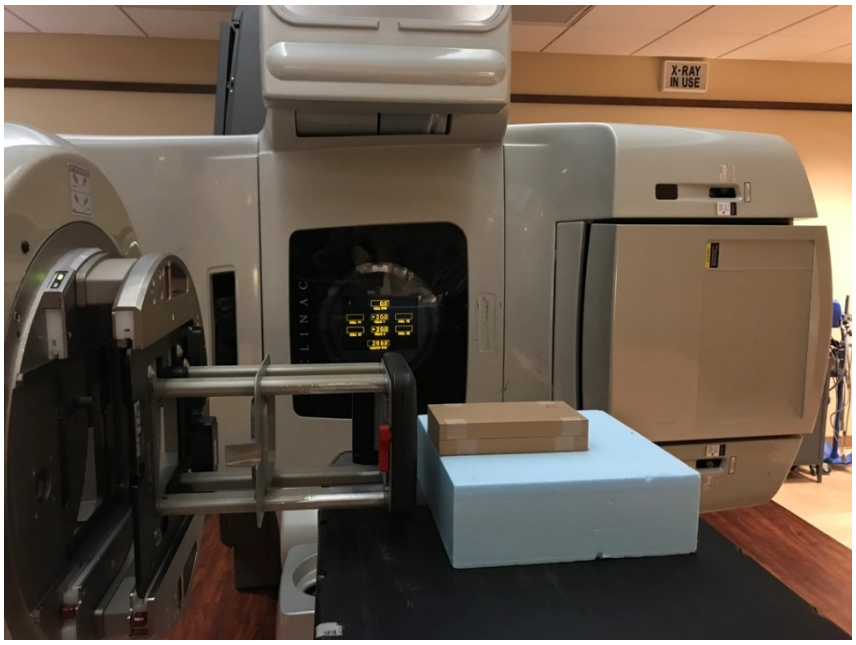

Figure 3.2: Example of the electron measurement setup using the Wood PLA blocks, using settings: gantry 270°, collimator 0°, SSD 100 cm, 10x10 cm^2 field size.

24 (± 12) hours after irradiation, the film was digitized via *EPSON 10000XL* flatbed scanner 'EPSON Scan' software [51]. The parameters used are shown in Figure 3.3.

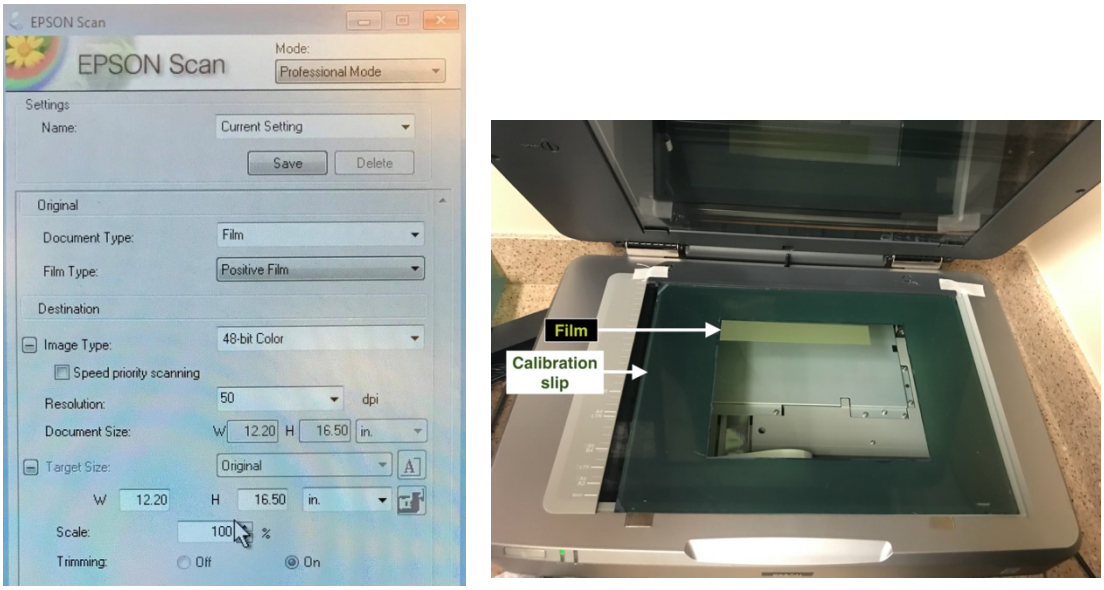

Figure 3.3: Left: Scanning parameters used on EPSON scan. Right: Orientation of film on film scanner.

The scanner was turned on and allowed to warmup up for at least 15 minutes, and the scanner glass was cleaned to eliminate noise occurring from dust particles. To scan

each film, the film was placed in the top left corner of the glass bordered by a calibration slip. A piece of glass was placed on top to ensure the film was flat, reducing newton's rings artifacts. This is shown in Figure 3.3. A preview of the scan was created by the software, and the scanning area was selected by outlining the perimeter of the glass area. The section of scanner upon which each film was placed was reproduced to reduce scanner-based inter-scan discrepancies. Each film was then scanned five consecutive times, saving each scan as a lossless, 48-bit color TIFF file. An un-irradiated background film was also scanned in the same way [52].

The *ImageJ* [53] software was used in film analysis and data output to Excel. Using the 'straight line' tool, a line was selected through the center of the film strip along the beam path, parallel with the film edge. A 'plot profile' function was performed, and the data exported into Excel for each color channel (red, green, blue) (Figure 3.4A). To ensure that the coordinates for each color channel and plot profile were constant for the three separate data acquisitions, the following process was used. The original line centered along the length of the film was indexed five pixel values in the +y direction of the image, and the plot profile data for each of the color channels exported (Figure 3.4B). The same line was then indexed five pixel values in the -y direction below center and the plot profile data subsequently exported for each color channel (Figure 3.4C). This process was repeated for each film strip scan. For each energy, each film strip was scanned five times, and three lines of data were taken for each color channel, resulting in fifteen pixel values for each color channel dose value, and forty-five pixel values for the final dose value for the given depth.

Figure 3.4: Orientation of plot profile line on film for (A) center of film (B) 5 pixels in +y direction from center of film and (C) 5 pixels in -y direction from center of film.

Film Calculations

Calibration films were used to convert the pixel values of the film data into dose values. Each film in the calibration set was obtained by irradiating a piece of film with a known dose. The film was scanned in the same orientation on the scanner as described above. The mean, minimum, and maximum pixel values, as well as the standard deviation for each color channel were obtained for each known dose value. Each mean pixel value for the given calibration dose value was normalized by subtracting 2^{16} (due to 16 bits per channel) from the pixel value by

$$P_{norm,D_{cal}} = 2^{16} - \bar{P}_{D_{cal}}, \tag{3.5}$$

where $P_{norm,D_{cal}}$ is the normalized pixel value for the given known calibration film dose, D_{cal}, and $\bar{P}_{D_{cal}}$ is the average pixel value for the given known calibration film dose. The background was subtracted from each pixel value for each color channel using

$$P_{final,D_{cal}} = P_{norm,D_{cal}} - bkg_{color}, \tag{3.6}$$

where $P_{final,D_{cal}}$ is the final pixel value for the given known calibration dose and bkg_{color} is the background value for the given color channel. The background used was obtained

from the un-irradiated background film. These values were plotted to obtain the calibration curve for each color channel. An equation was fit to the calibration curves using the 'Solver' function in Excel to implement the least-squares fitting method. The fit equation was then inverted, so that dose was then the dependent variable, in the form of

$$D = \left(-\frac{a - (b\,x\,P)}{c - (d\,x\,P)}\right)^{e}, \tag{3.7}$$

where *a*, *b*, *c*, *d*, and *e* are fit parameters (Table 3.2), and P is the pixel value. To solve for the calibration fit equation dose values, $D = D_{cal}$ and $P = P_{final,D_{cal}}$. This equation was used as the final equation to solve for dose using the 3D printed material irradiated film. The calibration curves are shown in Figure 3.5.

Table 3.2: Parameters used in the dose fit equation for each color channel.

	Color Channel		
Parameter	**Red**	**Green**	**Blue**
a	58615310275522600	7288569320959520000	3516046701491590000
b	322204126629000	11627043719979700	7078675333885350
c	56258887832507700	660161046024394000	186955495994128000
d	1435381496850	17262388783450	7027572534450
e	1.07155832225439	0.979836116546895	1.06148995117795

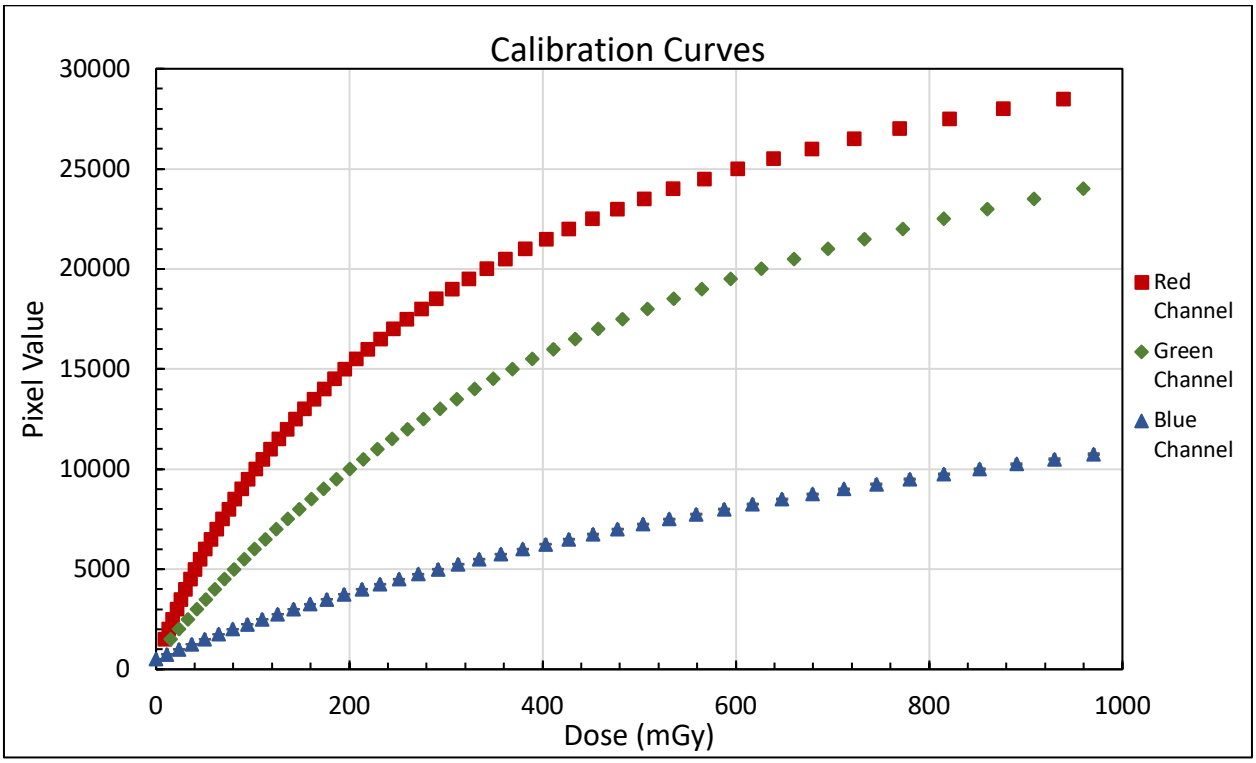

Figure 3.5: Calibration curves for the red, green, and blue channels.

All raw pixel values from the film data sets were normalized individually using

$$P_{norm,d} = 2^{16} - P_{raw,d}, \tag{3.8}$$

where $P_{norm,d}$ is the normalized pixel value for the given depth, d, and $P_{raw,d}$ is the raw pixel value for the given depth. The normalized pixel values were then averaged across the row using Equation 3.1 to get

$$\bar{P}_d = \frac{1}{15}\sum_{i=1}^{15}(P_{norm,d})_i, \tag{3.9}$$

where $\bar{P}_d$ is the average pixel value for the given depth. The background was subtracted to obtain the final pixel value via

$$P_{final,d} = \bar{P}_d - bkg, \tag{3.10}$$

where $P_{final,d}$ is the final pixel value for the given depth and bkg is the background value. The background used was obtained by using the minimum $P_{norm,d}$ value from the

respective film data. The final pixel value was input into Equation 3.7 for the respective color channel, where $P = P_{final,d}$, to obtain a dose value for the respective color channel and depth ($D = D_{color,d}$). To obtain the final dose value from the three color channel dose values, the triple channel least-squares method described by Micke et al. (2011) was considered, in which the dose difference between the color channels is minimized [54]. Assuming uniform thickness of the film active layer, the least-squares method can be reduced by finding the minimum distance between the three color channels through the following method:

Given

$$f(D) = (R - D)^2 + (G - D)^2 + (B - D)^2,$$

where *R*, *G*, and *B*, are the red, green, and blue dose values, respectively, and *D* is the desired final dose value, the minimization of *f(D)* would give the dose value which minimizes the path between the color channel dose values. This is done by setting the derivative of *f(D)* equal to zero and solving for *D*.

Solving

$$min((R - D)^2, (G - D)^2, (B - D)^2) \; for \; variable \; D = D_{min}$$

by

$$\frac{\partial f(D)}{\partial D} = 0,$$

and substituting $f(D)$, where $D = D_{min}$, this becomes

$$\frac{\partial[(R - D_{min})^2 + (G - D_{min})^2 + (B - D_{min})^2]}{\partial D_{min}} = 0$$

$$2(R - D_{min}) + 2(G - D_{min}) + 2(B - D_{min}) = 0$$

$$2R + 2G + 2B - 6D_{min} = 0.$$

$$min((R-D)^2,(G-D)^2,(B-D)^2)\ for\ variable\ D = D_{min}$$

Solving for D_{min},

$$D_{min} = \frac{1}{3}(R+G+B),$$

which is equal to taking the average of the three color channel dose values to find the final dose, *D*.

Using this reasoning, the dose values from each of the color channels were averaged to obtain the final dose value for each depth using Equation 3.1 to get

$$\overline{D}_d = \frac{D_{red,d} + D_{green,d} + D_{blue,d}}{3}, \tag{3.11}$$

where $\overline{D}_d$ is the average dose value for the given depth, and $D_{red,d}$, $D_{green,d}$, $D_{blue,d}$, are the dose values for the respective color channel for the given depth. The PDD for each depth was determined using

$$PDD_d = \frac{\overline{D}_d}{\overline{D}_{d_{max}}}\ x\ 100, \tag{3.12}$$

where PDD_d is the percent depth dose value for the given depth and $\overline{D}_{d_{max}}$ is the dose at the depth of maximum dose (d_{max}).

The R_{50} of each PDD curve was also calculated. R_{50} is the "depth…at which the percent depth dose is 50%" of the maximum dose [30]. Using the 'Forecast' function in Excel, the depth at which the dose is 50% of the maximum dose was determined. An example of each calculation is shown in Appendix B.

Film Uncertainty Calculations

The uncertainties of the calibration film raw pixel values were given in the calibration data, and were the same after the pixel was normalized. The uncertainty of the final pixel value was determined by the subtraction uncertainty equation, for $u = x - y$,

$$\sigma_u = \sqrt{(\sigma_x)^2 + (\sigma_y)^2}, \tag{3.13}$$

where σ_u, σ_x, and σ_y are the uncertainty values of the associated variables [49]. This gives

$$\sigma_{P_{final,D_{cal}}} = \sqrt{\left(\sigma_{P_{norm,D_{cal}}}\right)^2 + \left(\sigma_{bkg_{color}}\right)^2} \tag{3.14}$$

when applied to Equation 3.6, where $\sigma_{P_{final,D_{cal}}}$ is the uncertainty of the final pixel value for the given known calibration dose, $\sigma_{P_{norm,D_{cal}}}$ is the uncertainty of the normalized pixel value for the given known calibration dose, and $\sigma_{bkg_{color}}$ is the uncertainty in the background value for the given color channel.

The uncertainty of the each average pixel value from the film data was determined using by the standard deviation of the pixel values, using Equation 3.3 to get

$$\sigma_{\bar{P}_d} = \sqrt{\frac{1}{15}\sum_{i=1}^{15}((P_{norm})_i - \bar{P}_d)^2}, \tag{3.15}$$

where $\sigma_{\bar{P}_d}$ is the uncertainty of the average pixel value for the given depth. The uncertainty of each final pixel value of the film data was found by applying Equation 3.13 to Equation 3.10 to get

$$\sigma_{P_{final,d}} = \sqrt{\left(\sigma_{\bar{P}_d}\right)^2 + \left(\sigma_{bkg}\right)^2}, \tag{3.16}$$

where $\sigma_{P_{final,d}}$ is the uncertainty of the final pixel value for the given depth, $\sigma_{\bar{P}_d}$ is the uncertainty of the average pixel value for the given depth, and σ_{bkg} is the uncertainty of the background value.

The uncerainty of the fit equation was dependent on the uncertainty of the fit parameters and the pixel value. To determine the uncertainty of the fit parameters, four scenarios were considered using the extreme cases of dose and pixel values: high dose and high pixel value; low dose and low pixel value; high dose and low pixel value; and low dose and high pixel value. These values were determined by dose $\pm\sigma_D$ and pixel value $\pm\sigma_P$. Using these scenarios, the calibration fit equation was recalculated to investigate how the fit parameters changed. The investigation revealed a change in only parameter *e*. The uncertainty in the parameter was then determined by

$$\sigma_e = \frac{e_{max} - e_{min}}{2}.$$

where σ_e is the uncertainty of parameter e, and e_{max} and e_{min} are the maximum and miminum values of parameter e, respectively. Hence, the uncertainty of the dose calculated from the fit equation was only dependent on the uncertainty of the final pixel value and parameter *e*. The general uncertainty propagation formula is given as

$$\sigma_u = \sqrt{\left(\frac{\partial u}{\partial x}\right)^2 \sigma_x^2 + \left(\frac{\partial u}{\partial y}\right)^2 \sigma_y^2 + \left(\frac{\partial u}{\partial z}\right)^2 \sigma_z^2 + \cdots}, \tag{3.17}$$

where $\partial u/\partial x$, $\partial u/\partial y$, and $\partial u/\partial z$ are derivatives of u with respect to the independent variables x, y, and z, respectively; and σ_x, σ_y, and σ_z, are the uncertainties of the respective independent variables [49]. Applying Equation 3.17 to Equation 3.7, the uncertainty equation for the calibration dose is

$$\sigma_{D_{cal}} = \sqrt{\left(\frac{\partial D_{cal}}{\partial P_{final,D_{cal}}}\right)^2 \sigma_{P_{final,D_{cal}}}^2 + \left(\frac{\partial D_{cal}}{\partial e}\right)^2 \sigma_e^2}, \tag{3.18}$$

where

$$\frac{\partial D_{cal}}{\partial P_{final,D_{cal}}} =$$

$$e\left[\frac{d\left(\left(b\ x\ P_{final,D_{cal}}\right)-a\right)}{\left(c\ -\left(d\ x\ P_{final,D_{cal}}\right)\right)^2}+\frac{b}{\left(c\ -\left(d\ x\ P_{final,D_{cal}}\right)\right)}\right]\left[\frac{\left(\left(b\ x\ P_{final,D_{cal}}\right)-a\right)}{\left(c\ -\left(d\ x\ P_{final,D_{cal}}\right)\right)}\right]^{e-1}$$

and

$$\frac{\partial D_{cal}}{\partial e}=\left[\frac{\left(b\ x\ P_{final,D_{cal}}\right)-a}{\left(c\ -\left(d\ x\ P_{final,D_{cal}}\right)\right)}\right]^{e}\log\left[\frac{\left(b\ x\ P_{final,D_{cal}}\right)-a}{\left(c\ -\left(d\ x\ P_{final,D_{cal}}\right)\right)}\right].$$

Inputting the derivatives, the fit equation becomes

$\sigma_{D_{cal}} =$

$$\sqrt{\left(e\left[\frac{d\left(\left(b\ x\ P_{final,D_{cal}}\right)-a\right)}{\left(c\ -\left(d\ x\ P_{final,D_{cal}}\right)\right)^2}+\frac{b}{\left(c\ -\left(d\ x\ P_{final,D_{cal}}\right)\right)}\right]\left[\frac{\left(\left(b\ x\ P_{final,D_{cal}}\right)-a\right)}{\left(c\ -\left(d\ x\ P_{final,D_{cal}}\right)\right)}\right]^{e-1}\right)^2\sigma^2_{P_{final,D_{cal}}}+\cdots}$$

$$\overline{\cdots+\left(\left[\frac{\left(b\ x\ P_{final,D_{cal}}\right)-a}{\left(c\ -\left(d\ x\ P_{final,D_{cal}}\right)\right)}\right]^{e}\log\left[\frac{\left(b\ x\ P_{final,D_{cal}}\right)-a}{\left(c\ -\left(d\ x\ P_{final,D_{cal}}\right)\right)}\right]\right)^2\sigma_e^2},\qquad(3.19)$$

where $\sigma_{D_{cal}}$ is the uncertainty of the known calibration dose. The maximum pixel uncertainty found for each color channel was used as $\sigma_{P_{final,D_{cal}}}$. This equation was also used to find the uncertainty of the film data dose values in which $\sigma_{D_{cal}}$= σ_{D_d} and $\sigma_{P_{final,D_{cal}}}$= $\sigma_{P_{final,d}}$.

The dose uncertainty for each color channel was propagated through the averaging calculation using

$$\sigma_{\bar{D}_d}=\sqrt{\left(\frac{\partial\bar{D}_d}{\partial D_{red,d}}\right)^2\sigma^2_{D_{red,d}}+\left(\frac{\partial\bar{D}_d}{\partial D_{green,d}}\right)^2\sigma^2_{D_{green,d}}+\left(\frac{\partial\bar{D}_d}{\partial D_{blue,d}}\right)^2\sigma^2_{D_{blue,d}}},\qquad(3.20)$$

where $D_{red,d}$, $D_{green,d}$, and $D_{blue,d}$ are the doses for the given color channel and depth; and $\sigma_{D_{red,d}}$, $\sigma_{D_{red,d}}$, and $\sigma_{D_{red,d}}$ are the uncertainties of the doses for the given color channel and depth. The derivatives of $\bar{D}_d$ with respect to the dose values are 1/3, simplifying the equation to

$$\sigma_{\bar{D}_d} = \sqrt{\left(\frac{1}{3}\right)^2 \sigma_{D_{red,d}}^2 + \left(\frac{1}{3}\right)^2 \sigma_{D_{green,d}}^2 + \left(\frac{1}{3}\right)^2 \sigma_{D_{blue,d}}^2}. \tag{3.21}$$

The uncertainty of the PDD calculation for each depth was found using the uncertainty equation for division, where $u = x/y$,

$$\sigma_u = u\sqrt{\left(\frac{\sigma_x}{x}\right)^2 + \left(\frac{\sigma_y}{y}\right)^2}. \tag{3.22}$$

Applying Equation 3.22 to Equation 3.12, this becomes

$$\sigma_{PDD_d} = PDD_d\sqrt{\left(\frac{\sigma_{\bar{D}_d}}{\bar{D}_d}\right)^2 + \left(\frac{\sigma_{\bar{D}_{d_{max}}}}{\bar{D}_{d_{max}}}\right)^2}, \tag{3.23}$$

where σ_{PDD_d} is the uncertainty of the PDD for the given depth and $\sigma_{\bar{D}_{d_{max}}}$ is uncertainty of the dose at the depth of maximum dose.

The uncertainty of the R_{50} calculation was found in the following way. Given two known data points (x_1, y_1) and (x_2, y_2), then the linearly interpolated y value, y_{int}, given the desired x value, x_{int}, is calculated by

$$y_{int} = y_1 + (x_{int} - x_1)\left(\frac{y_2 - y_1}{x_2 - x_1}\right). \tag{3.24}$$

Using Equation 3.23, the equation to solve for R_{50} becomes

$$R_{50} = d_{low} + (PDD_{50\%} - PDD_{low})\left(\frac{d_{high} - d_{low}}{PDD_{high} - PDD_{low}}\right), \tag{3.25}$$

where d_{low} and d_{high} are the known depth values below and above R_{50}, respectively; $PDD_{50\%}$ is the 50% PDD value; and PDD_{low} and PDD_{high} are the known PDD values below and above $PDD_{50\%}$, respectively. Using Equation 3.17, the uncertainty was propagated through Equation 3.24 to get

$$\sigma_{R_{50}} = \sqrt{\left(\frac{\partial R_{50}}{\partial d_{low}}\right)^2 \sigma_{d_{low}}^2 + \left(\frac{\partial R_{50}}{\partial d_{high}}\right)^2 \sigma_{d_{high}}^2 + \left(\frac{\partial R_{50}}{\partial PDD_{low}}\right)^2 \sigma_{PDD_{low}}^2 + \cdots} \\ \overline{\cdots + \left(\frac{\partial R_{50}}{\partial PDD_{high}}\right)^2 \sigma_{PDD_{high}}^2}. \quad (3.26)$$

For

$$\frac{\partial R_{50}}{\partial d_{low}} = \frac{PDD_{low} - PDD_{50\%}}{PDD_{low} - d_{high}},$$

$$\frac{\partial R_{50}}{\partial d_{high}} = \frac{(PDD_{low} - PDD_{50\%})(d_{low} - PDD_{high})}{PDD_{low} - d_{high}},$$

$$\frac{\partial R_{50}}{\partial PDD_{low}} = \frac{(d_{high} - PDD_{50\%})(d_{low} - PDD_{high})}{(PDD_{low} - d_{high})^2},$$

and

$$\frac{\partial R_{50}}{\partial PDD_{high}} = \frac{d_{high} - PDD_{50\%}}{d_{high} - PDD_{low}},$$

this becomes

$$\sigma_{R_{50}} = \\ \sqrt{\left(\frac{PDD_{low} - PDD_{50\%}}{PDD_{low} - d_{high}}\right)^2 \sigma_{d_{low}}^2 + \left(\frac{(PDD_{low} - PDD_{50\%})(d_{low} - PDD_{high})}{PDD_{low} - d_{high}}\right)^2 \sigma_{d_{high}}^2 + \cdots} \quad (3.27) \\ \overline{\cdots + \left(\frac{(d_{high} - PDD_{50\%})(d_{low} - PDD_{high})}{(PDD_{low} - d_{high})^2}\right)^2 \sigma_{PDD_{low}}^2 + \left(\frac{d_{high} - PDD_{50\%}}{d_{high} - PDD_{low}}\right)^2 \sigma_{PDD_{high}}^2},$$

where $\sigma_{d_{low}}$ and $\sigma_{d_{high}}$ are the uncertainties of the known depth values below and above the interpolated depth value, respectively; and $\sigma_{PDD_{low}}$ and $\sigma_{PDD_{high}}$ are the uncertainties of the known PDD values below and above the interpolated depth value, respectively. An example of each uncertainty calculation is shown in Appendix B.

Photon

Photon Measurements

The photon measurements were made using a PTW-Freiburg TN34045 (SN 001558) parallel plate ion chamber. The chamber was placed within the top block of 5 cm of plastic water blocks, and a 1 cm plastic water block with a cutout for the chamber to fit within was placed on top such that the top surface of the detector was flush with the top of the plastic water block. The blocks underneath the chamber were utilized for the purpose of backscatter. The gantry and collimator were set to 0°, and the treatment table was raised until the surface of the detector was set to 100 cm SAD by optical distance indicator (ODI). The detector was centered at isocenter under the treatment head plastic water by external lasers. The *Standard Imaging* Max-4000 (SN F110456) electrometer [55] was set to -300 V bias in 'low range' mode. The first block placed on the detector was centered using the light field. The setup is shown in Figure 3.6.

Using 'service mode', 100 MU of 6MV photon radiation was delivered at 600 MU/min, using a 10x10 cm^2 field size, and at 100 cm SAD. This was repeated using an 18 MV beam. The measurements for each energy were repeated, adding a 1 cm thick block of each of the 3D printed materials to the top of the stack for added depth to the detector, for a total of eight measurements for each energy (totaling 8 cm depth). Three measurements were taken for each material at each depth except for the plastic water

'control' blocks, where only one measurement was made. This procedure was repeated for each material.

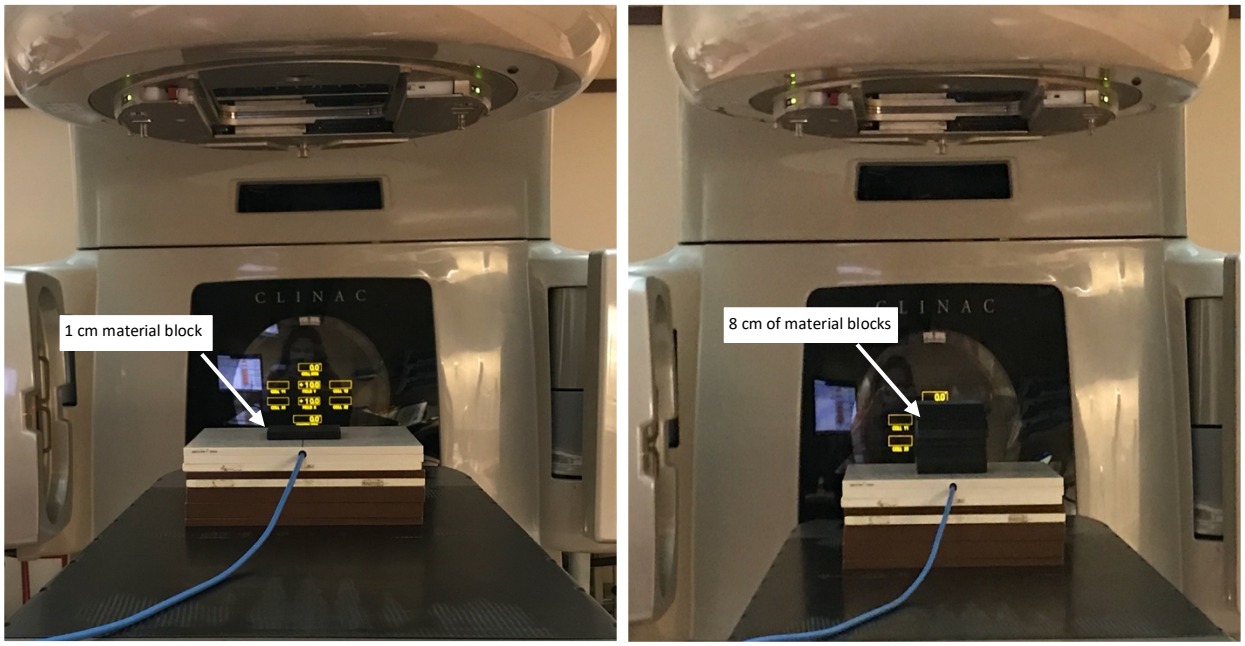

Figure 3.6: Setup for photon measurements.

Photon Calculations

The raw charge values were averaged to get a final raw charge value for each depth using Equation 3.1 to get

$$\bar{M}_{material,d} = \frac{1}{3}\sum_{i=1}^{3}(M_{material,d})_i, \tag{3.28}$$

where $\bar{M}_{material,d}$ is the average charge value for the given material and depth, and $M_{material,d}$ is each raw charge measurement for the given material and depth. The TMR was then calculated for each depth using

$$TMR_d = \frac{\bar{M}_{material,d}}{\bar{M}_{PW,d_{max}}}, \tag{3.29}$$

where TMR_d is the Tissue-Maximum ratio for the given depth and $\bar{M}_{PW,d_{max}}$ is the charge measurement at the depth of maximum charge in the plastic water blocks. Since the TMR values are relative values, and the charge measured is related to the absorbed dose, the charge values can be used in place of dose values to determine the TMR. The percent difference between the material measurements and the plastic water measurements was determined by

$$\%\, Difference = \frac{\bar{M}_{PW,d} - \bar{M}_{material,d}}{\bar{M}_{PW,d}}, \tag{3.30}$$

where $\%\, Difference$ is the percent difference between the average plastic water (PW) value for the given depth, $\bar{M}_{PW,d}$, and the average value for the given material for the given depth, $\bar{M}_{material,d}$. An example of these calculations is given in Appendix B.

Photon Uncertainty Calculations

The uncertainty of each photon measurement was determined by the ion chamber uncertainty of 1.3%. This value was given by the ADCL from which the chamber was calibrated. The uncertainty of each measurement was determined by

$$\sigma_{M_{n,d}} = 0.013\ x\ M_{n,d}, \tag{3.31}$$

where $\sigma_{M_{n,d}}$ is the uncertainty of the raw charge measurement and $M_{n,d}$ is the given measurement for the given depth. For each set of measurements, the uncertainty of the calculated average for each depth was determined by applying Equation 3.17 to Equation 3.28 to get

$$\sigma_{\bar{M}_{material,d}} = \sqrt{\left(\frac{\partial \bar{M}_{material,d}}{\partial M_{1,d}}\right)^2 \sigma^2_{M_{1,d}} + \left(\frac{\partial \bar{M}_{material,d}}{\partial M_{2,d}}\right)^2 \sigma^2_{M_{2,d}} + \left(\frac{\partial \bar{M}_{material,d}}{\partial M_{3,d}}\right)^2 \sigma^2_{M_{3,d}}}, \tag{3.32}$$

where $\sigma_{\bar{M}_{material,d}}$ is the uncertainty of the average charge for the given material and depth and $\sigma_{M_{n,d}}$ are the uncertainties of each raw charge measurement. Given $\partial \bar{M}_{material,d} / \partial M_{n,d}$ is 1/3, the equation simplifies to

$$\sigma_{\bar{M}_{material,d}} = \sqrt{\left(\frac{1}{3}\right)^2 \sigma_{M_{1,d}}^2 + \left(\frac{1}{3}\right)^2 \sigma_{M_{2,d}}^2 + \left(\frac{1}{3}\right)^2 \sigma_{M_{3,d}}^2}. \quad (3.33)$$

The uncertainty propagation for the TMR calculations was determined by Equation 3.22 as applied to Equation 3.29 to get

$$\sigma_{TMR_d} = TMR_d \sqrt{\left(\frac{\sigma_{\bar{M}_{material,d}}}{\bar{M}_{material,d}}\right)^2 + \left(\frac{\sigma_{\bar{M}_{PW,d_{max}}}}{\bar{M}_{PW,d_{max}}}\right)^2}, \quad (3.34)$$

where σ_{TMR_d} is the uncertainty of the TMR for the given depth, $\sigma_{\bar{M}_{material,d}}$ is the uncertainty of the average charge value for the given material and depth, and $\sigma_{\bar{M}_{PW,d_{max}}}$ is the uncertainty of the average charge value for plastic water at the depth of maximum charge. To determine the uncertainty of the percent difference calculations, the uncertainty of the difference was first calculated by starting with Equation 3.13, where $u = Diff = M_{d,PW} - \bar{M}_{material,d}$. The resulting equation becomes

$$\sigma_{Diff} = \sqrt{\left(\sigma_{\bar{M}_{PW,d}}\right)^2 + \left(\sigma_{\bar{M}_{material,d}}\right)^2}, \quad (3.35)$$

where σ_{Diff} is the uncertainty of the difference, and $\sigma_{\bar{M}_{PW,d}}$ is the uncertainty of the average charge measurement in the PW blocks for the given depth. To propagate the uncertainty through the percent difference calculation, Equation 3.22 was used, where $u = \%\, Difference = \frac{Diff}{M_{d,PW}}$. This gives

$$\sigma_{\%\,Diff} = \%\,Diff\sqrt{\left(\frac{\sigma_{Diff}}{Diff}\right)^2 + \left(\frac{\sigma_{\bar{M}_{PW,d}}}{\bar{M}_{PW,d}}\right)^2}, \tag{3.36}$$

where $\sigma_{\%\,Diff}$ is the uncertainty of the percent difference. An example of these calculations is given in Appendix B.

Proton

Proton Measurements

The proton measurements were made using an *IBA* PPC05 ion chamber, a *Standard Imaging* Max 4000 electrometer [55], and a *PTW* MP1 water tank on a 230 MeV *Mevion S250i™ with Hyperscan™* proton system [56]. The ion chamber's front window has a water equivalent thickness of 1.55 mm [57] and the water tank can move the ion chamber with a resolution of 1 mm [58]. The water tank was set up on the treatment couch so that the surface of the water was centered at the isocenter using external lasers. The air gap between the surface of the water and the bottom of the snout was 10 cm, and the gantry angle was set to 0°. The ion chamber was placed at the surface of the water tank. The setup is shown in Figure 3.7. The beams were constructed with 2.5 mm spot spacing, 1 MU/spot, and an 8x8 cm^2 field, giving 33x33 spots and totaling 1089 MU for each set of measurements. Measurements were taken for three energies: 70.77 Mev, the energy most frequently used in the clinic; 180.15 MeV, the largest energy possible based on the maximum depth of the small water tank; and 120.21 MeV, approximately midway between the larger and smaller energies.

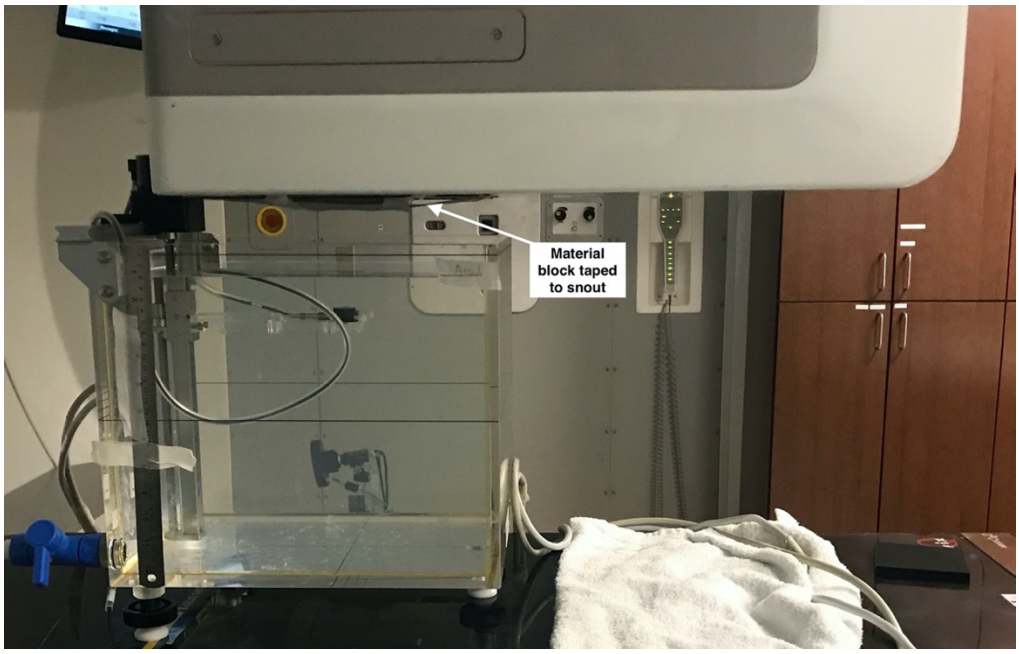

Figure 3.7: Example of proton measurement setup, using settings: gantry 0°, 8x8 cm^2 field size, 33x33 spots, 2.5 mm spot spacing, and 1 MU/spot.

The in-patient range correlates to the proton beam penetration depth in water. It is vendor defined by *Mevion* as "the 90% distal dose point (R_{90}) of a normalized depth dose curve" when measuring the depth dose distribution [56]. These values are measured as linear distances in water. Based on this definition, measurements were made by moving the ion chamber one millimeter in depth at a time to determine R_{90}. Each measurement was recorded as the values increased to a maximum, then as the values decreased, the R_{90} was determined by normalizing each value by the maximum value and linearly interpolating the depth of R_{90} using the 'Forecast' function in Excel. For each set 3D printed material measurements, one 10x10x1 cm^2 block was taped to the snout of the proton system, and measurements were made in the same way as the water measurements. These values show the relative range shift when compared to water alone. The thickness of the material blocks used were determined using a digital caliper. The height thickness of each side was measured at the center edge.

Proton Calculations

The average thickness of each block of material, $\bar{t}_{material}$, was determined using Equation 3.1 to get

$$\bar{t}_{material} = \frac{1}{4}\sum_{i=1}^{4}(t_{material,s})_i, \tag{3.37}$$

where $t_{material,s}$ is the thickness measurement for the given side, s, for the given material.

The relative stopping power for the given material, $RSP_{material}$, was then calculated using

$$RSP_{material} = \frac{R_{90,w} - R_{90,material}}{\bar{t}_{material}}, \tag{3.38}$$

where $R_{90,w}$ is the depth in water to the distal 90% dose point, $R_{90,material}$ is the depth in water, with the material taped to the snout, to the distal 90% dose point for the given material [33]. An example of each calculation is shown in Appendix B.

Proton Uncertainty Calculations

The uncertainty in the precision of the caliper used for the thickness measurements was given by the technical specifications sheet as 0.02 mm for measurements less than 100 mm. To determine the uncertainty in the thickness measurements for a given material based on the variance of the sides, $\sigma_{\bar{t}_{material}}$, Equation 3.3 was used to get

$$\sigma_{\bar{t}_{material}} = \sqrt{\frac{1}{4}\sum_{i=1}^{4}\left((t_{material,s})_i - \bar{t}_{material}\right)^2}. \tag{3.39}$$

The larger of the two uncertainties for the given material was used.

The equation to calculate the R_{90} values for each material, $R_{90,material}$, comes from Equation 3.24 to be

$$R_{90,material} = R_{low} + (D_{90} - D_{low})\left(\frac{R_{high} - R_{low}}{D_{high} - D_{low}}\right), \tag{3.40}$$

where R_{low} and R_{high} are the measured range values below and above the interpolated R_{90} value, respectively; D_{90} is the fraction of dose on the distal side of the Bragg Peak that is 90% of the max dose; and D_{low} and D_{high} are the measured dose values given as a fraction of the max dose below and above the interpolated D_{90} value. Before implementing these values into the uncertainty propagation equation, the uncertainty values for the variables were determined. The uncertainty of R_{low} and R_{high} was determined to be 1 mm, the water tank movement resolution. The dose values given as a fraction, D_x, were determined by

$$D_x = \frac{D}{D_{max}}, \tag{3.41}$$

where D is the dose given in nC, D_{max} is the maximum dose. The uncertainty of each dose value was determined by the uncertainty of the ion chamber by

$$\sigma_D = 0.013D. \tag{3.42}$$

These uncertainties were implemented to determine the uncertainty of the fractional dose, σ_{D_x}, by applying Equation 3.13 to Equation 3.40 to get

$$\sigma_{D_x} = D_x\sqrt{\left(\frac{\sigma_D}{D}\right)^2 + \left(\frac{\sigma_{D_{max}}}{D_{max}}\right)^2}, \tag{3.43}$$

where $\sigma_{D_{max}}$is the uncertainty of the maximum dose. After determining the uncertainties of the variables, Equation 3.17 was applied to Equation 3.39 to get the equation for the uncertainty of $R_{90,m}$, $\sigma_{R_{90,m}}$, given as

$$\sigma_{R_{90,material}} = \sqrt{\left(\frac{\partial R_{90,material}}{\partial R_{low}}\right)^2 \sigma_{R_{low}}^2 + \left(\frac{\partial R_{90,material}}{\partial R_{high}}\right)^2 \sigma_{d_{high}}^2 + \ldots} \quad (3.44)$$
$$\ldots + \left(\frac{\partial R_{90,m}}{\partial D_{low}}\right)^2 \sigma_{D_{low}}^2 + \left(\frac{\partial R_{90,material}}{\partial D_{high}}\right)^2 \sigma_{D_{high}}^2.$$

Given

$$\frac{\partial R_{90,material}}{\partial R_{low}} = \frac{D_{low} - D_{90}}{D_{low} - R_{high}},$$

$$\frac{\partial R_{90,material}}{\partial R_{high}} = \frac{(D_{low} - D_{90})(R_{low} - D_{high})}{D_{low} - R_{high}},$$

$$\frac{\partial R_{90,material}}{\partial D_{low}} = \frac{(R_{high} - D_{90})(R_{low} - D_{high})}{(D_{low} - R_{high})^2},$$

and

$$\frac{\partial R_{90,mateial}}{\partial D_{high}} = \frac{R_{high} - D_{90}}{R_{high} - D_{low}},$$

this becomes

$$\sigma_{R_{90,material}} =$$

$$\sqrt{\left(\frac{D_{low} - D_{90}}{D_{low} - R_{high}}\right)^2 \sigma_{R_{low}}^2 + \left(\frac{(D_{low} - D_{90})(R_{low} - D_{high})}{D_{low} - R_{high}}\right)^2 \sigma_{R_{high}}^2 + \cdots} \quad (3.45)$$
$$\ldots + \left(\frac{(R_{high} - D_{90})(R_{low} - D_{high})}{(D_{low} - R_{high})^2}\right)^2 \sigma_{D_{low}}^2 + \left(\frac{R_{high} - D_{90}}{R_{high} - D_{low}}\right)^2 \sigma_{D_{high}}^2,$$

where $\sigma_{R_{low}}$ and $\sigma_{R_{high}}$ are the uncertainties of the measured range values below and above the interpolated range value, respectively; and $\sigma_{D_{low}}$ and $\sigma_{D_{high}}$ are the uncertainties of the known fractional dose values below and above the interpolated fractional dose value, respectively.

The uncertainty of the RSP calculation was determined using Equation 3.17 to get

$$\sigma_{RSP} = \sqrt{\left(\frac{\partial(RSP)}{\partial R_{90,w}}\right)^2 \sigma_{R_{90,w}}^2 + \left(\frac{\partial(RSP)}{\partial R_{90,material}}\right)^2 \sigma_{R_{90,m}}^2 + \left(\frac{\partial(RSP)}{\partial \bar{t}_{material}}\right)^2 \sigma_{\bar{t}_{material}}^2}. \quad (3.46)$$

Given

$$\frac{\partial(RSP)}{\partial R_{90,w}} = \frac{1}{\bar{t}_{material}},$$

$$\frac{\partial(RSP)}{\partial R_{90,material}} = -\frac{1}{\bar{t}_{material}},$$

and

$$\frac{\partial(RSP)}{\partial \bar{t}_{material}} = \frac{R_{90,w} - R_{90,material}}{\bar{t}_{material}^2},$$

this becomes

$$\sigma_{RSP} = \sqrt{\left(\frac{1}{\bar{t}_{material}}\right)^2 \sigma_{R_{90,w}}^2 + \left(-\frac{1}{\bar{t}_{material}}\right)^2 \sigma_{R_{90,material}}^2 + \left(\frac{R_{90,w} - R_{90,material}}{\bar{t}_{material}^2}\right)^2 \sigma_{\bar{t}_{material}}^2}. \quad (3.47)$$

An example of each uncertainty calculation is given in Appendix B.

Density

Density Measurements

The mass of each block was measured on an *Ohaus* Harvard Trip balance (Model 5860-168). Three measurements were made for each block and averaged to obtain one mass value per block, using Equation 3.1 to get

$$\bar{m}_{material,n} = \frac{1}{3}\sum_{i=1}^{3}(m_n)_i, \quad (3.48)$$

where $\bar{m}_{material,n}$ is the average mass for the given material and block number, n, and m_n is each mass measurement for the given block. All measurements were averaged to obtain one mass value for each material, $\bar{m}_{material}$, using Equation 3.1 to get

$$\bar{m}_{material} = \frac{1}{24}\sum_{i=1}^{24}(m_{material,n})_i. \quad (3.49)$$

To prevent absorption, the blocks were coated in a waterproofing spray. For the volume measurements, a technique of displacement-of-water was used. A cylindrical container was used with a measured circumference of 41.5 cm. The radius was then found by

$$D = \frac{C}{\pi} = \frac{41.5\ cm}{\pi},$$

where D is the diameter and C is the circumference of the cylinder. The radius, R, was determined by

$$R = \frac{D}{2} = \frac{C}{2\pi} = \frac{20.75\ cm}{\pi}. \quad (3.50)$$

The volume of each block was then measured in the following way. Water was filled to a certain level, providing a relative 0 value. The block was then placed in the water in the container. Once the water surface settled, the change in height of the water surface was measured using a ruler from the relative 0 to the new water surface. This height value was called Δh. Using this value and the calculated radius, the volume of the block was determined by

$$\Delta V = \pi R^2 \Delta h = V_{material,n}, \quad (3.51)$$

where ΔV is the change in volume of the water, which is equal to the volume of the block for the given material and block number, $V_{material,n}$. The average volume for each material, $\bar{V}_{material}$, was determined by Equation 3.1 to get

$$\bar{V}_{material} = \frac{1}{8}\sum_{i=1}^{8}(V_{material,n})_i. \quad (3.52)$$

The effective density of each block for the given material, $\rho_{material,n}$, was determined by using the average mass and measured volume of the given block using

$$\rho_{material,n} = \frac{m_{material,n}}{V_{material,n}}. \tag{3.53}$$

The average effective density for the given material, $\bar{\rho}_{material}$, was then determined by

$$\bar{\rho}_{material} = \frac{1}{8}\sum_{i=1}^{8}(\rho_{material,n})_i. \tag{3.54}$$

An example of each calculation is shown in Appendix B.

Density Uncertainty Calculations

The uncertainty in each average block mass measurement was determined to be the standard deviation of the three measurements. Using Equation 3.3 this becomes

$$\sigma_{\bar{m}_{material,n}} = \sqrt{\frac{1}{3}\sum_{i=1}^{3}(m_i - \bar{m}_{material,n})^2}, \tag{3.55}$$

where $\sigma_{\bar{m}_{material,n}}$ is the uncertainty of the average mass value for the given block of material. The uncertainty for the average material mass, $\sigma_{\bar{m}_{material}}$, was determined by Equation 3.3 to get

$$\sigma_{\bar{m}_{material}} = \sqrt{\frac{1}{24}\sum_{i=1}^{24}((\bar{m}_{material,n})_i - \bar{m}_{material})^2}. \tag{3.56}$$

The uncertainty of the volume of a given block was determined by applying Equation 3.17 to Equation 3.38 to get

$$\sigma_{V_{material,n}} = \sqrt{\left(\frac{\partial R}{\partial V_{material,n}}\right)^2 \sigma_R^2 + \left(\frac{\partial(\Delta h)}{\partial V_{material,n}}\right)^2 \sigma_{\Delta h}^2}, \tag{3.57}$$

where $\sigma_{V_{material,n}}$ is the uncertainty in the volume of the given material and block, σ_R is the uncertainty in the radius of the cylinder used for the measurements, and $\sigma_{\Delta h}$ is the uncertainty in the height measurement. Given

$$\frac{\partial R}{\partial V_{material,n}} = 2\pi R\Delta h,$$

and

$$\frac{\partial(\Delta h)}{\partial V_{material,n}} = \pi R^2,$$

Equation 3.45 becomes

$$\sigma_{V_{material,n}} = \sqrt{(2\pi R\Delta h)^2\sigma_R^2 + (\pi R^2)^2\sigma_{\Delta h}^2}. \quad (3.58)$$

The uncertainty of the radius was derived from the uncertainty in the ruler used to measure the circumference of the circle, being 0.05 cm. This value was then propagated through the radius equation by using

$$\sigma_u = A\sigma_x, \quad (3.59)$$

for $u = Ax$, where A is a constant. Using Equation 3.46, where $\sigma_x = \sigma_C$, the uncertainty of the circumference, the uncertainty of the radius, σ_R, becomes

$$\sigma_R = \frac{\sigma_C}{2} = \frac{0.05\ cm}{2} = 0.025\ cm. \quad (3.60)$$

The uncertainty of Δh was determined by halving the smallest unit of the ruler used to make the measurements. To determine if this method was reasonable, the following experiment was done. Water was filled to the relative 0. A known volume of 200 mL of water was poured into the volume measurement container three separate times, and the height was measured. Each time the height was measured to be 1.45 cm. Using the known volume, the predicted Δh was calculated to by

$$\Delta V = \pi R^2 \Delta h.$$

Solving for Δh, and inputting ΔV=200 mL and $R = \frac{20.75\ cm}{\pi}$, the predicted Δh became

$$\Delta h = \frac{(200\ mL)\pi}{20.75^2} = 1.46\ cm.$$

The uncertainty of Δh would then be

$$1.46\ cm - 1.45\ cm = 0.01\ cm.$$

Since the uncertainty of Δh is larger when using the ruler uncertainty, $\sigma_{\Delta h}$ was determined to be 0.05 cm.

The uncertainty of the average volume measurement, $\sigma_{\bar{V}_{material}}$, was determined by Equation 3.3 to get

$$\sigma_{\bar{V}_{material}} = \sqrt{\frac{1}{8}\sum_{i=1}^{8}\left((V_{material,n})_i - \bar{V}_{material}\right)^2}. \quad (3.61)$$

The mass and volume uncertainties were propagated through the density equation for each block using Equation 3.22 to get

$$\sigma_{\rho_{material,n}} = \rho_{material,n}\sqrt{\left(\frac{\sigma_{m_{material,n}}}{m_{material,n}}\right)^2 + \left(\frac{\sigma_{V_{material,n}}}{V_{material,n}}\right)^2}, \quad (3.62)$$

where $\sigma_{\rho_{material,n}}$ is the uncertainy of the effective density for the given material and block. The uncertainty in the average effective density for the given material, $\sigma_{\bar{\rho}_{material}}$, was determined using Equation 3.3 to get

$$\sigma_{\bar{\rho}_{material}} = \sqrt{\frac{1}{8}\sum_{i=1}^{8}\left((\rho_{material,n})_i - \bar{\rho}_{material}\right)^2}. \quad (3.63)$$

An example of each uncertainty calculation is given in Appendix B.

CHAPTER IV

RESULTS

CT

Spool CT

Table 4.1 shows the result of CT scanning the spools of material. The materials which were printed are highlighted in gray.

Table 4.1: HU values of the spools of materials.

	Material	Min	Max	Mean	St. dev.
1	ABS	-602	-127	-240.2	72.79
2	Algae PLA	-751	29	-118.8	102.87
3	Amphora	-896	53	-191.3	184.85
4	Armadillo TPU	-430	5	-103.2	99.08
5	Carbon Fiber PLA	-538	-32	-172.9	87.72
6	Glow PLA	-282	39	-66.7	60.73
7	HIPS	-595	-176	-305.3	69.27
8	Nylon	-688	-54	-176.9	88.11
9	PET G	-101	98	61.4	38.77
10	PLA	-485	68	-53.4	75.97
11	Aluminum PLA	-505	13	-138.5	98.41
12	Iron PLA	962	1831	1473.7	204.62
13	PP	-754	-233	-361.7	70.65
14	PVA	-316	102	-27.9	76.84
15	SILK PLA	-425	49	-61.4	67.76
16	T-glase	-568	115	-39	87.04
17	TPU	-607	42	-104.7	95.77
18	Wood PLA	-92	102	50.9	57.07

The spool maximum HU values ranged from to -233 to 1831 and the minimum HU values ranged from -754 to 962. The max HU values of the materials printed ranged from -127 to 1831 and the minimum HU values ranged from -751 to 962. The standard

deviation for each material is very large due to the volume averaging of the spool with the surrounding air.

Block CT

Figure 4.1 shows the average HU values for two axial slices within each block of material. The circle marker represents the HU value of the first slice within the given block, and the square marker represents the HU value of the second slice within the given block. In general, the standard deviation of each HU value is small, and the HU values for the two slices within each block have a large spread, resulting in variable HU values for each material. Iron PLA has the largest spread in HU values, while TPU has the smallest spread in HU values.

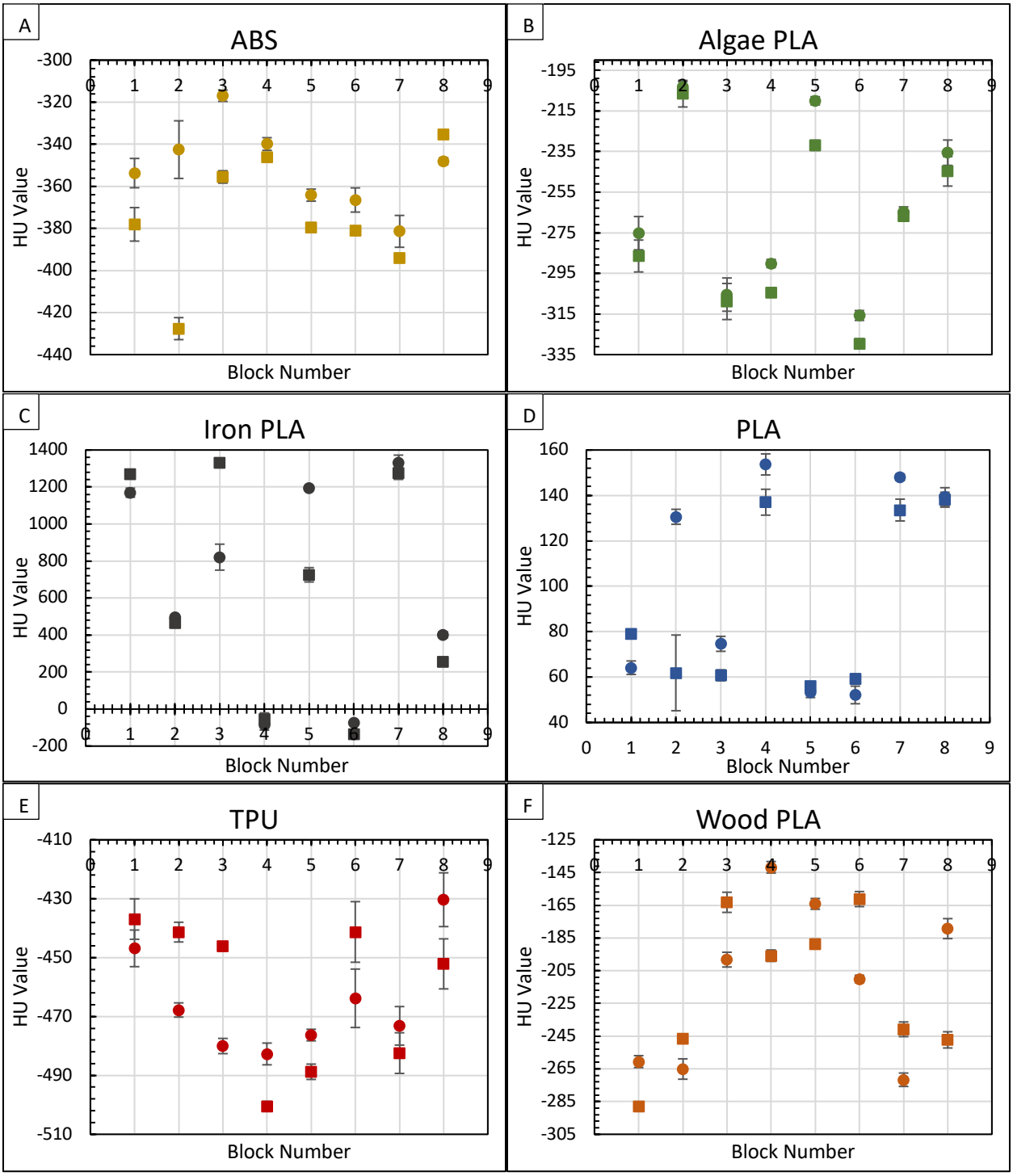

Figure 4.1: HU values for each block of material for (A) ABS, (B) Algae PLA, (C) Iron PLA, (D) PLA, (E) TPU, and (F) Wood PLA.

Electron

Figures 4.2 to 4.8 show the dose versus depth curves for the red, green, and blue color channels for each material and energy. Transparency of the method requires acquisition of individual color channels which are ultimately combined to provide a dose, based on calibration curves. The individual color channel dose curves are provided to follow the entire dose calculations from the acquired data. Each color channel is given by the color, while the associated uncertainty bars are in a darker shade of the color channel.

In general, the color channel dose curves are very close to one another, with each dose curve within the uncertainty of the other two dose curves. Each color channel dose curve has the same shape as the other dose curves, besides minor features caused by noise. The points of these noise features, however, have a larger uncertainty. Within the uncertainty of the points, the curves remain smooth. Examples of this are the two large dips in the blue channel dose curve of TPU for 12 MeV in Figure 4.6, C. The data points forming the dip have a larger uncertainty than the surrounding points.

Also present, are large dips and peaks in certain dose curves. When this occurs, the feature is shared by all three color channels. A large dip is present in Wood PLA (Figure 4.6) for example, in which the dip in dose becomes more prominent the higher the energy. However, in PLA (Figure 4.5), the dip in dose with depth becomes less prominent with higher energies.

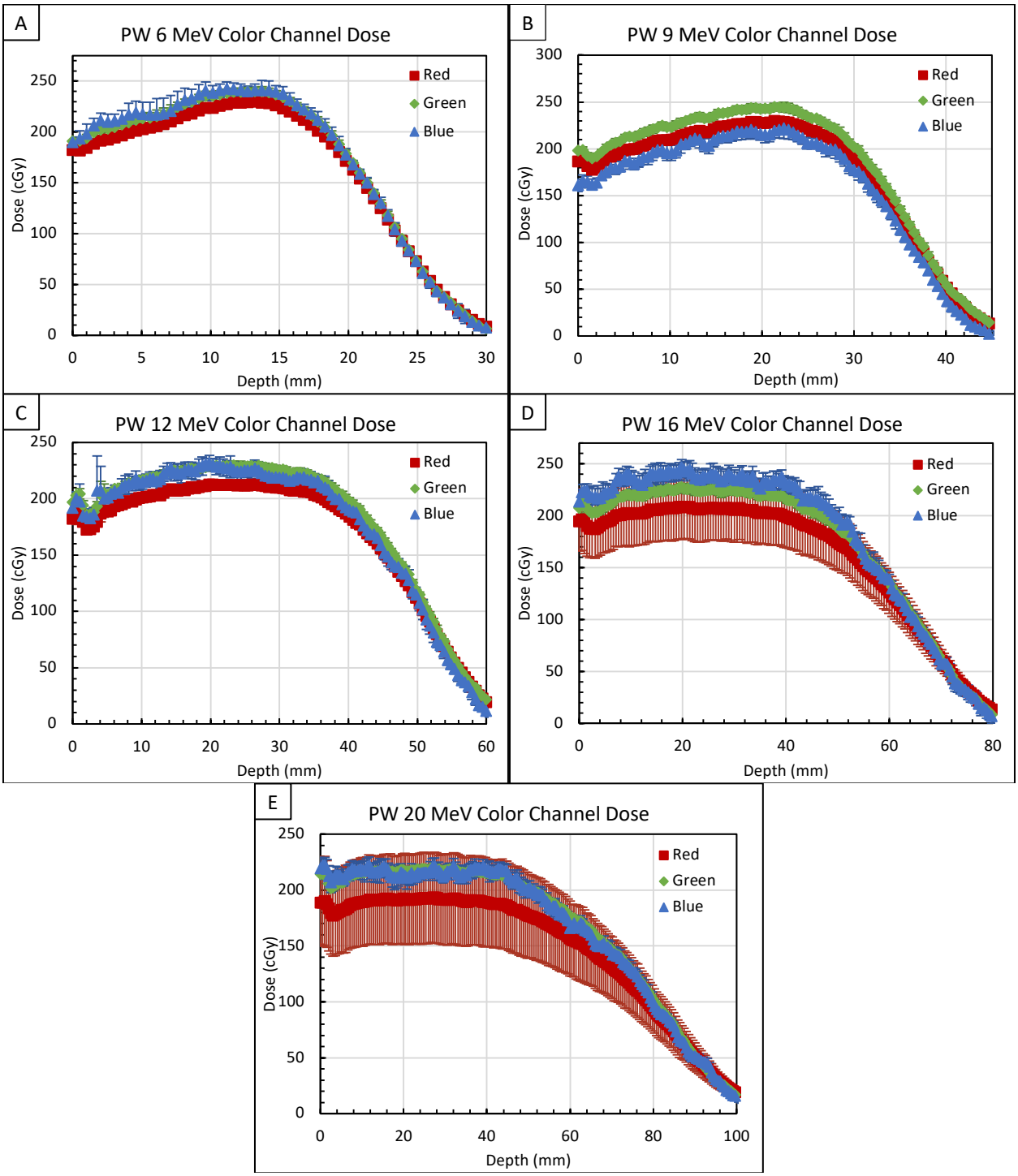

Figure 4.2: Dose versus depth curves of each color channel for plastic water for (A) 6 MeV, (B) 9 MeV, (C) 12 MeV, (D) 16 MeV, and (E) 20 MeV.

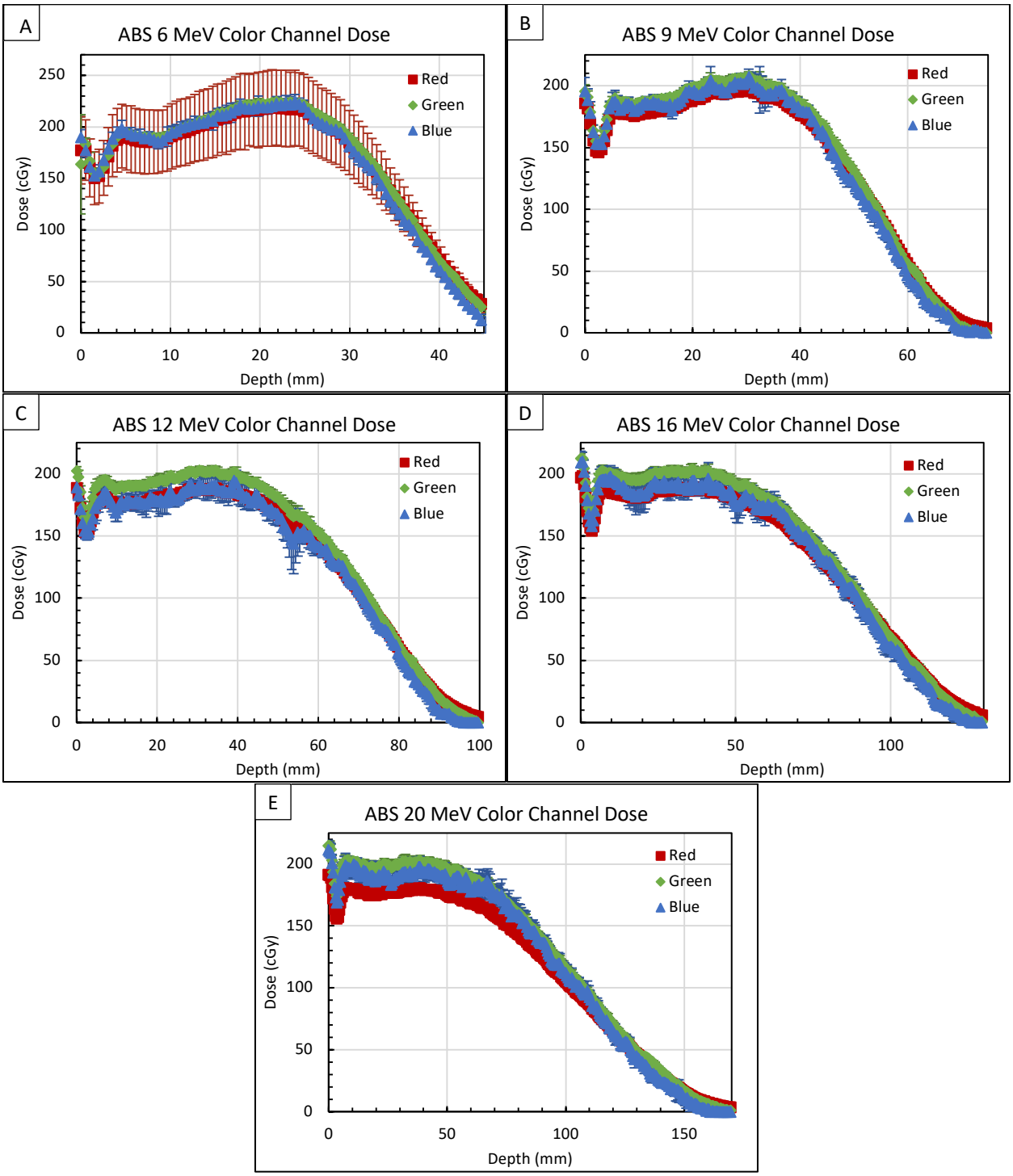

Figure 4.3: Dose versus depth curves of each color channel for ABS for (A) 6 MeV, (B) 9 MeV, (C) 12 MeV, (D) 16 MeV, and (E) 20 MeV using electron beam.

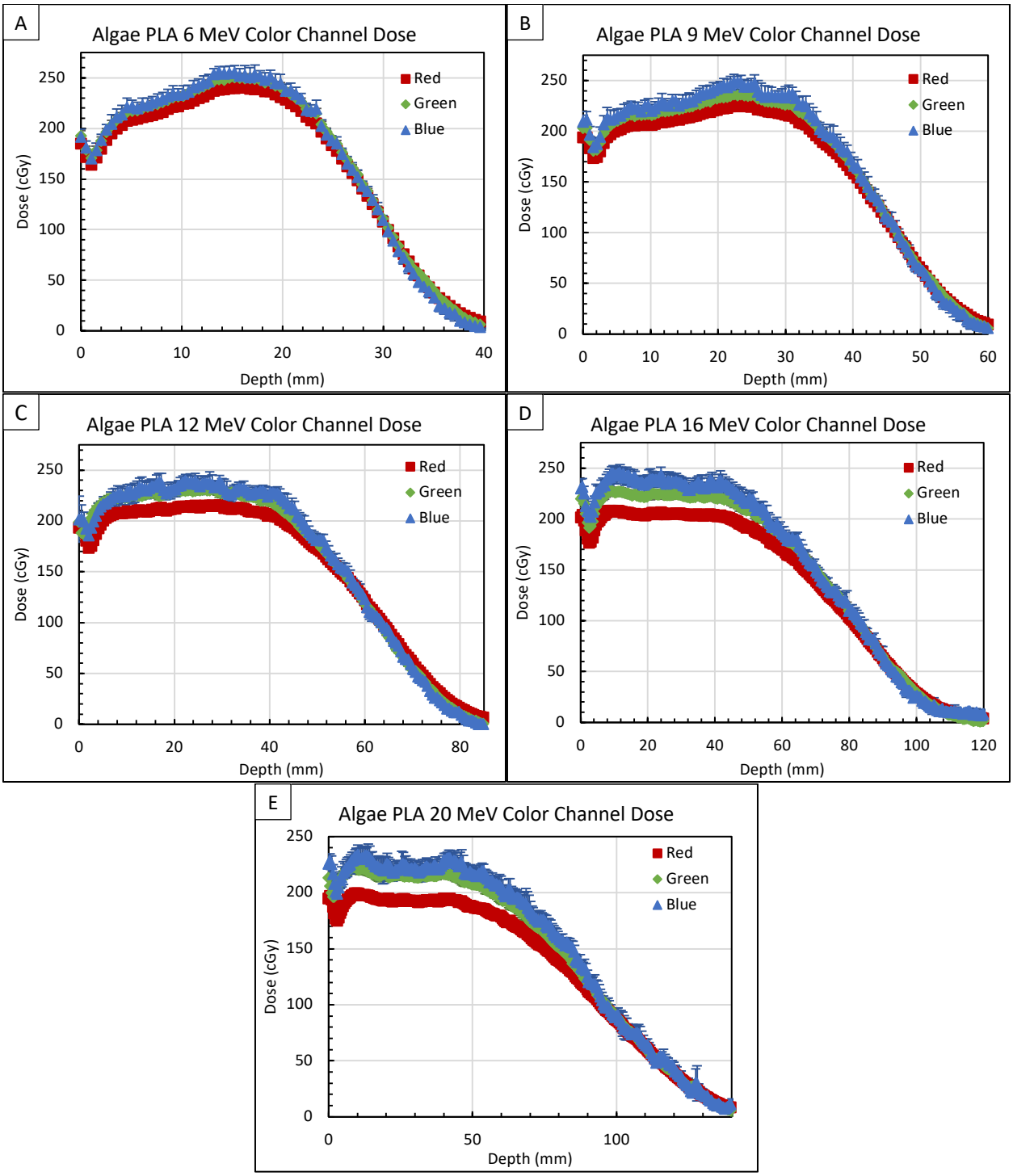

Figure 4.4: Dose versus depth curves of each color channel for Algae PLA for (A) 6 MeV, (B) 9 MeV, (C) 12 MeV, (D) 16 MeV, and (E) 20 MeV using electron beam.

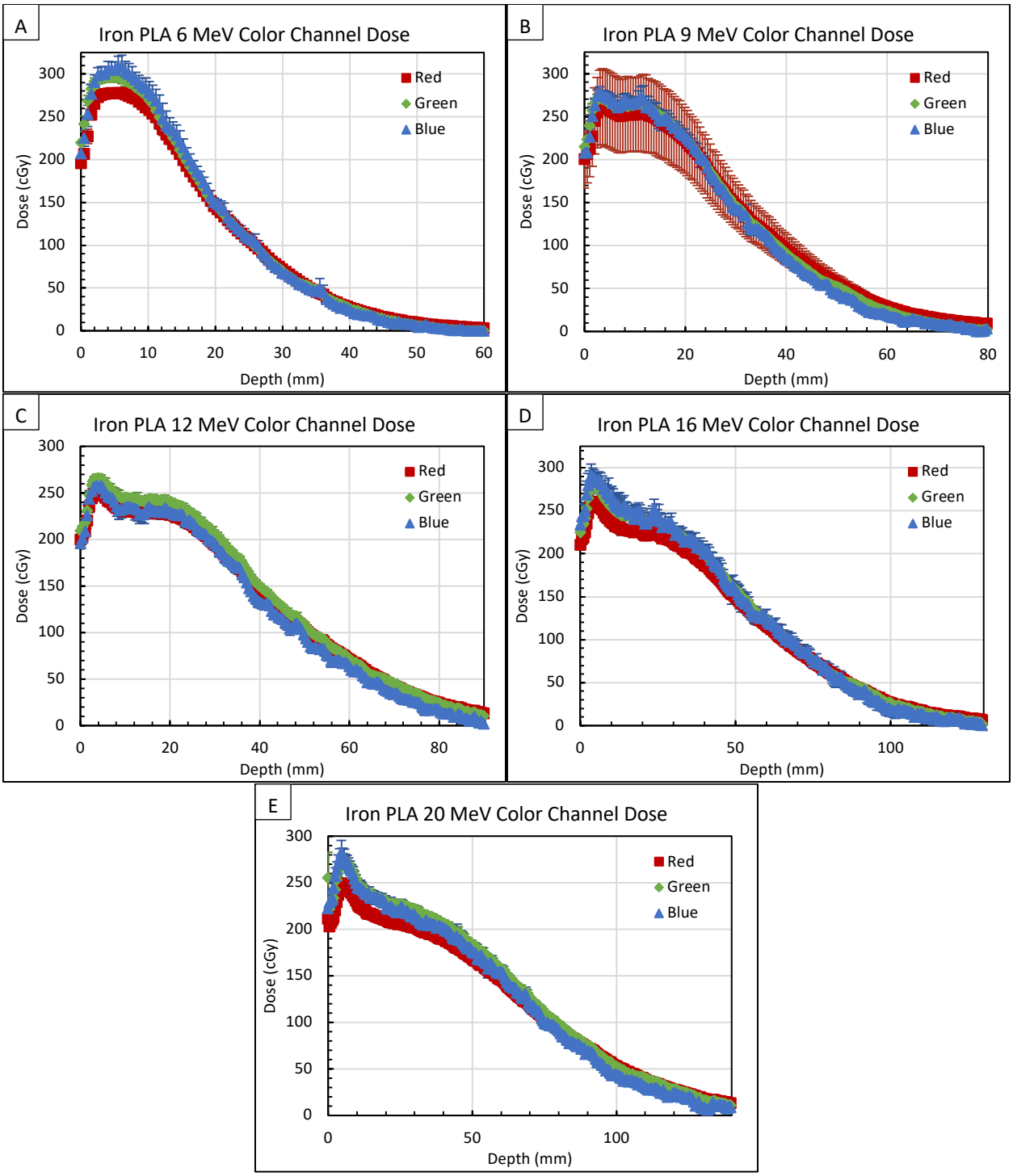

Figure 4.5: Dose versus depth curves of each color channel for Iron PLA for (A) 6 MeV, (B) 9 MeV, (C) 12 MeV, (D) 16 MeV, and (E) 20 MeV using electron beam.

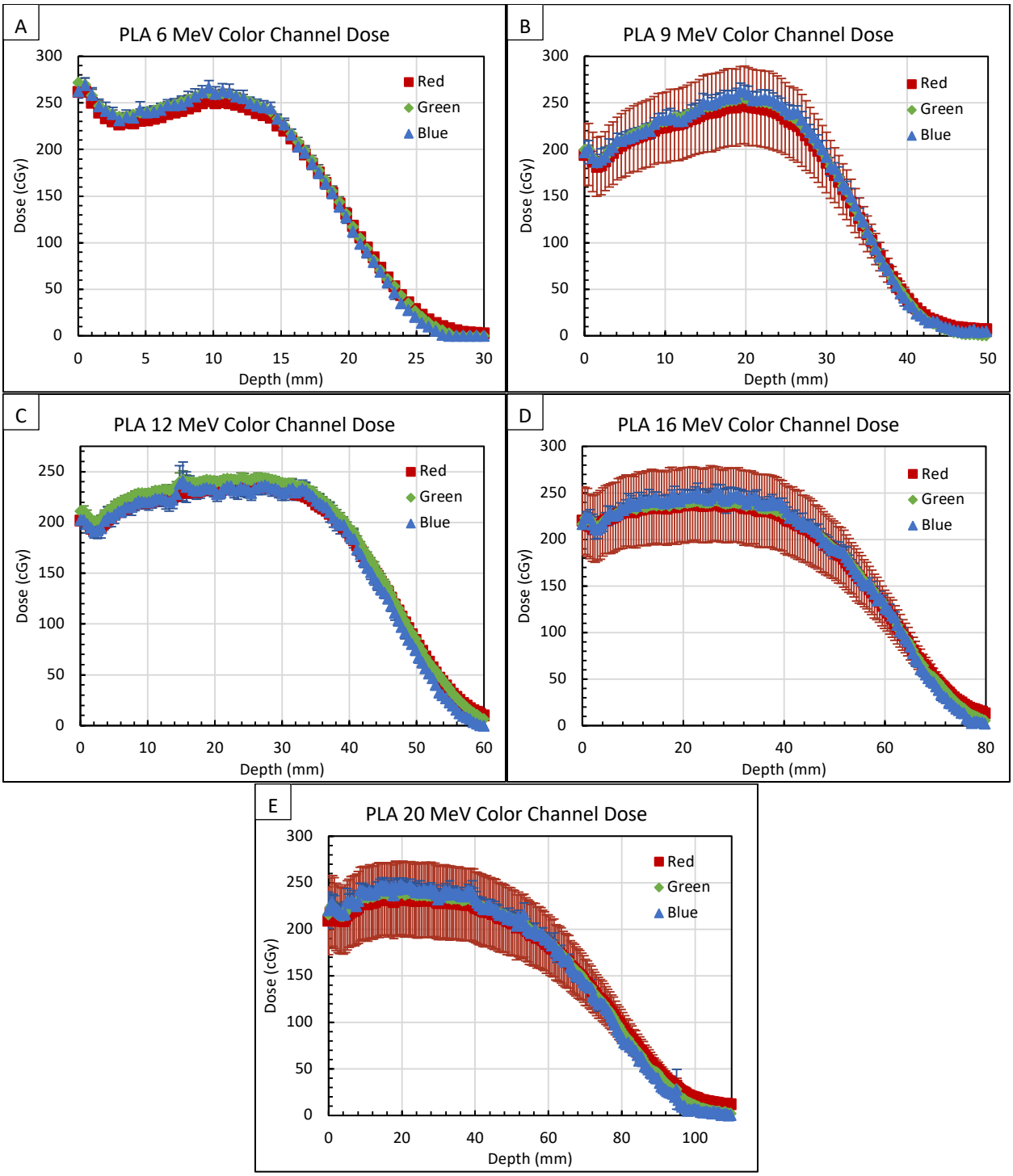

Figure 4.6: Dose versus depth curves of each color channel for PLA for (A) 6 MeV, (B) 9 MeV, (C) 12 MeV, (D) 16 MeV, and (E) 20 MeV using electron beam.

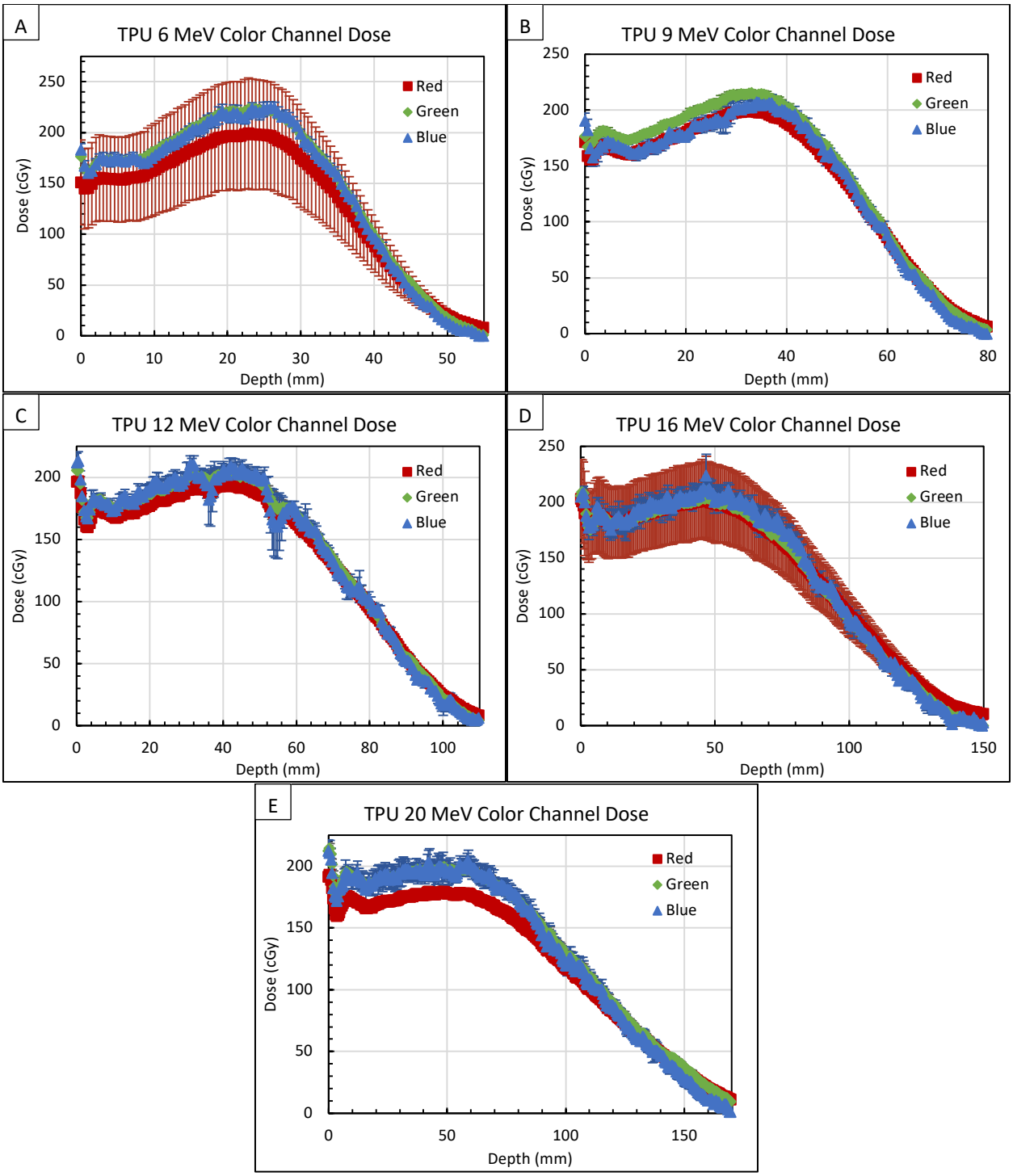

Figure 4.7: Dose versus depth curves of each color channel for TPU for (A) 6 MeV, (B) 9 MeV, (C) 12 MeV, (D) 16 MeV, and (E) 20 MeV using electron beam.

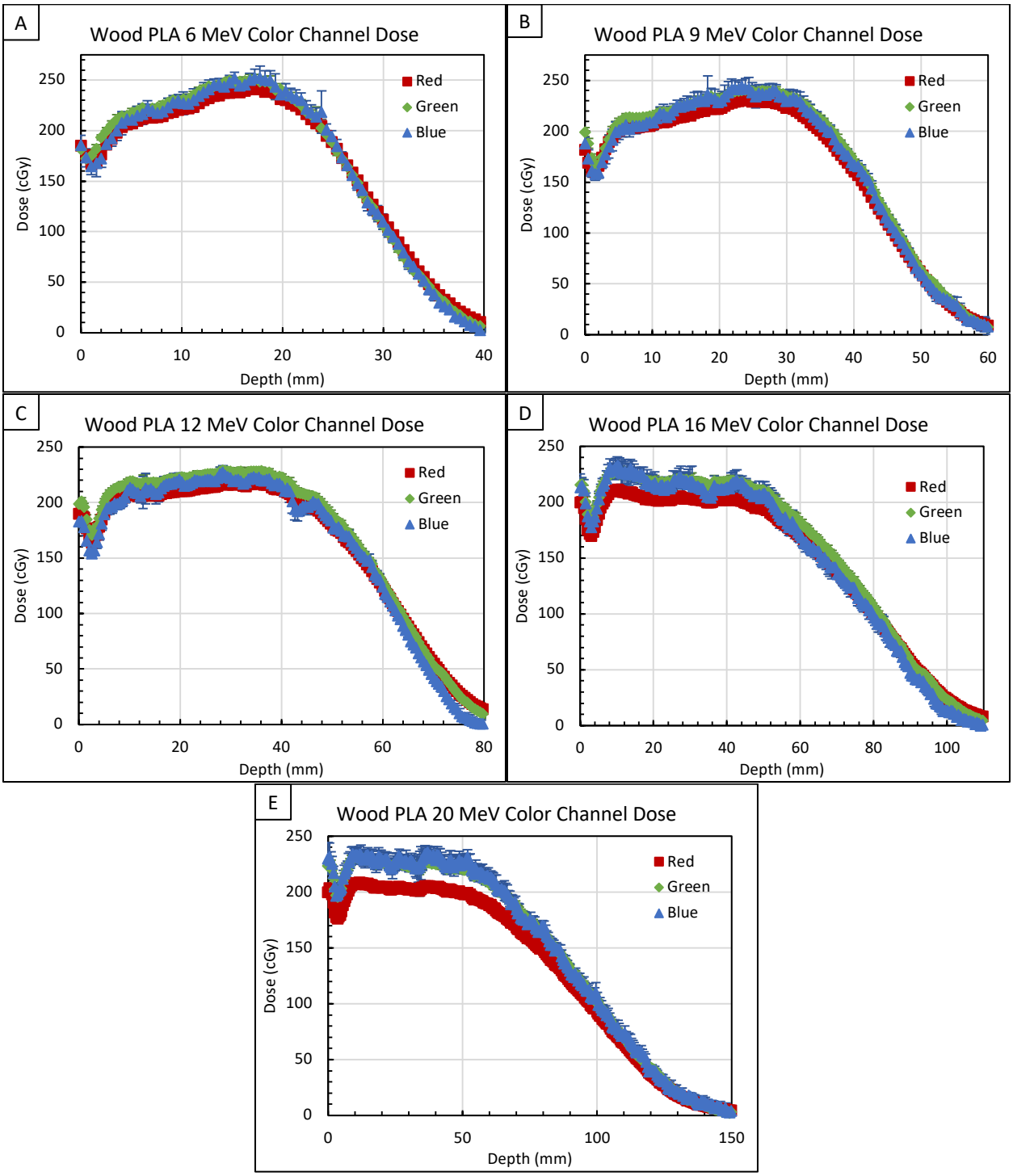

Figure 4.8: Dose versus depth curves of each color channel for TPU for (A) 6 MeV, (B) 9 MeV, (C) 12 MeV, (D) 16 MeV, and (E) 20 MeV using electron beam.

Photon

Figures 4.9 to 4.15 show the raw charge data for the materials for 6 MV and 18 MV.

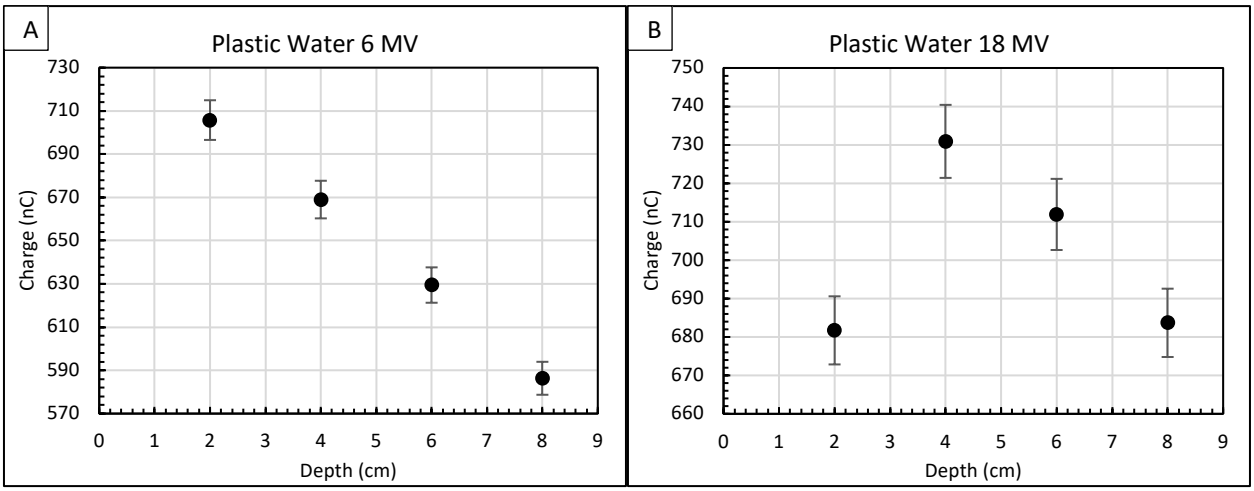

Figure 4.9: Raw charge data for plastic water for (A) 6 MV and (B) 18 MV using photon beam.

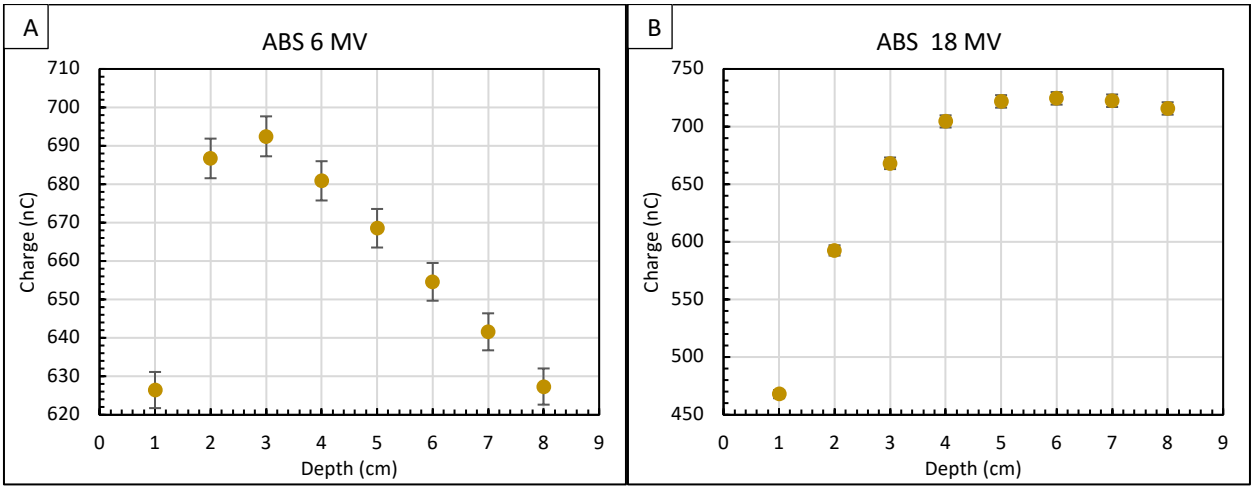

Figure 4.10: Raw charge data for ABS for (A) 6 MV and (B) 18 MV using photon beam.

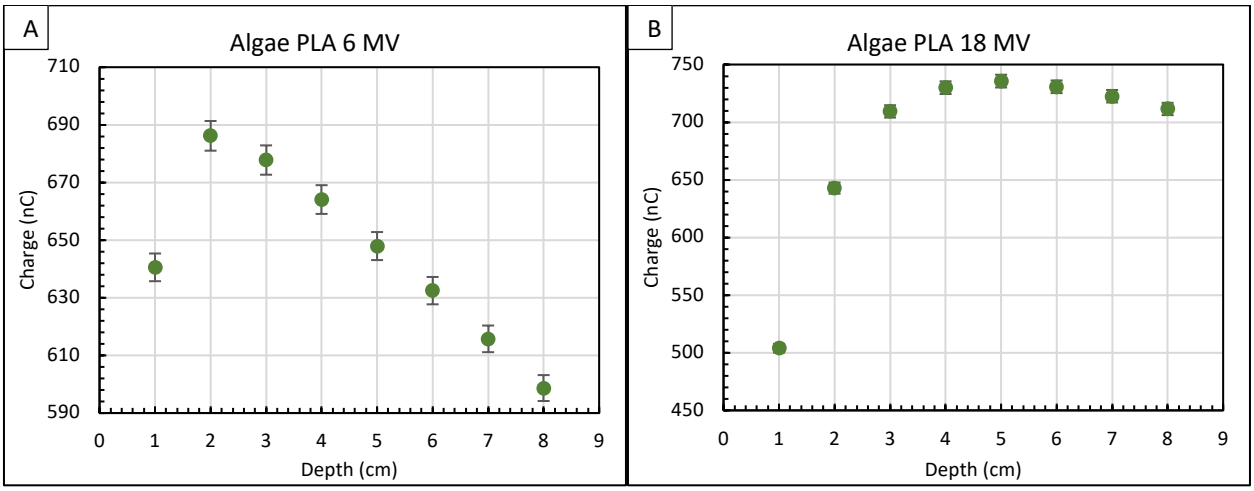

Figure 4.11: Raw charge data for Algae PLA for (A) 6 MV and (B) 18 MV using photon beam.

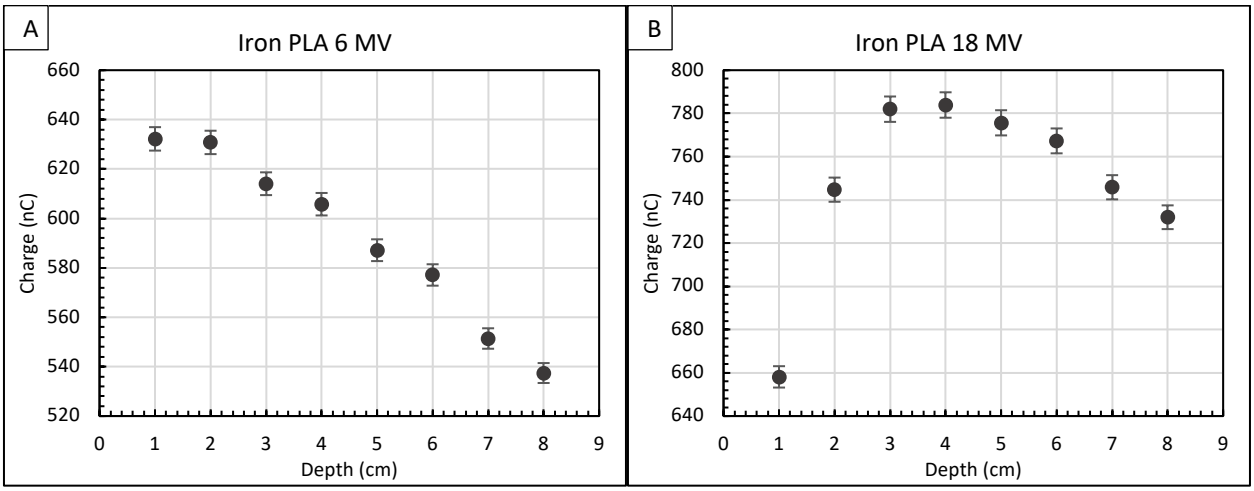

Figure 4.12: Raw charge data for Iron PLA for (A) 6 MV and (B) 18 MV using photon beam.

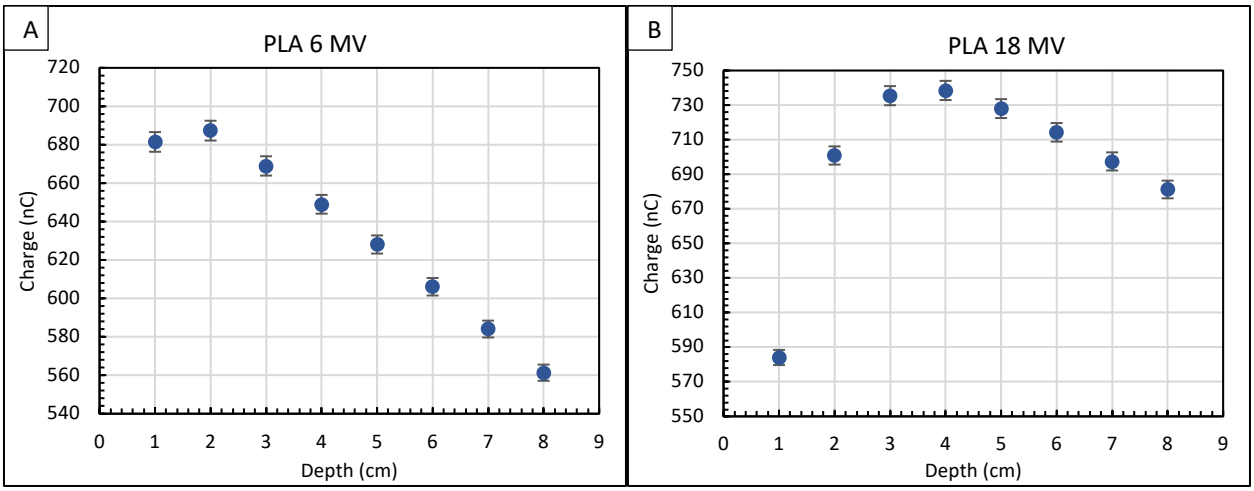

Figure 4.13: Raw charge data for PLA for (A) 6 MV and (B) 18 MV using photon beam.

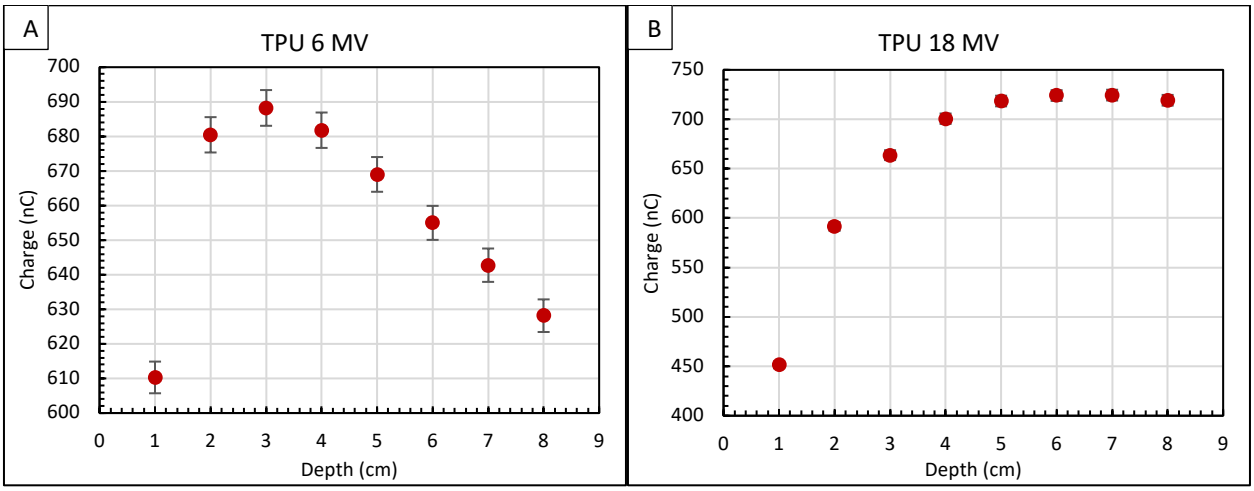

Figure 4.14: Raw charge data for TPU for (A) 6 MV and (B) 18 MV using photon beam.

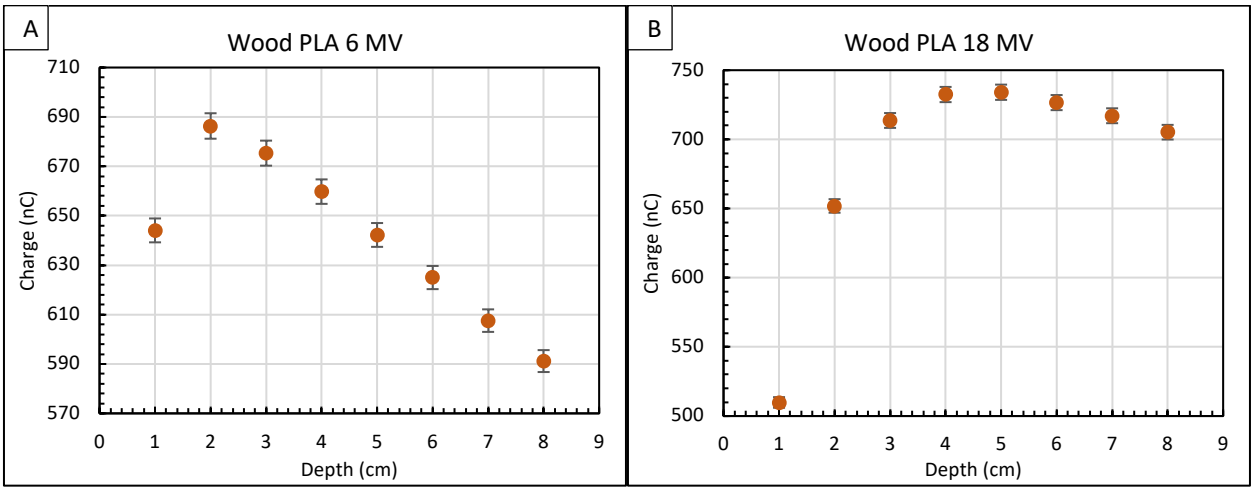

Figure 4.15: Raw charge data for Wood PLA for (A) 6 MV and (B) 18 MV using photon beam.

Each set of charge measurements has the trend of increasing to a maximum, then decreasing. The measurements for the 6 MV energy have a maximum at a shallower depth than the measurements for the 18 MV energy. All of the measurements create a smooth slope past the maximum with the exception of the Iron PLA. For this material, it can be seen by visual inspection that the slope between every other measurement point is not as steep as the general slope of the measurements for the 6 MV energy. The same can be seen to a lesser extent for the 18 MV measurements for Iron PLA.

Proton

Table 4.2 gives the range values of D_{90} for each material using proton beam. These values were found using the Excel function Forecast. The uncertainty values were found using Equation 3.42.

Table 4.2: D_{90} range values for each material.

		R_{90} (mm)		
Material	**Thickness (mm)**	**70.77 MeV**	**120.21 MeV**	**180.15 MeV**
Water	N/A	42.60 ± 0.1730	106.9 ± 0.06761	215.6 ± 0.03729
ABS	9.81 ± 0.0629	32.07 ± 0.2013	95.69 ± 0.07220	204.5 ± 0.03805
Algae PLA	10.29 ± 0.05802	35.69 ± 0.2073	99.35 ± 0.07218	208.2 ± 0.03784
Iron PLA	10.17 ± 0.06076	30.29 ± 0.2428	93.67 ± 0.07660	202.1 ± 0.03871
PLA	10.10 ± 0.03775	32.07 ± 0.2278	95.69 ± 0.07513	204.5 ± 0.03867
TPU	9.96 ± 0.02	37.07 ± 0.1955	100.8 ± 0.07150	209.5 ± 0.03798
Wood PLA	10.30 ± 0.03000	35.33 ± 0.2146	99.12 ± 0.0944	208 ± 0.09562

The materials were printed to be 10 mm thick. The measured thicknesses of ABS, Algae PLA, Iron PLA, and Wood PLA did not fall within the 0.1 mm printer resolution. The thickness of ABS was smaller than 10 mm due to shrinking, a common problem when printing the material. The measured thicknesses of all PLA materials were larger than 10 mm, while the measured thickness of TPU was within the uncertainty of the printer resolution. The difference could be due to the print speed, because the TPU was printed at a much lower speed, which could be attributed to the higher geometric accuracy. The R_{90} values for each printed material blocks increase with increased energy. The range of R_{90} values between materials also increase with increasing energy.

Density

Figures 4.16 to 4.21 show the mass and volume of each block, and the average mass and volume of each material. The thicker red line in each graph represents the

average, determined by Equations 3.36 and 3.40 for mass and volume, respectively, and the thinner red lines are the average uncertainty bands determined by Equations 3.44 and 3.46.

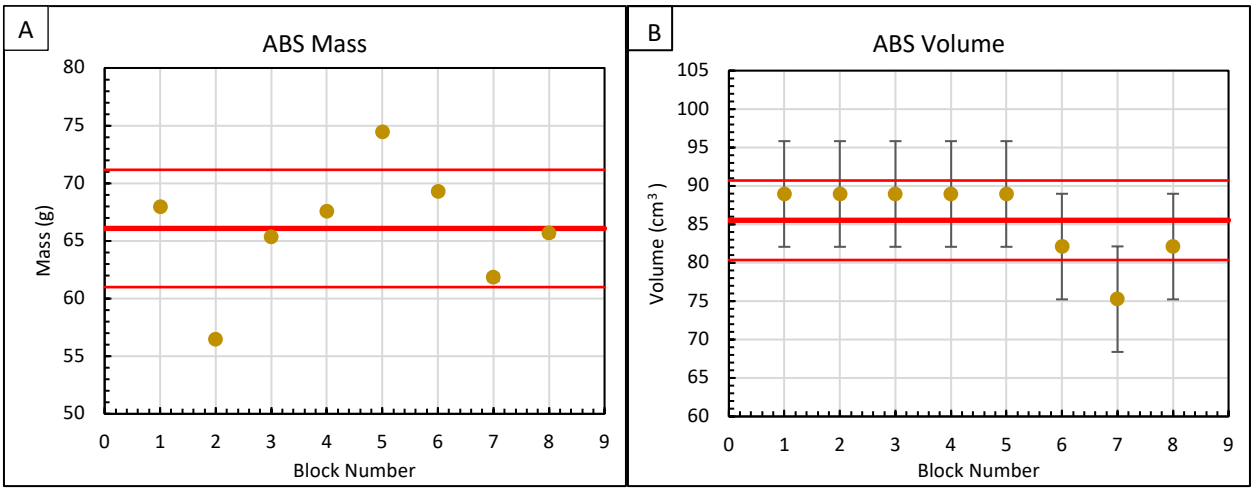

Figure 4.16: (A) The mass values and (B) the volume values for each block of ABS that were used to calculate the effective density.

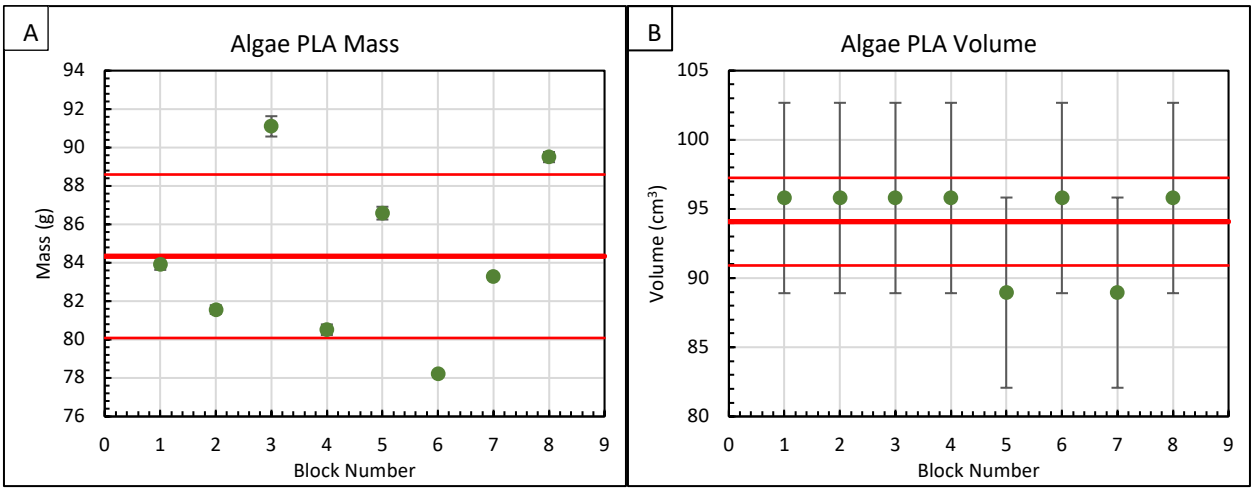

Figure 4.17: (A) The mass values and (B) the volume values for each block of Algae PLA that were used to calculate the effective density.

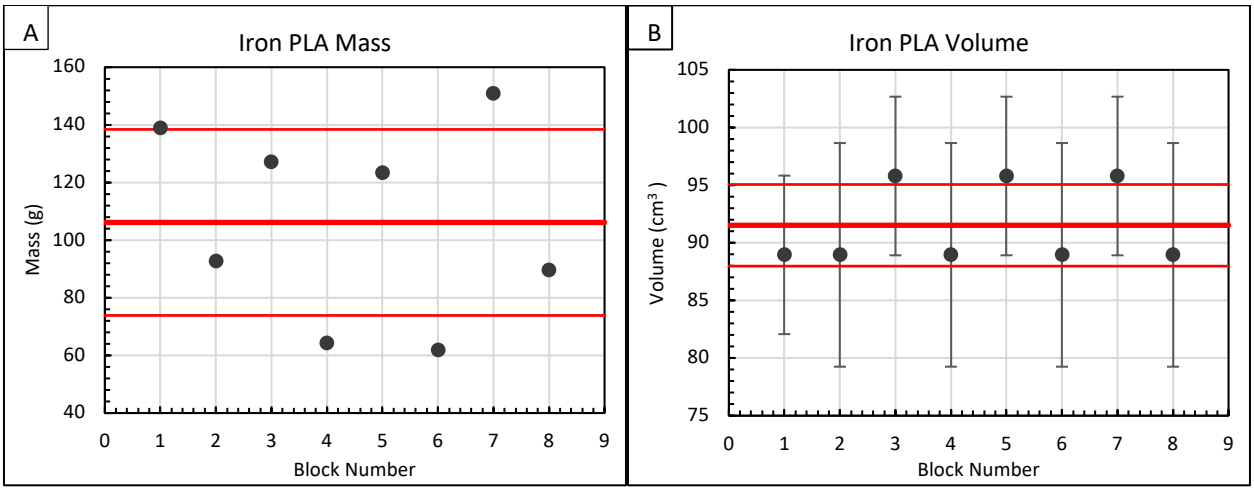

Figure 4.18: (A) The mass values and (B) the volume values for each block of Iron PLA that were used to calculate the effective density.

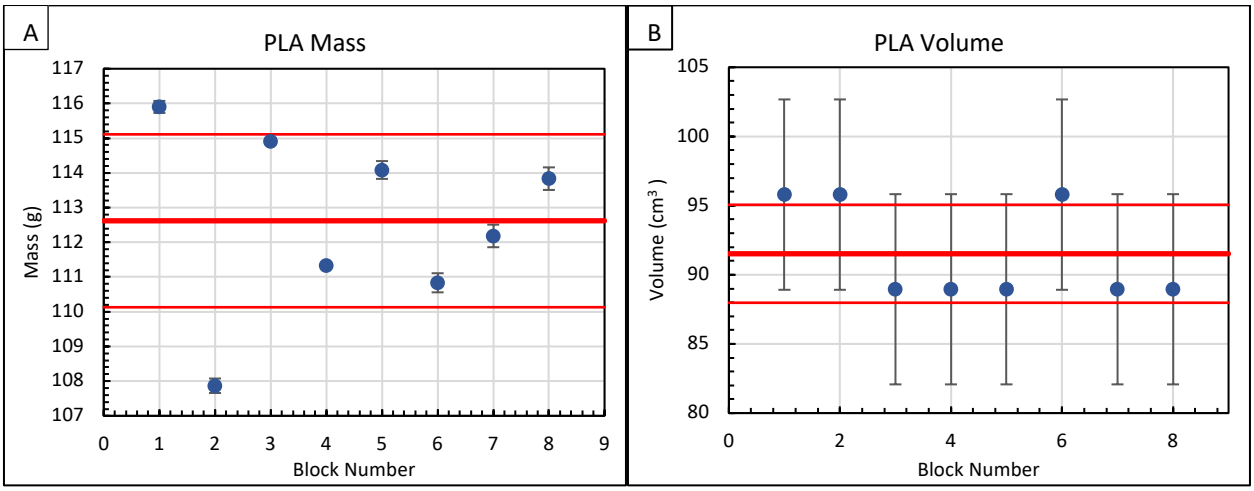

Figure 4.19: (A) The mass values and (B) the volume values for each block of PLA that were used to calculate the effective density.

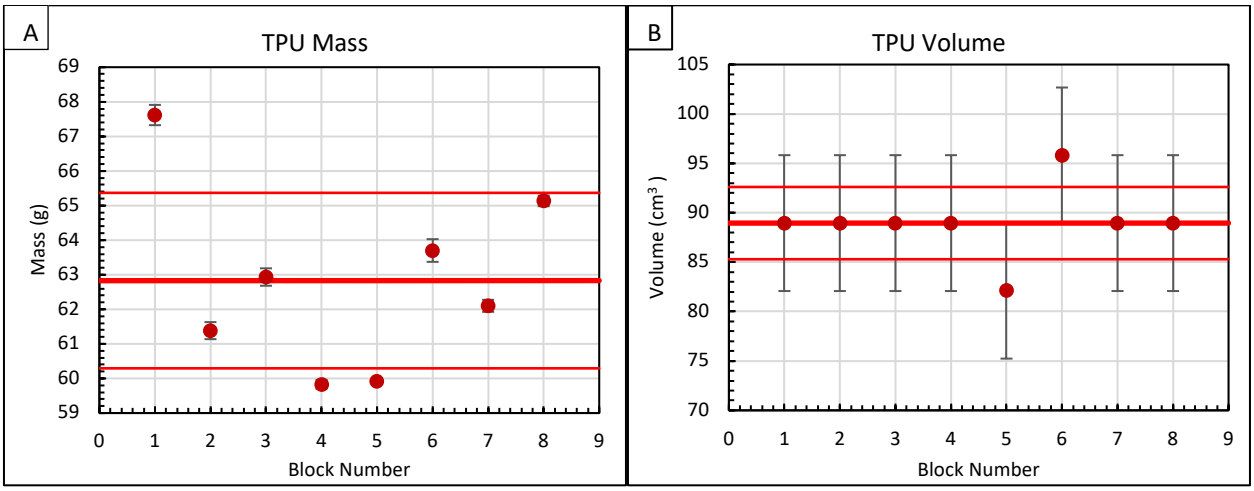

Figure 4.20: (A) The mass values and (B) the volume values for each block of TPU that were used to calculate the effective density.

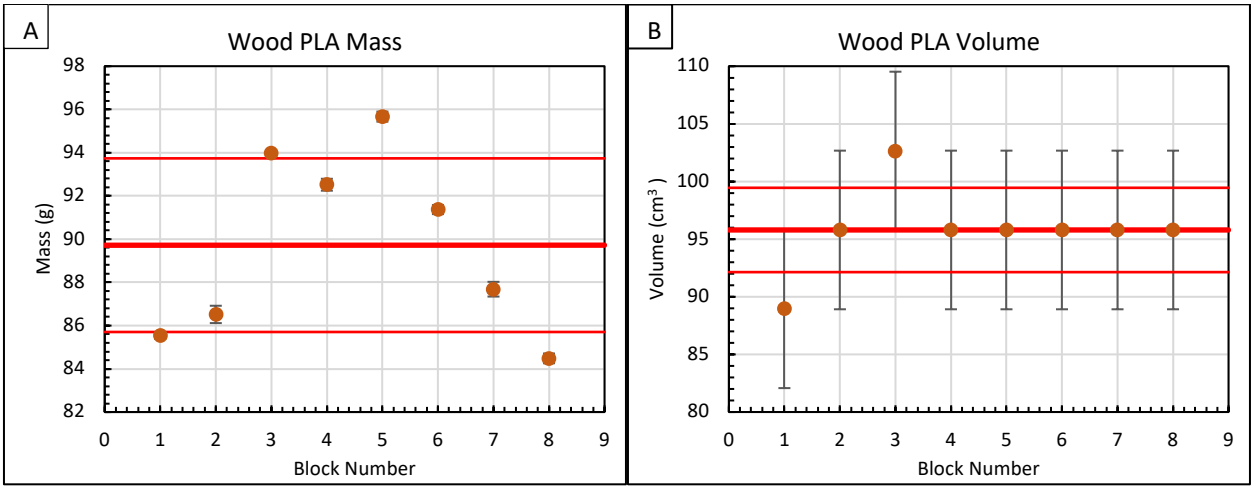

Figure 4.21: (A) The mass values and (B) the volume values for each block of Wood PLA that were used to calculate the effective density.

The mass and volume measurements varied between blocks due to the cutting of the blocks. The measurements were made after the original blocks were cut in half. Using the band saw caused some loss of material, causing the blocks to vary slightly in volume in addition to the potential variance prior to the cutting. The mass measurements were consistent within each block, giving small uncertainty. The uncertainty of each volume value was relative larger due to propagating the uncertainty of two measurements through the volume calculation.

CHAPTER V

ANALYSIS AND DISCUSSION

3D printing the materials

Each material was printed in accordance with manufacturer suggested print temperatures and speed, and adjusting as needed, obtaining the values in Table 3.1. The materials with a PLA base were simple to print, as they did not require a heated bed or different print speeds. Also, no warping issues were encountered. This is with the exception of one print attempt, in which the printer was left alone after being monitored through approximately 20% of the print. Upon arrival the next morning, the printer was surrounded by hardened Algae PLA. It seemed from the resulting mess that the printer nozzle had gotten off track, causing the hot nozzle to begin to dig into the printed block, melting plastic through its path, and ultimately causing the material to hardening up through the printer head and around the nozzle. Figure 5.1 shows the results of the botched print.

Figure 5.1: (A) Botched printed block (B) Filament hardened around the print head.

The Iron PLA printed without issues, but after printing, it was obvious the last two blocks printed differently than the first two. The last two blocks felt lighter and were more brittle. The first two blocks and last two blocks came from different spools, but were printed with the same print settings and ambient surroundings.

The TPU material printed smoothly, but at a print speed of 30 mm/s (Table 3.1), only ~33% the speed of the PLA materials. The ABS material blocks warped slightly at the corners as the block printed, due to the edges coming up slightly from the print bed. This could have possibly been prevented if an enclosure had been constructed about the printer in, reducing the temperature gradient of the ambient surroundings.

CT

The HU values of the slices within each block were used to determine the average HU value for the given material using Equation 3.2. These values are shown in Figure 5.2. The average HU value for the given material is the thicker red line, and the thinner red lines are the average uncertainty bands. The uncertainty of the average value was determined by Equation 3.4, given by 1σ on the graph. The average HU value is labelled below the red line representing the average to the right. The circle markers represent the HU values of the first measured slice within the given block, and the square markers represent the HU values of the second slice.

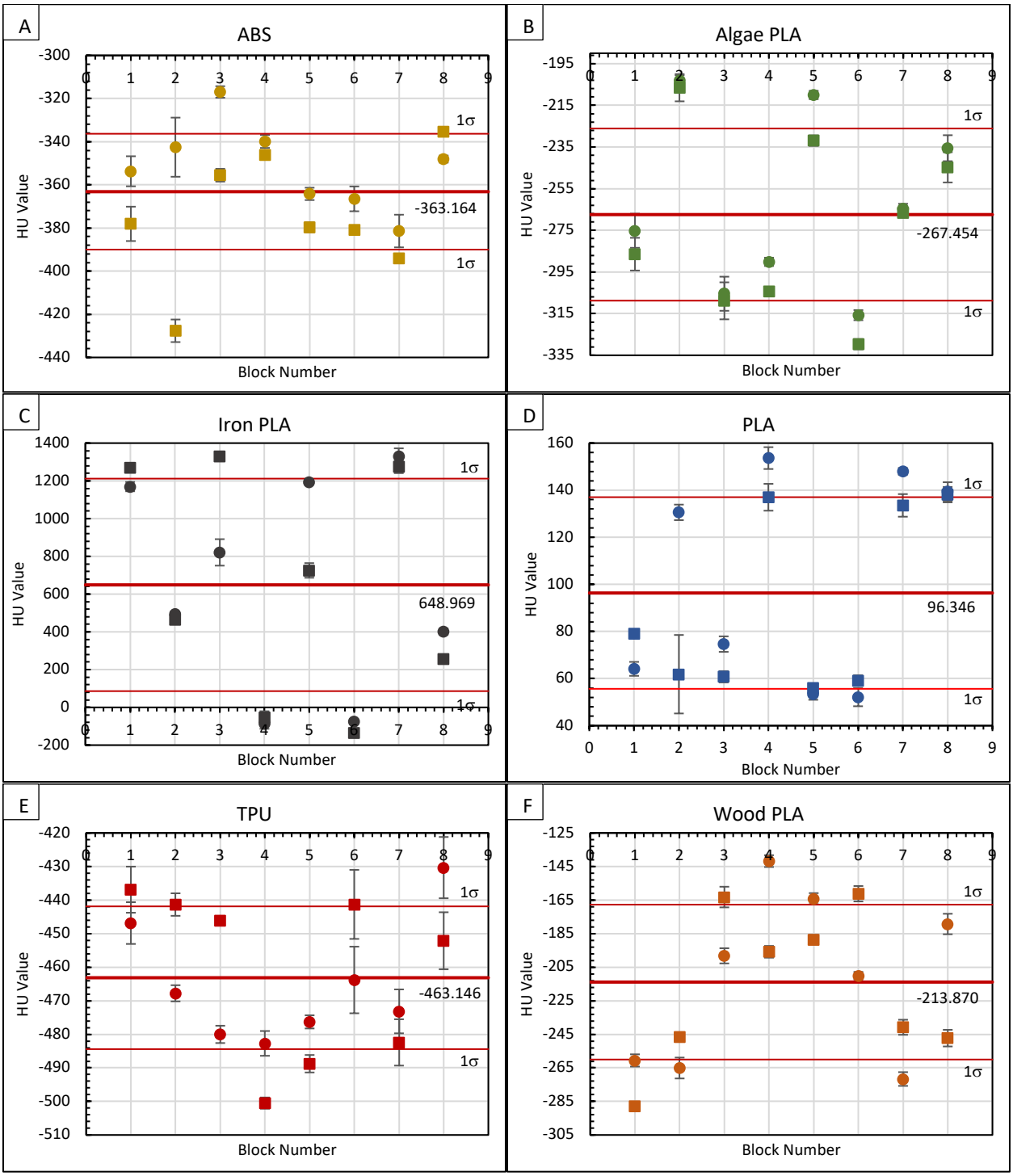

Figure 5.2: The HU values of the individual blocks and the average values of the materials for (A) ABS, (B) Algae PLA, (C) Iron PLA, (D) PLA, (E) TPU, and (F) Wood PLA.

The average HU values of the printed materials were compared with the HU values of the material spool. It was thought that the maximum HU value of the material spool

may correspond with the average HU value of the printed material. However, there was no connection between the average HU value of the material to that of spooled material, due to the large amount of in-spool air gaps involved. This is emphasized by the large standard deviation values of the average HU values of the material spools.

The HU values between the blocks, and occasionally within a given block, span an extended range. The majority of blocks are poorly defined by a single HU value, and no material demonstrated a controlled range of HU values. Treatment planning systems heavily rely on the HU values of materials to accurately determine dose distributions. Even in the case that the HU value in the TPS can be overridden by the user to aid in improving the accuracy of the dose, the large variation in HU values that each material exhibits would make it very difficult to implement a 3D printed material's HU value to calculate an accurate dose distribution when using a 3D printed object in patient treatment, for example a bolus, because using the average HU value may not be a true representation of material. As commercially available 3D printed bolus systems exist [59], the HU values of these printed materials are likely a function of the printer and print settings, in addition to the filament type and manufacturer.

Electron

Figures 5.3 to 5.9 show the PDD curves for each material and energy. Using the color channel dose values, the PDD values were calculated using Equation 3.12, and the associated uncertainty values were determined using Equation 3.23.

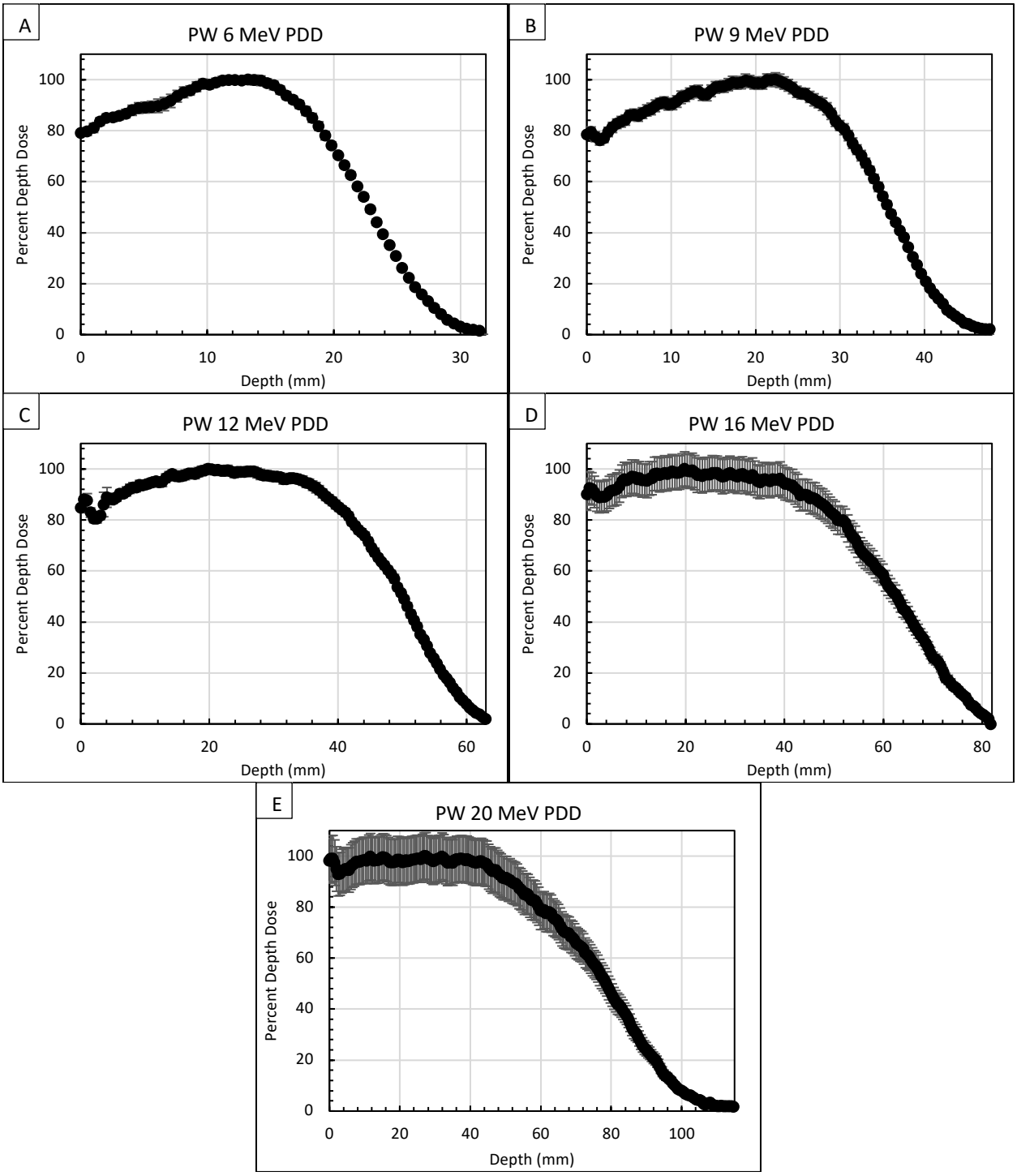

Figure 5.3: PDD curves for Plastic Water for (A) 6 MeV, (B) 9 MeV, (C) 12 MeV, (D) 16 MeV, and (E) 20 MeV.

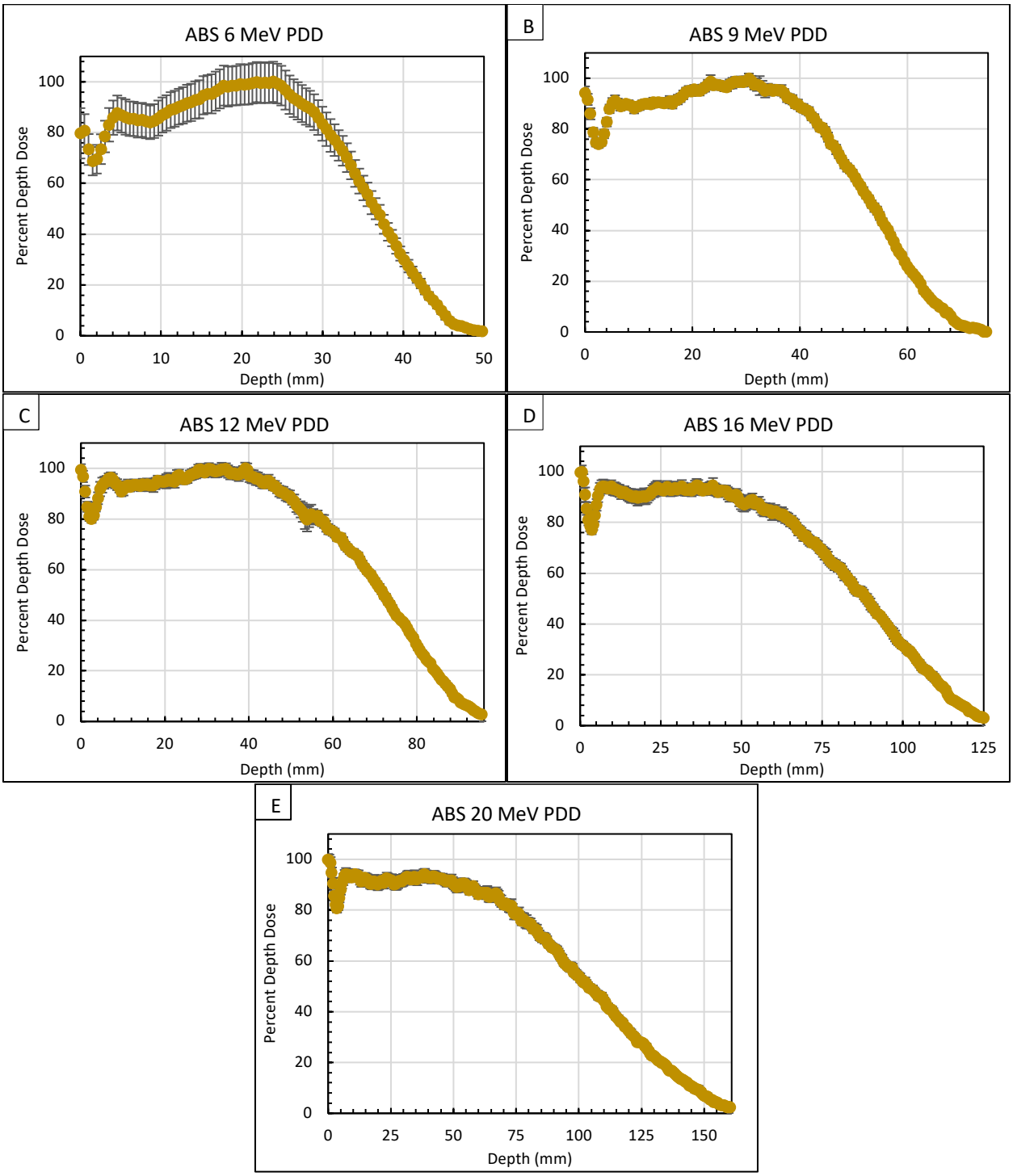

Figure 5.4: PDD curves for ABS for (A) 6 MeV, (B) 9 MeV, (C) 12 MeV, (D) 16 MeV, and (E) 20 MeV.

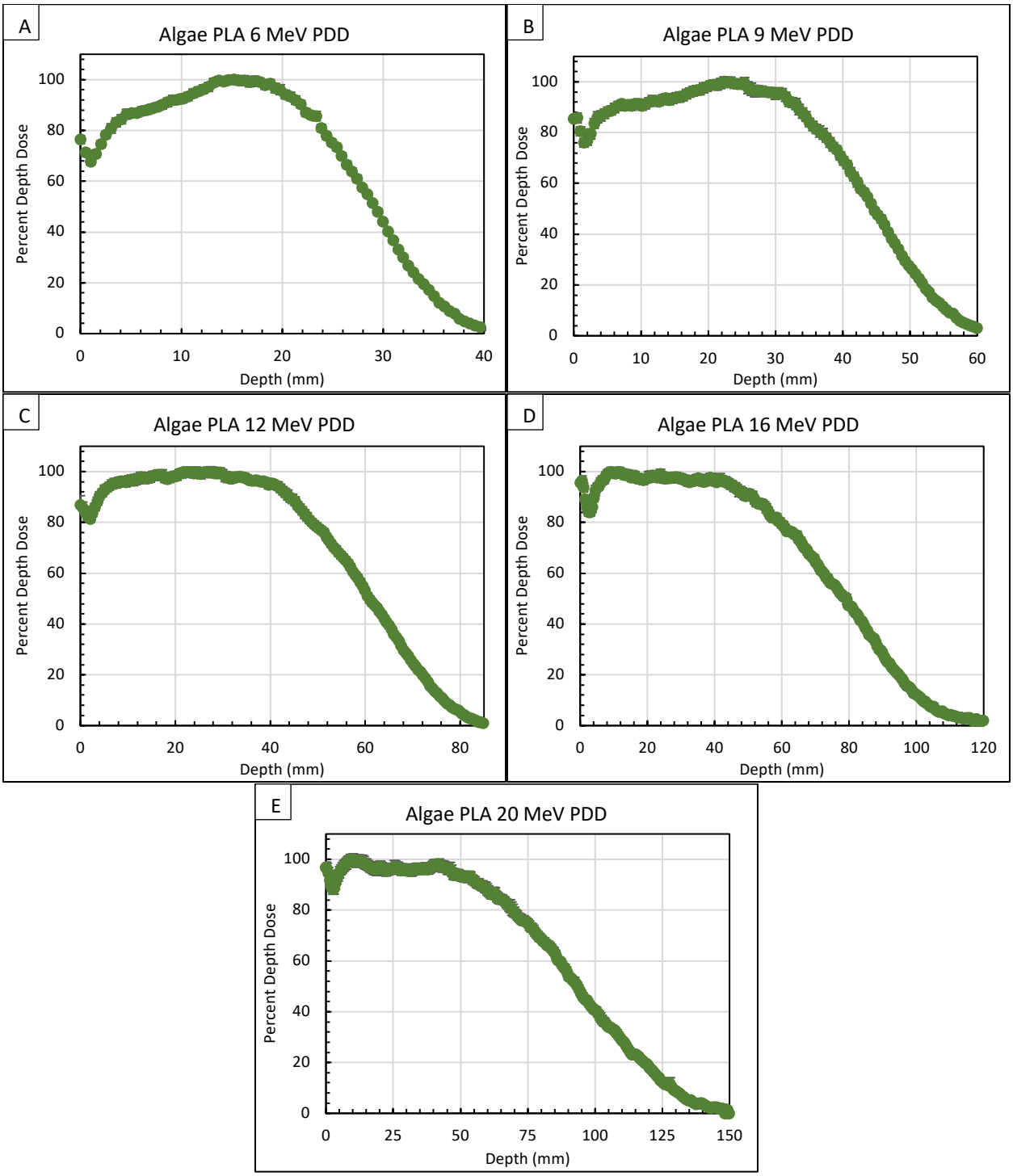

Figure 5.5: PDD curves for Algae PLA for (A) 6 MeV, (B) 9 MeV, (C) 12 MeV, (D) 16 MeV, and (E) 20 MeV.

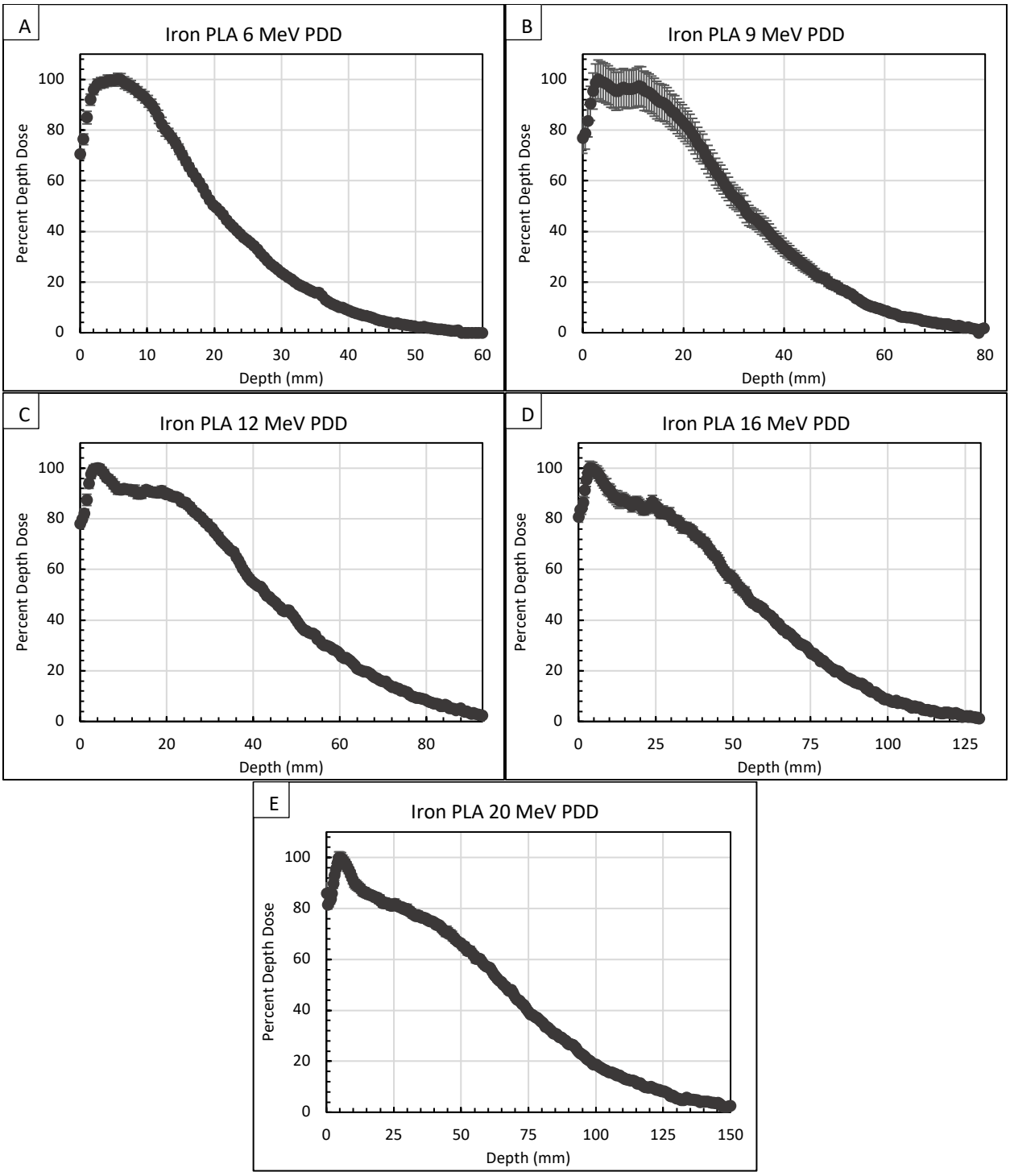

Figure 5.6: PDD curves for Iron PLA for (A) 6 MeV, (B) 9 MeV, (C) 12 MeV, (D) 16 MeV, and (E) 20 MeV.

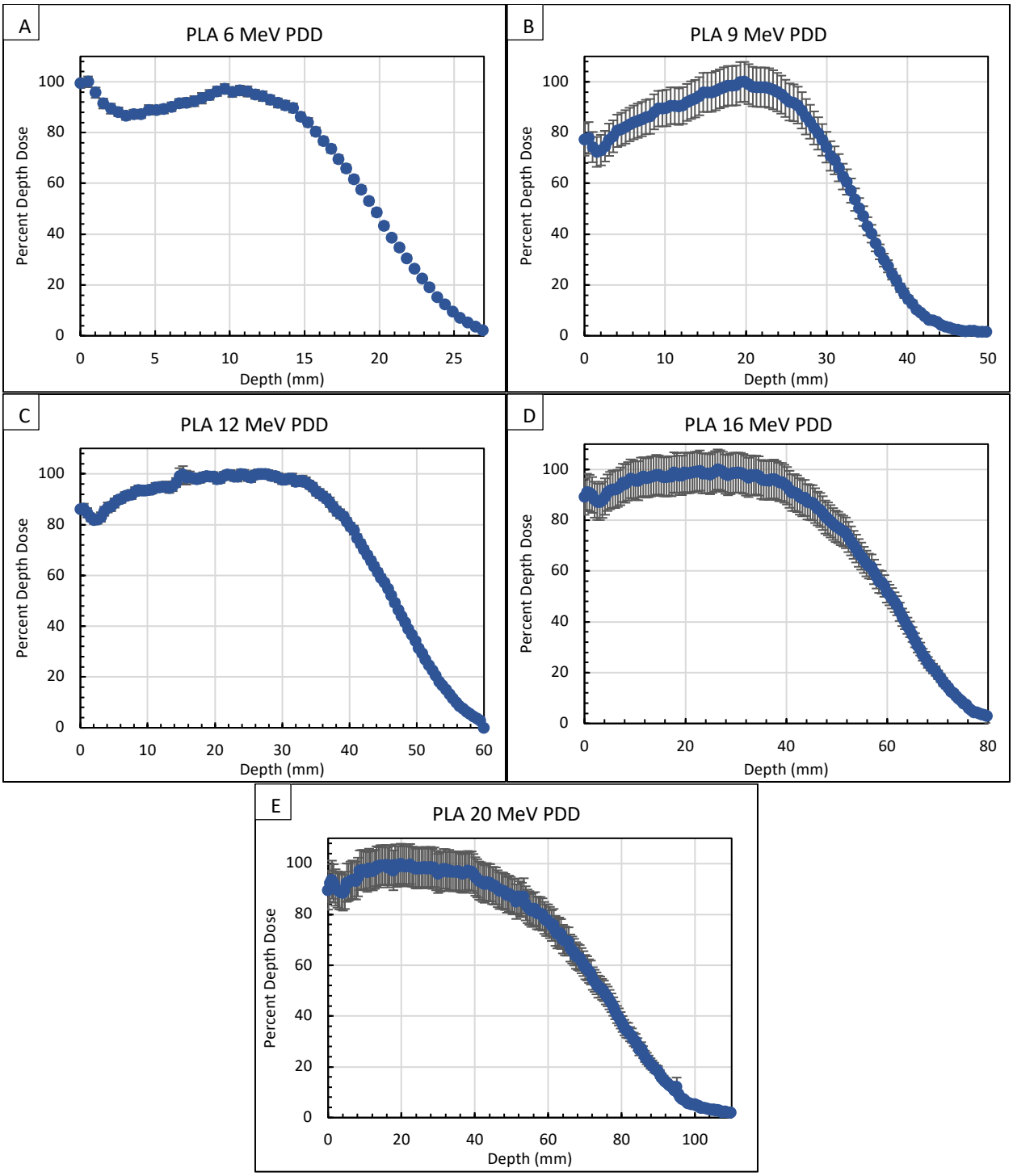

Figure 5.7: PDD curves for PLA for (A) 6 MeV, (B) 9 MeV, (C) 12 MeV, (D) 16 MeV, and (E) 20 MeV.

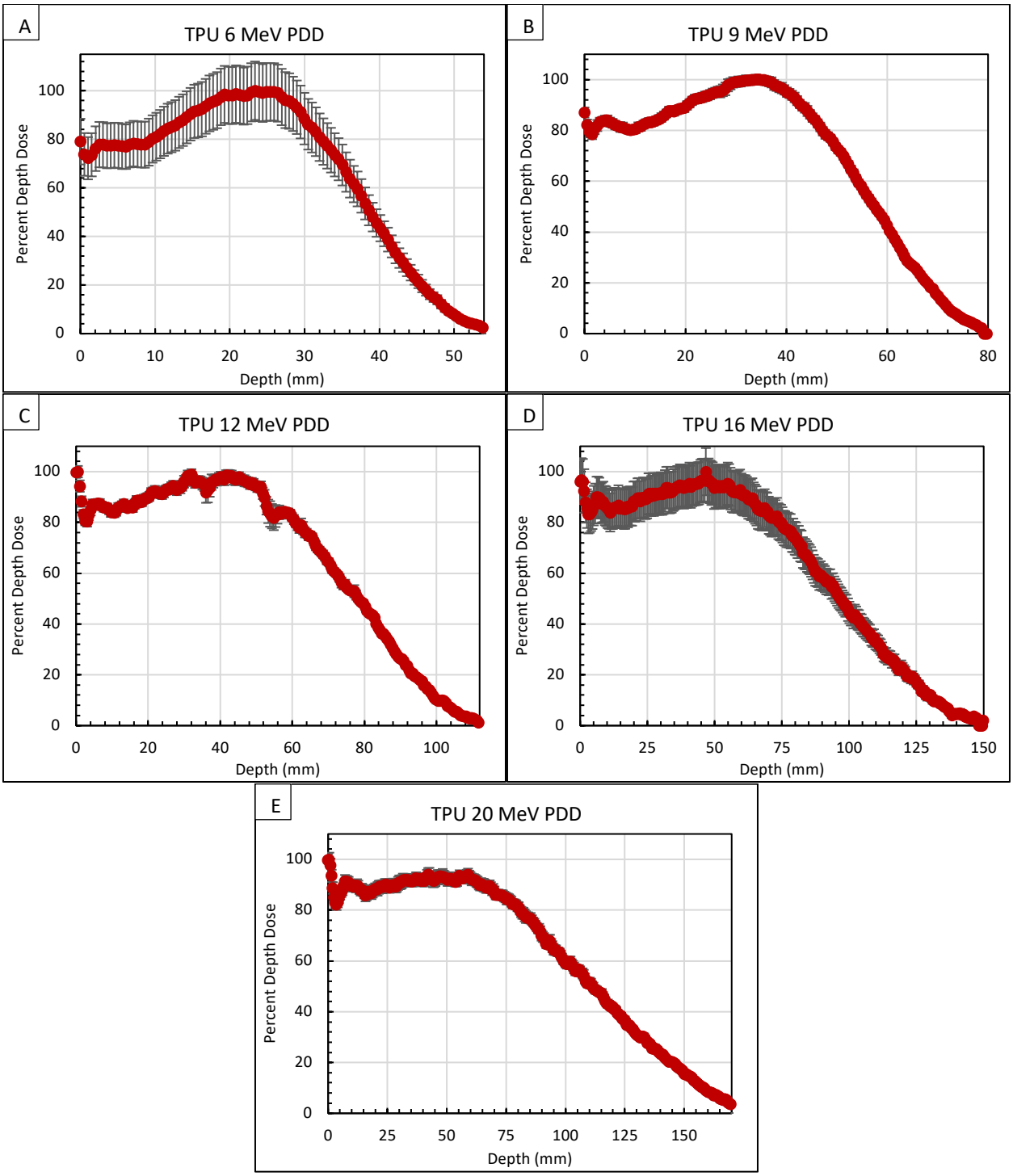

Figure 5.8: PDD curves for TPU for (A) 6 MeV, (B) 9 MeV, (C) 12 MeV, (D) 16 MeV, and (E) 20 MeV.

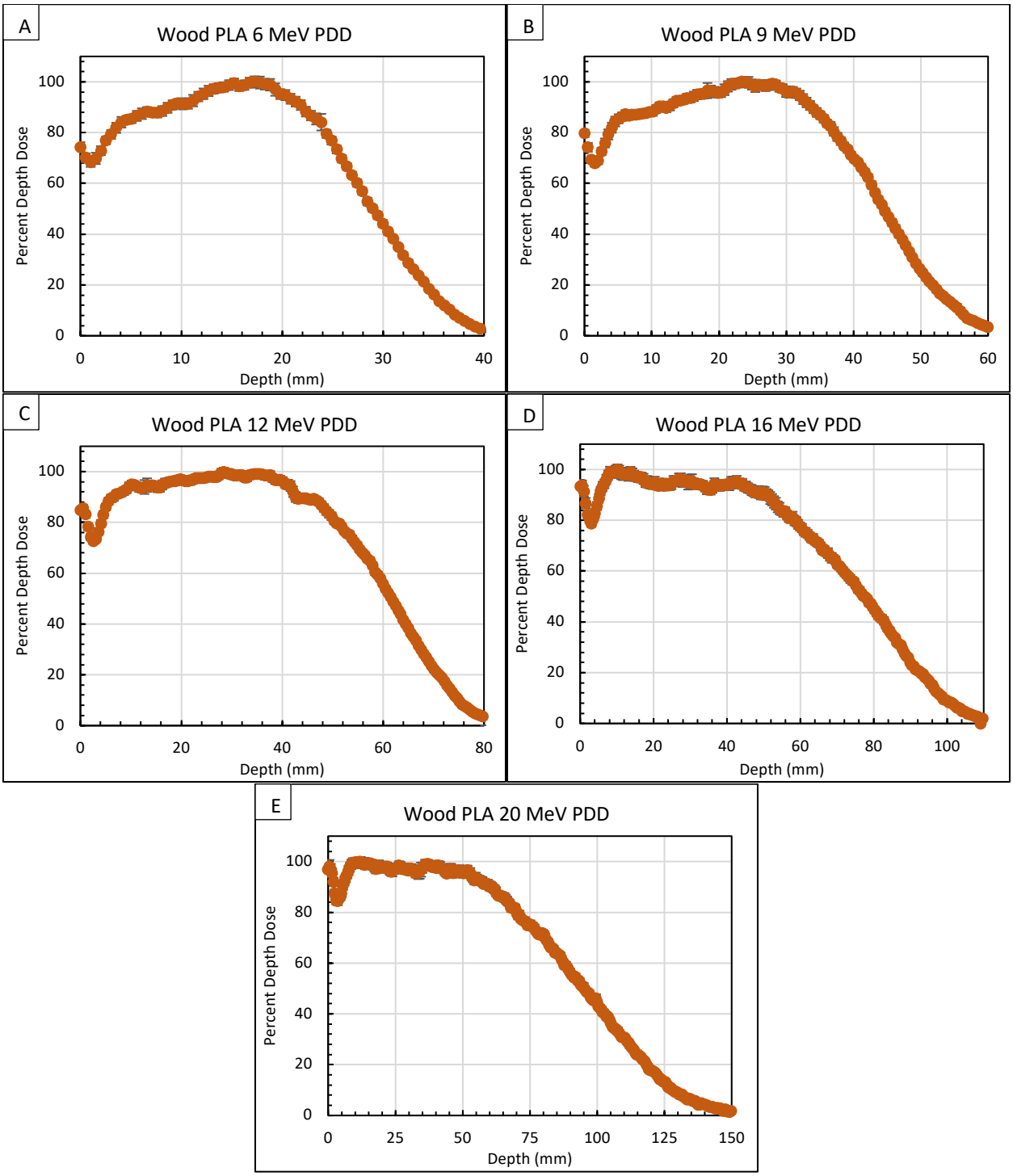

Figure 5.9: PDD curves for Wood PLA for (A) 6 MeV, (B) 9 MeV, (C) 12 MeV, (D) 16 MeV, and (E) 20 MeV.

The general trend of the PDD curves show the data start around 60 to 80 percent depth dose, increase to a maximum, then decrease to zero dose. All of the materials' PDD curves except Iron PLA have a dip in the PDD curve within the first 5 mm of depth.

This is likely due to the film edge not being perfectly aligned with the edge of the blocks, causing the film artifact (Figure 5.10, A). The alignment of the film is especially important when using the geometry in which the film is parallel with the beam axis [30]. This is the geometry that was used when irradiating the film. This type of artifact can potentially be alleviated by tilting the gantry to a small degree [60]. The Iron PLA exhibits a horn which gets more prominent with higher energy (Figure 5.6). The other printed materials also show some form of a horn, although less prominent than the Iron PLA, for many of the energies (Figure 5.4; Figure 5.5 D, E; Figure 5.8 B, C, E; Figure 5.9 D, E). This is likely due to air gaps as demonstrated by Figure 5.10, B. However, in the Iron PLA, due to the material containing embedded pieces of high-Z iron, the horn could also be caused by increased surface scatter.

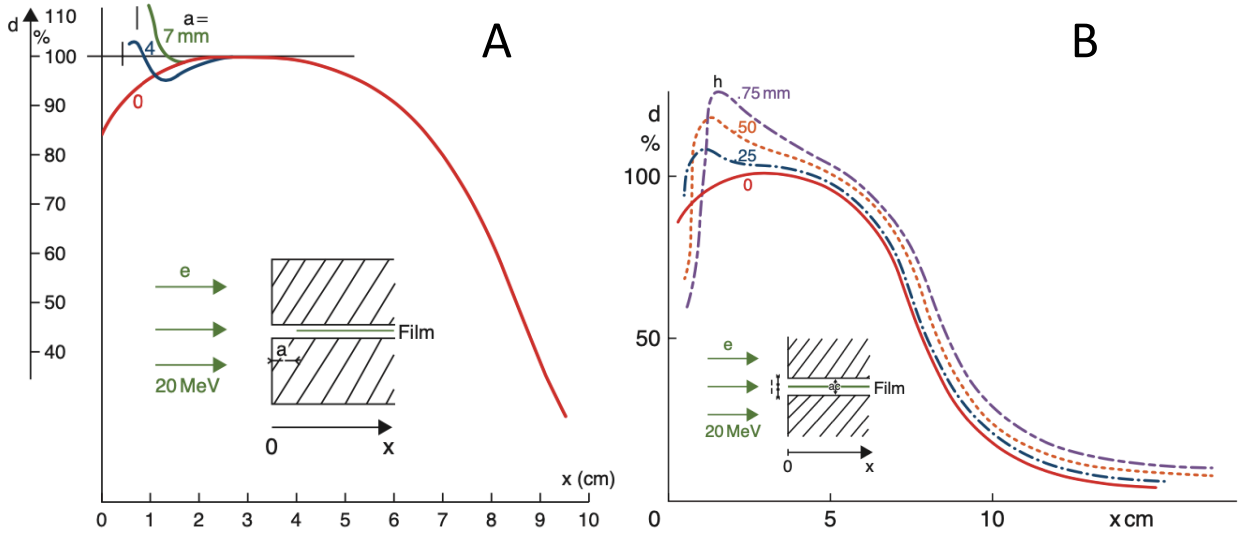

Figure 5.10: (A) Film artifact due to misalignment of film with the phantom (B) Film artifact due to air gap (Republished with permission of A. Dutreix and J. Dutreix, from Film Dosimetry of High-Energy Electrons, Annals of the New York Academy of Science, 2006, permission conveyed through John Wiley and Sons [30].

The PDD curves of the 3D printed materials can be directly compared to the Plastic Water (PW) PDD curve, as the measurements were all made using the same geometric setup (Figures 5.11 to 5.15). This is useful when implementing the materials into patient

treatment plans, as the PDD of the material exhibits the electron's response within the material. This ultimately determines the dose to the surface of the patient when being used in patient treatment, due to the material's attenuation of the radiation with respect to depth, prior to reaching the patient. Depending on how the dose distribution needs to be altered, different materials could be used to attenuate the photon beam and shift the dose in a desired fashion.

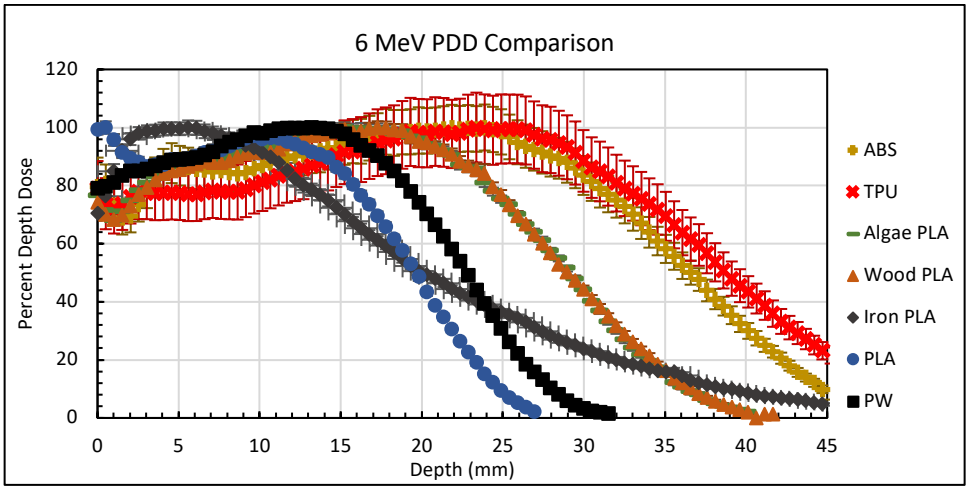

Figure 5.11: PDD curve comparison between materials for 6 MeV electron beam.

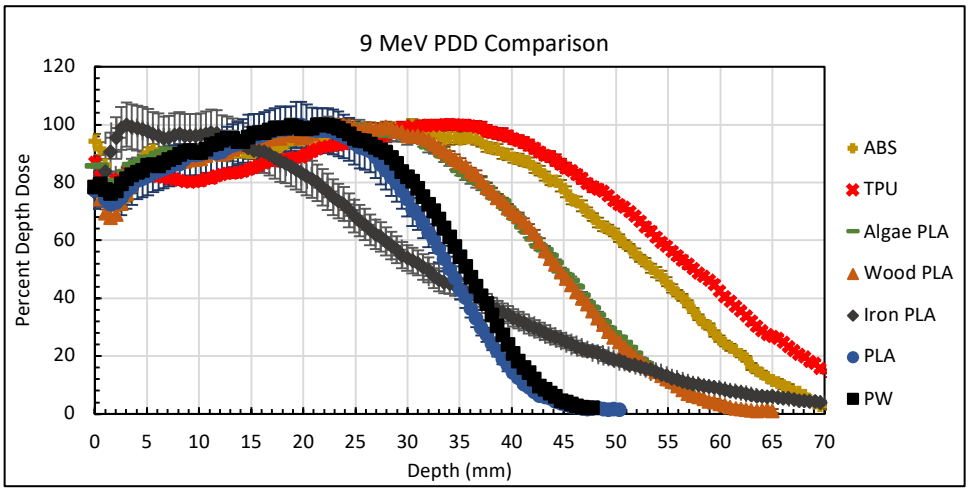

Figure 5.12: PDD curve comparison between materials for 9 MeV electron beam.

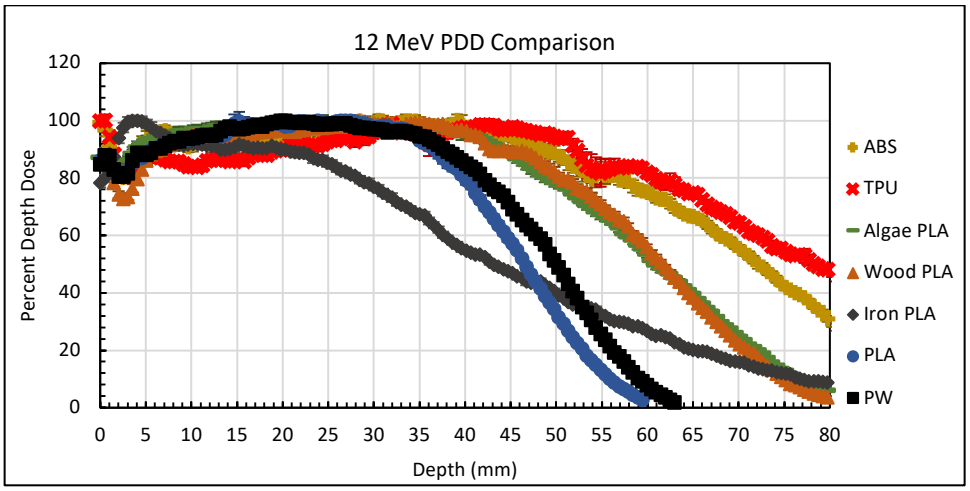

Figure 5.13: PDD curve comparison between materials for 12 MeV electron beam.

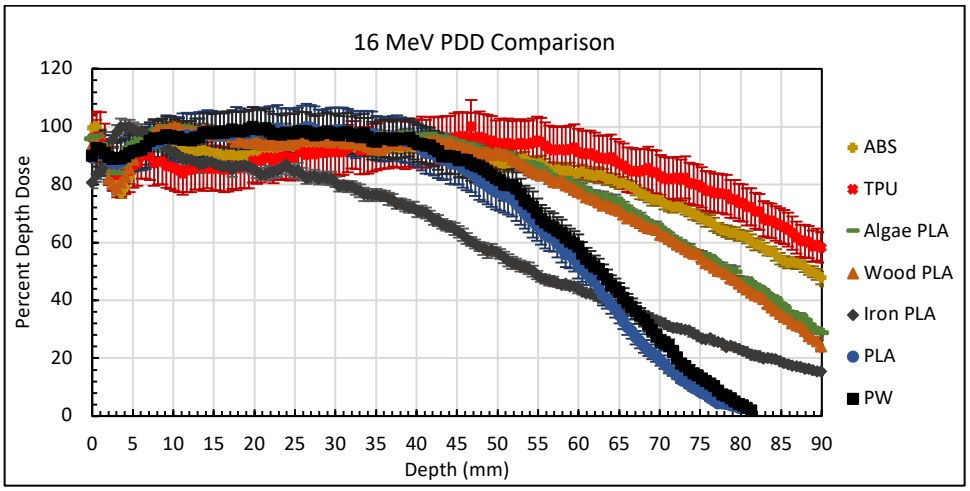

Figure 5.14: PDD curve comparison between materials for 16 MeV electron beam.

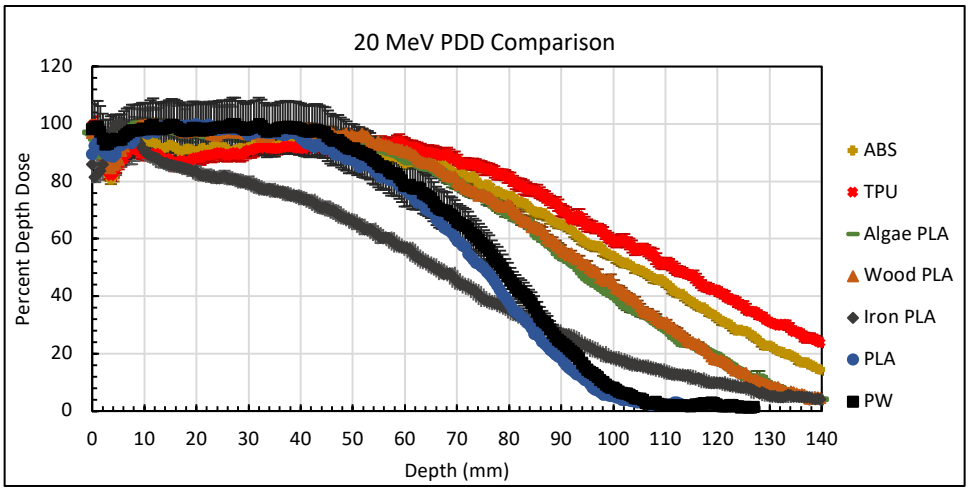

Figure 5.15: PDD curve comparison between materials for 6 MeV electron beam.

Photon

The TMR values for each material were calculated from the raw charge measurements using Equation 3.29, shown in Figures 5.16 to 5.22. Figure 5.16 shows the TMR for the Plastic Water (PW) graphed against the clinical TMR data gathered at the Stephenson Oklahoma Cancer Center (SOCC) during the commissioning of the linear accelerator. Figures 5.17 to 5.22 are graphed with the PW TMR curve for comparison.

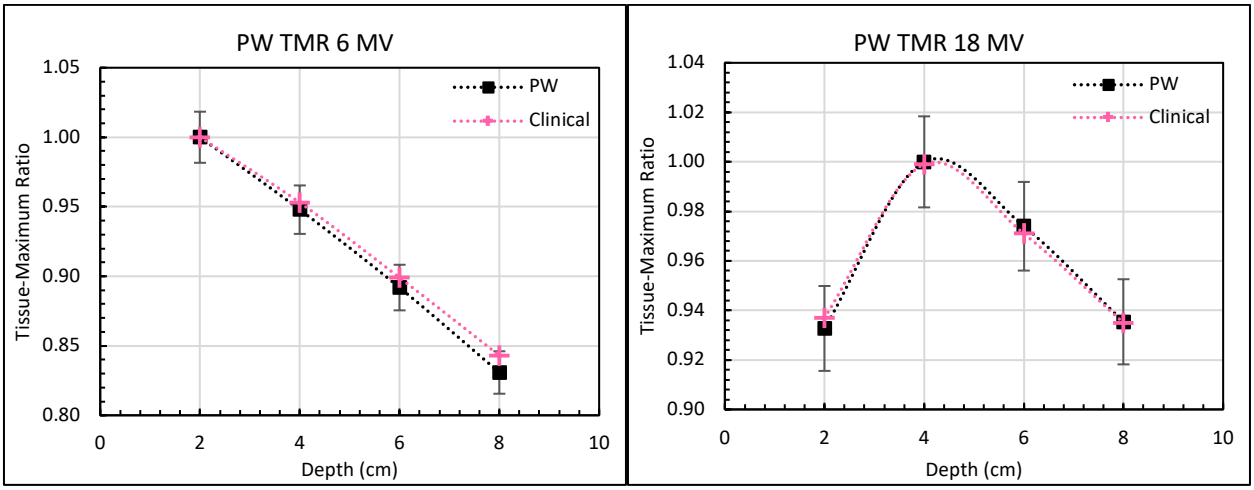

Figure 5.16: TMR curves for Plastic Water for (A) 6 MV and (B) 18 MV, graphed with the SOCC clinical TMR data.

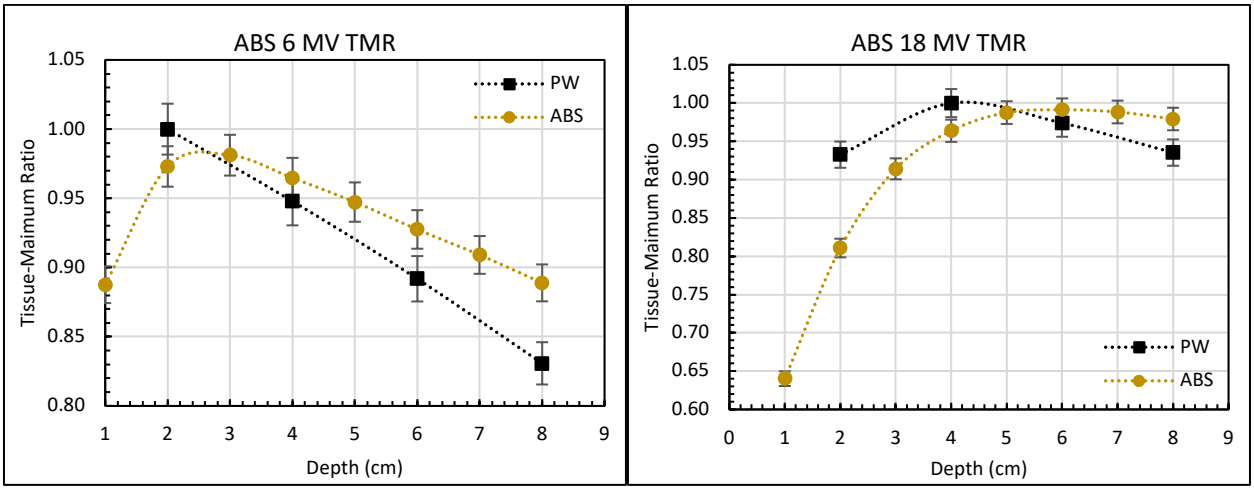

Figure 5.17: TMR curves for ABS for (A) 6 MV and (B) 18 MV.

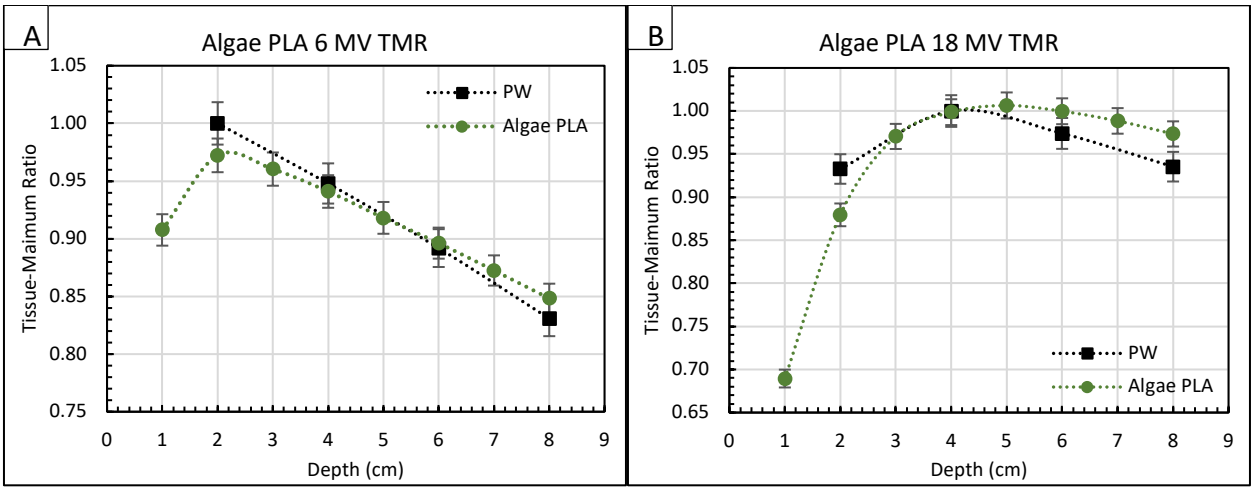

Figure 5.18: TMR curves for Algae PLA for (A) 6 MV and (B) 18 MV.

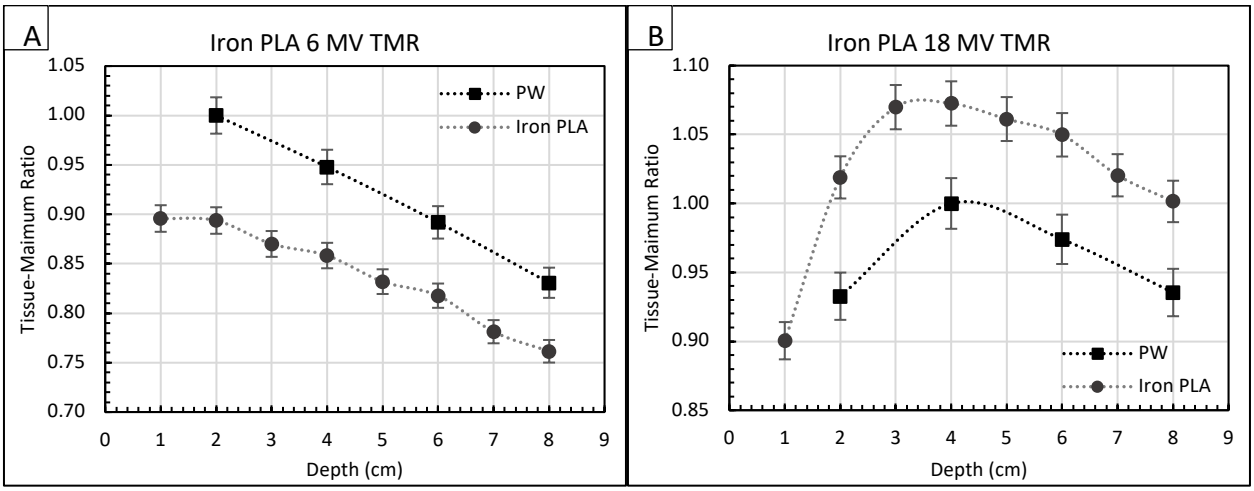

Figure 5.19: TMR curves for Iron PLA for (A) 6 MV and (B) 18 MV.

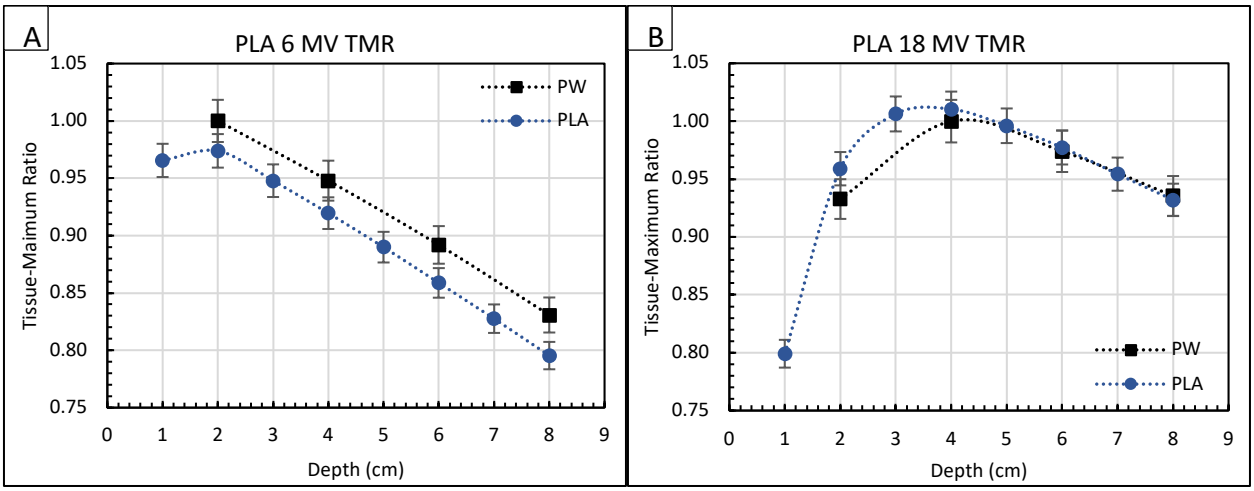

Figure 5.20: TMR curves for PLA for (A) 6 MV and (B) 18 MV.

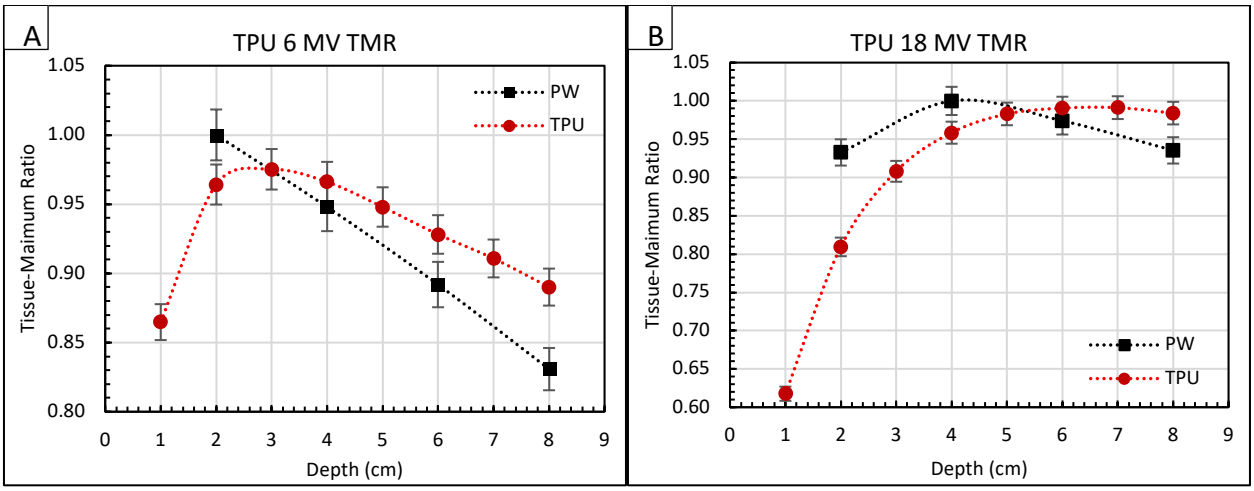

Figure 5.21: TMR curves for TPU for (A) 6 MV and (B) 18 MV.

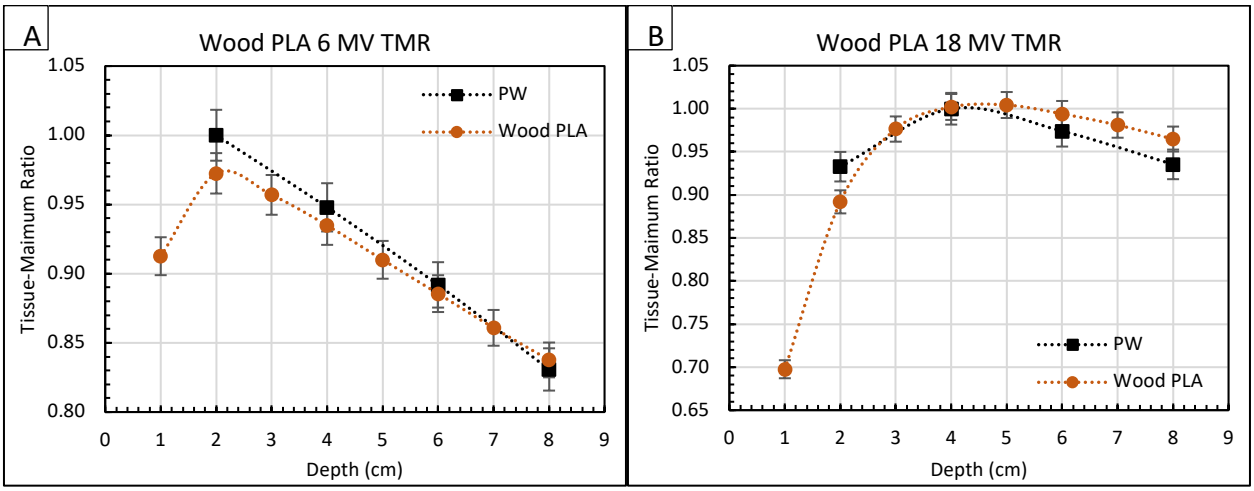

Figure 5.22: TMR curve for Wood PLA for (A) 6 MV and (B) 18 MV.

The TMR curves for all materials have the same trend of increasing to a maximum, then decreasing. Wood PLA and Algae PLA for 6 MV, and PLA for 18 MV follow the Plastic Water (PW) data the closest, with all points the same as PW (within the known uncertainty). Iron PLA exhibits the largest deviation from the PW points. The PW TMR points show good agreement with the clinical TMR data, indicating that comparing the 3D printed materials to the PW material is, for all practical purposes, equivalent to comparing the 3D printed material response to the measurements made in the water tank during commissioning. As in the case of the electron PDD curves, seeing the response of the

3D printed materials relative to the PW TMR curves allows for the response of the materials to be known, and better implemented into clinical treatment planning.

Figure 5.23 shows the percent difference of each material compared with Plastic Water (PW) for the 6 MV and 18 MV energies.

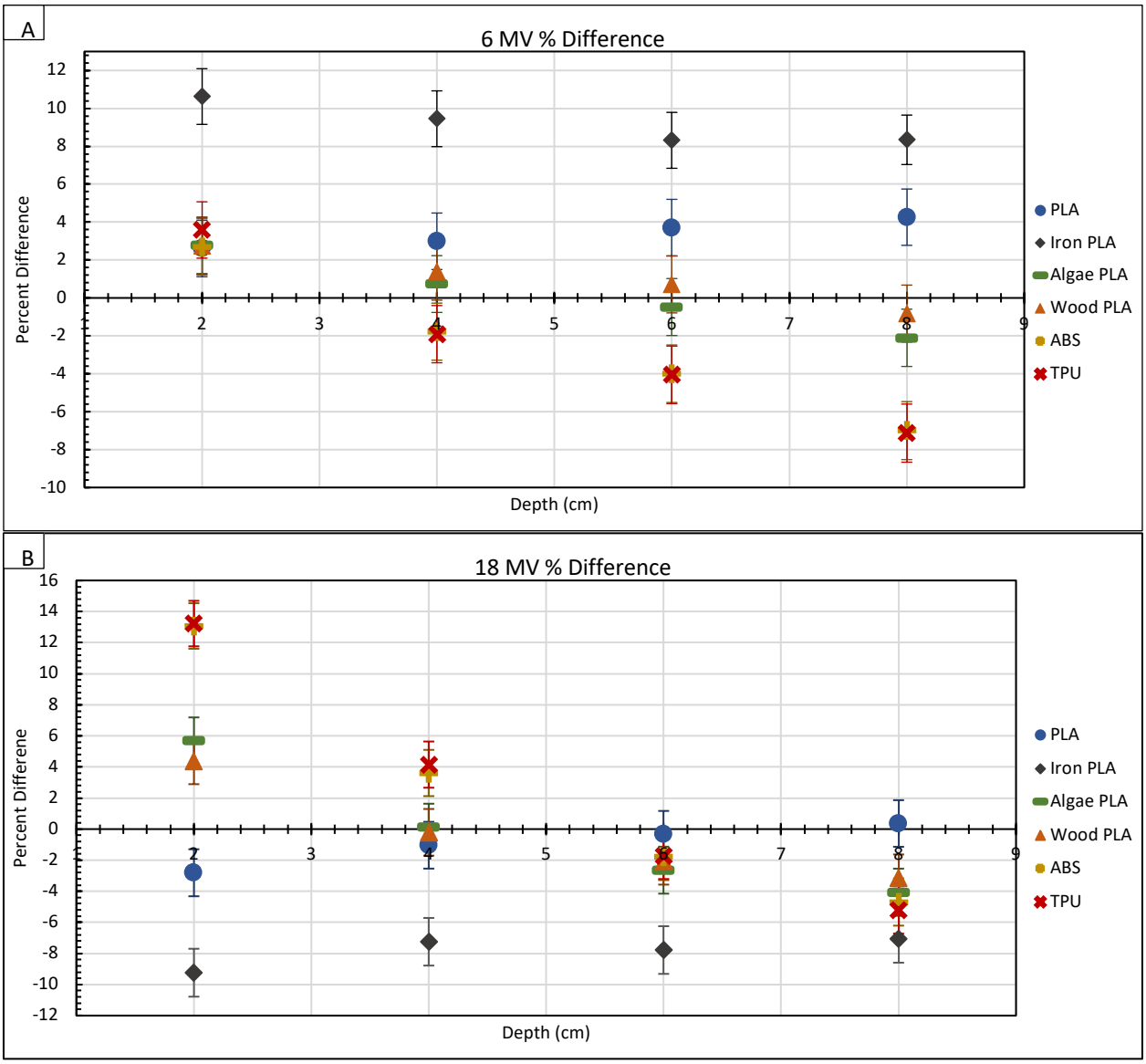

Figure 5.23: The percent difference of each material from plastic water for (A) 6 MV and (B) 18 MV.

The materials with densities lower than the PW blocks exhibit a negative trend in the percent difference with increasing depth, whereas the PLA, with a density higher than

the PW blocks exhibits a positive trend. The increases in percent difference values between the two energies at each depth for TPU, ABS, Algae PLA, and Wood PLA are a result of the larger offset in the depth of maximum dose compared with PW at higher energies as a function of density of the materials. The Iron PLA percent difference values exhibit a large change at each depth between energies. This is likely due to the increase in scatter at 18 MV producing a larger charge value at each depth relative to PW.

When directly comparing the dose measured in the materials, no material, for either energy, should be considered to exhibit the same behavior as PW. Within a 5% dose difference, however, Wood PLA and PLA would be considered comparable. For all materials but Iron PLA, each material is equal to the PW measurement (e.g. percent difference is zero) at a specific depth. If the thickness of the 3D printed material were to be equal to the depth value at which the percent difference is zero, then the material could be assumed to be water in the TPS, and no alterations would need to made in the TPS for the material.

Proton

The RSP analysis was performed using Equation 3.37 and the associated uncertainty analysis using Equation 3.44. Table 5.1 reports the RSP values for each material at each energy.

Table 5.1: RSP values for each material.

	RSP		
Material	**70.77 MeV**	**120.21 MeV**	**180.15 MeV**
ABS	0.667 ± 0.208	0.736 ± 0.228	0.737 ± 0.229
Algae PLA	0.672 ± 0.204	0.730 ± 0.218	0.729 ±0.218
Iron PLA	1.21 ± 0.376	1.30 ± 0.401	1.33 ± 0.410
PLA	1.04 ± 0.202	1.11 ± 0.213	1.10 ± 0.213
TPU	0.555 ± 0.0626	0.609 ± 0.0661	0.615 ± 0.0684
Wood PLA	0.706 ± 0.114	0.753 ± 0.117	0.744 ± 0.128

The RSP values reflect the range shift the materials would subsequently cause in water. The RSP values range between 0.555 and 1.33. For each material, the RSP for 70.77 MeV are smaller than from the 120.21 MeV and 180.15 MeV values. This could be due to the air cavities in the printed materials. With an increase in energy, the air cavities could play a larger role in the increase in range compared with the smaller energy RSP values. However, within the uncertainty, the values show no energy dependence for the energy range in which the measurements were made. For all energies, the thickness of the material block used in the beam path affects the RSP values. Ideally, a material block of minimal thickness would be used to reduce additional multiple coulombic scatter contributing to the R_{90} measurements [61]. An averaging affect also occurs because of this, and the probable air cavities within the material compound this issue. The RSP values are critical for treatment planning, because implementing the corresponding RSP value for the material being used is the only way correct treatment plans can be created. These values are incorporated into treatment plans via a RSP-to-HU conversion [33]. The RSP values given in Table 3.1 allow for these materials to be used in proton treatment. It should be noted, however, according to Zou et al. (2015), that 3D printed materials using

FDM may not be ideal for proton therapy due to inhomogeneities causing undesirable dose effects [13].

Density

The density of each block was analyzed by Equation 3.41, and these were averaged using Equation 3.42 to obtain the values shown in Figure 5.24. The average density value for the given material is the thicker red line, and the thinner red lines are the average uncertainty bands, determined by Equation 3.51, given by 1σ on the graph. The average value is labelled above or below and to the left of the red line representing the average.

The average material densities range from 0.7069 to 1.232 g/cm^3. The largest spread between blocks of one material was for the Iron PLA, with the least dense block being 0.6955 g/cm^3 and the densest block being 1.563 g/cm^3. As mentioned previously, the two of the blocks were printed from one spool, and two were printed from another. According to Craft et al. (2018), differences in spools can account for large variations in printed density [42]. Iron PLA is also an embedded material. It is possible that one spool of material contained a higher amount of iron than another.

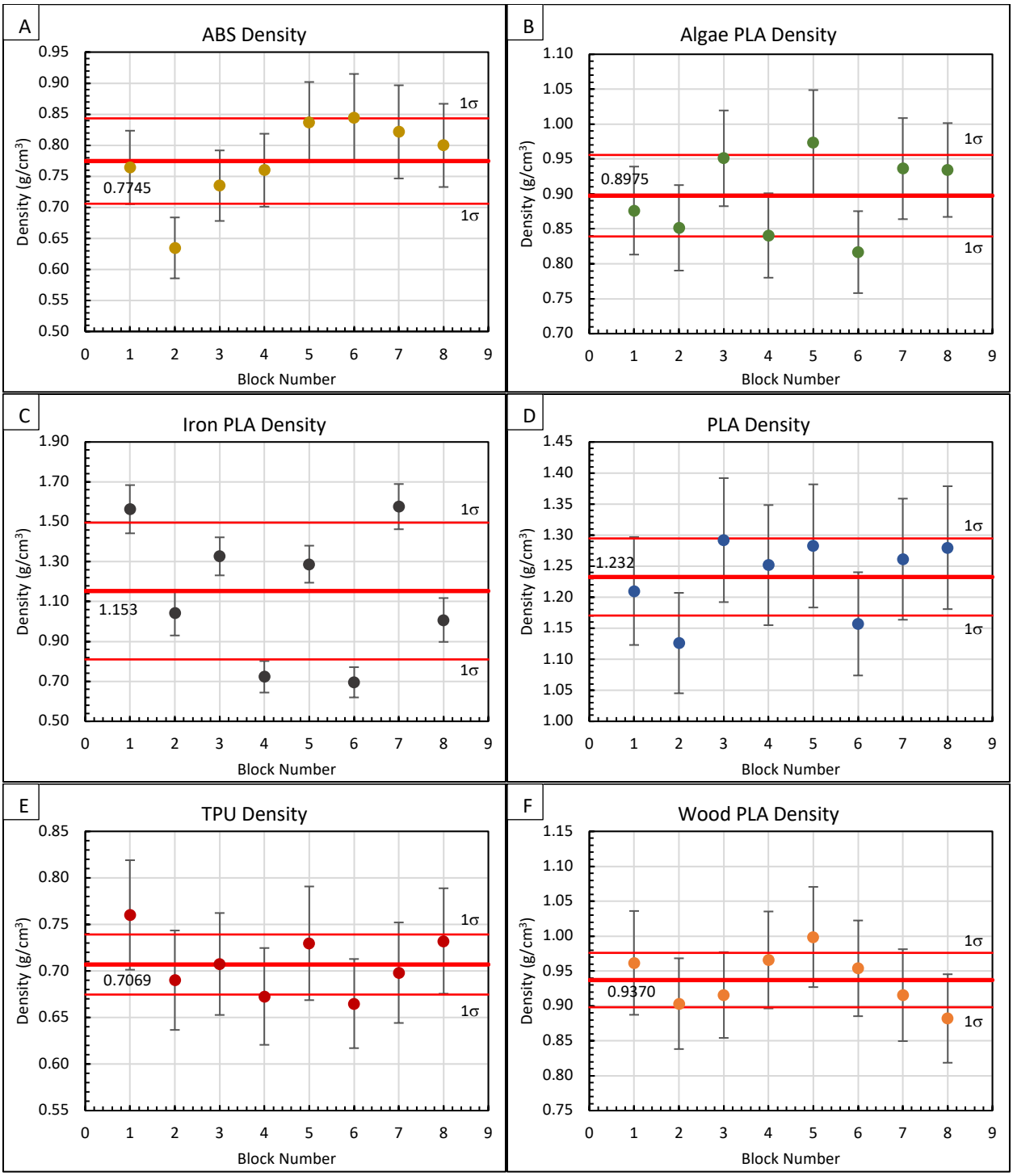

Figure 5.24: The density values of the individual blocks and the average values of the materials for (A) ABS, (B) Algae PLA, (C) Iron PLA, (D) PLA, (E) TPU, and (F) Wood PLA.

Density Comparison

The density of the 3D printed material is the most important characteristic when implementing the material into the TPS to be used in patient treatment, according to Craft et. al (2018) [42]. Figure 5.25 shows the average densities of PLA and ABS compared with the percent infill results from those published [45, 62]. It was assumed when plotting the measured data points that the blocks' percent infill was 100%, as indicated by the print settings used to print the materials.

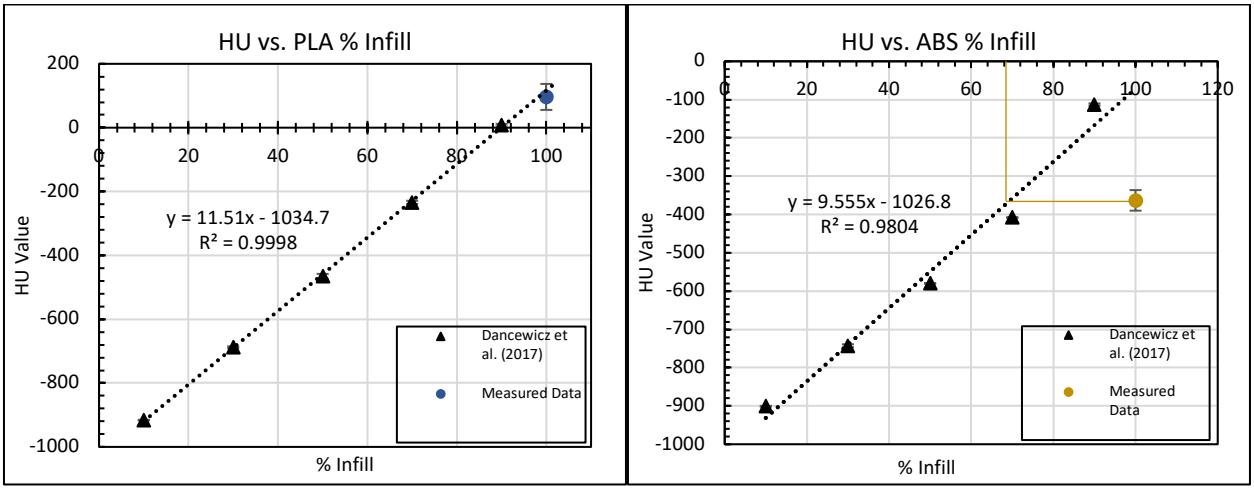

Figure 5.25: Percent infill of (A) PLA and (B) ABS compared to published HU values.

Compared with the results from Dancewicz et al. (2017), the printed PLA block point follows the linear trend of the data. Figure 5.25 indicates the PLA blocks were printed at, or close to 100% infill. The result of comparing the ABS measured data to Dancewicz et al. (2017) suggests that the ABS blocks were printed at a much lower percent infill than indicated by the print settings. Following the linear trend of the published data points suggests that the density of the ABS printed blocks is closer to 70% infill. Lindsay et al. (2015) found similar results, in which the printed ABS density was approximately 13% lower than the density of the spool of material when printed using the 100% infill setting [38].

Figure 5.26 compares the average density of the materials with the average HU value of the materials. The results in Figure 5.26 show an approximately linear trend between HU value and density. Due to the large variation in the Iron PLA density values between blocks, the larger density values within the uncertainty bars follow the linear trend more closely. However, it should be noted that although 3D printed materials' HU values exhibit a linear relationship, results from Craft et al. (2018) illustrate that the linear trend of the 3D printed materials is offset from the traditional human tissue CT calibration curve [42].

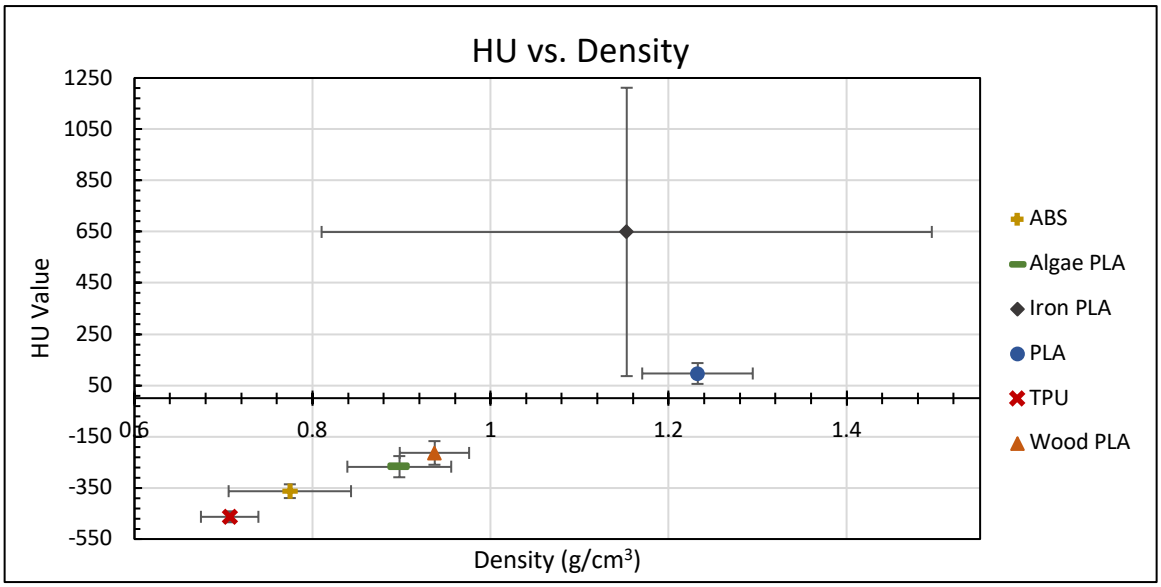

Figure 5.26: Density versus HU for each material.

Figure 5.27 compares the R_{50} of the electron PDD curves to the density of the materials. The R_{50} is a measurement used in the calibration of electron beams via TG-51, and so many clinics that utilize TG-51 [63] measure the R_{50} in water. An R_{50} comparison can characterize how the dose changes with depth at a reference point between materials. The relationship exhibits a negative linear trend, in which the R_{50} decreases with increasing density for all energies. This relationship is to be expected

because higher density materials attenuate more particles at shallower depths, causing the dose fall off to occur earlier, giving smaller R_{50} values.

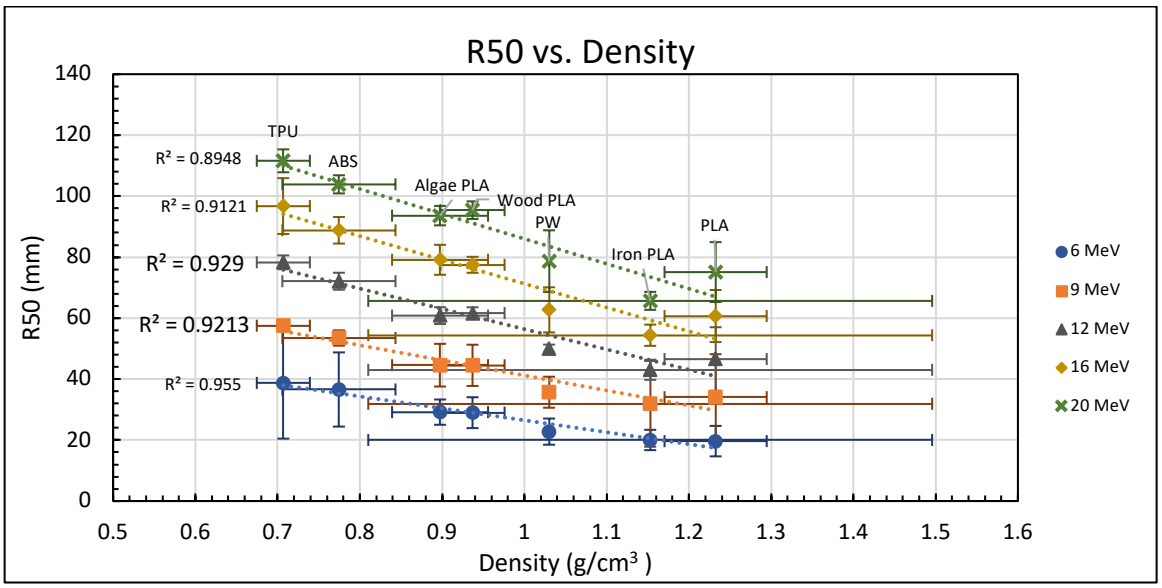

Figure 5.27: A comparison of the R_{50} values from the electron PDD and the material densities.

Figure 5.28 compares the RSP values calculated from the proton measurements to the densities of the materials. The results show a positive linear trend between materials. Within a given material, the RSP proves to have no energy dependence. The results agree with Moyers et al. (2010) for which the trend is also approximately linear within the density values represented here [33].

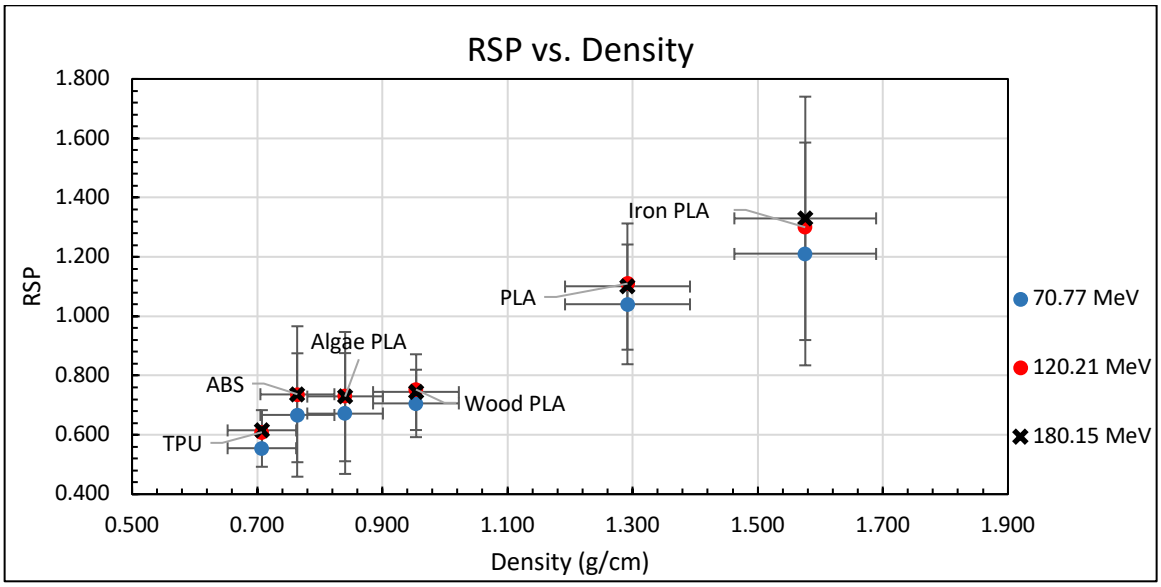

Figure 5.28: Comparison of the RSP values from the proton measurements and material densities.

Limitations of 3D Printing

3D printing has established itself a place within the medical physics community; however, there are limiting factors that need to be considered before implementation of 3D printed objects into patient treatment. Although 3D printing can be implemented into the workflow of the clinic, unforeseen complications can occur if the print file has an error or if printing occurs unsupervised. Quality assurance processes are strongly recommended to ensure that clinically acceptable print quality is routinely available and patient treatment delays can be prevented.

The effective density of the printed objects using the same material can vary widely, even when using the same print settings. This is apparent for Iron PLA, in which the density differences were apparent even by crude 'in-hand' comparisons. Not only does the density difference imply internal air cavities, but the differences in printing can also cause the printed infill layers to fuse poorly with the edges/borders defining print volume. Warping and shrinking can also occur, as seen in the ABS blocks. These issues

have the potential to cause large errors in the dose distribution if used in patient treatments without secondary volumetric simulation.

Due to the variation in density and HU value between and within blocks, characterizing a particular material based on its physical and radiological properties cannot be reliably generalized in a useful fashion. Each printed object used in patient treatment should be characterized individually, potentially decreasing efficiency and adding time and labor to workflows that may become unfeasible without healthy investments in specific 3D printing infrastructures.

Recommendations on Implementing 3D Printing into the Clinic

Due to its potential limitations, the recommendations for implementing 3D printing into the clinic are provided for consideration. Research should be done into the type of 3D printer which would most benefit the clinic. FDM printers are generally the most cost effective type of printer to implement, also demonstrating a reasonable learning curve, but SLS, SLM, and SLA have a higher printing resolution and material consistency [4]. An area should be designated for the printer to be placed, and if possible, a shield should be placed around the printer to reduce potential warping or shrinking. The ventilation (or filtration) of the room should be taken into consideration as the printing process can produce airborne micro-plastics and chemical outgassing.

Quality assurance procedures should be put in place by those who will be implementing the 3D printed objects into the patient treatment. Due to the density and HU value variations discussed above, each individual printed object should undergo verification testing before use [42]. The dimensions of the objects may be measured to verify geometric accuracy, especially if in direct patient contact or within the therapeutic

beam path. Ideally, prints should be CT scanned while on the patient, determining HU value as well as verifying placement during treatment. Although HU value is often used, ideally the density of the material should also be determined for implementation into the treatment planning system. According to Craft et. al. (2018), HU values of 3D printed materials do not adhere to the typical HU to density trend [42], and implementing the density of the printed material will provide more accurate treatment plans and dose distributions. Once verified, printed objects should be safe to use throughout the patient treatment.

CHAPTER VI

SUMMARY

The uses of 3D printing are rapidly expanding to include applications in radiation oncology. Patient-specific boluses, brachytherapy applicators, and immobilization devices have been 3D printed and used in patient treatments [8, 10, 11, 17, 19] for a wide variety of treatment modalities. Phantoms modeling patient anatomy have been built from 3D printed parts to be used in imaging and dosimetric studies. As 3D printing becomes more commonplace in the realm of radiation treatment, the printed materials being used should be characterized to adequately implement 3D printing successfully in the clinic.

The goal of this project was to 3D print clinically relevant materials in order to characterize them using various methods. ABS, Algae PLA, Iron PLA, PLA, TPU, and Wood PLA were printed in blocks such that the geometric setup matched that of available plastic water equivalent blocks. This was to provide relevant results when compared with established water standard. The 3D printed blocks were measured under electron beam, photon beam, proton beam, and CT imaging system. These were all performed using clinically established energies typical of patient treatment. From the measurements made, the average HU value of each material was determined, electron PDD curves were generated, photon TMR curves were compared with those of water, proton RSP values were calculated, and the density was determined for each material.

The measured HU values for each material varied widely, making it unreliable for each material to be defined by a single, averaged value. The electron PDD results provided depth dose curves characteristic of the material. Iron PLA exhibited a large horn

in the PDDs for all energies and the other materials all exhibited a dip in the dose to some extend at a very shallow depth. The TMR and percent difference plots aided in illustrating how the materials compared with the PW values. Wood PLA and PLA proved to have the most similar values compared with the PW values. This data also demonstrated how the PW values were equivalent to the commissioning TMR values within the given uncertainty. RSP values aid in implementing material characteristics into treatment plans to provide correct dose distributions. The RSP values were shown to have no energy dependence within the given uncertainty, and so these values can be used for treatment plans of all proton energies.

The PDD, TMR, and RSP results, as well as the average HU values, provide a clinical reference for dose distribution compared with water for implementation in clinical settings. Each of these results were affected by the density of the materials. The density of the material is the most influential characteristic and may vary substantially between prints of the same material. Directly determining the density and HU value of each 3D printed object to be used in a clinical setting should be performed after printing and before implementation into patient treatment.

Although 3D printing has much promise for use in radiation oncology, it is important to note that establishing a solid quality assurance protocol prior to its implementation is key to an accurate and successful clinical application. It is recommended that each 3D printed object be properly characterized before clinical use. Through the implementation of these measures, 3D printing in the clinical setting has the potential to further improve patient care within radiation oncology departments.

LIST OF REFERENCES

1. Bibb, R., D. Thompson, and J. Winder, *Computed tomography characterisation of additive manufacturing materials.* Medical Engineering & Physics, 2011. **33**(5): p. 590-596.

2. Sharma, S. and S. Goel, *3D Printing and its Future in Medical World*. 2019: Journal of Medical Research and Innovation. p. e000141.

3. *3-D Printing Steps into the Spotlight.* Upstate Business Journal, 2013.

4. Chen, X.B., et al., *Recent Progress on 3D-Printed Polylactic Acid and Its Applications in Bone Repair.* Advanced Engineering Materials: p. 19.

5. Ehler, E., D. Craft, and Y. Rong, *3D printing technology will eventually eliminate the need of purchasing commercial phantoms for clinical medical physics QA procedures.* Journal of Applied Clinical Medical Physics, 2018. **19**(4): p. 8-12.

6. Burnard, J.L., et al., *3D-printed spine surgery implants: a systematic review of the efficacy and clinical safety profile of patient-specific and off-the-shelf devices.* European Spine Journal: p. 13.

7. Giannatsis, J. and V. Dedoussis, *Additive fabrication technologies applied to medicine and health care: a review.* International Journal of Advanced Manufacturing Technology, 2009. **40**(1-2): p. 116-127.

8. Canters, R.A., et al., *Clinical implementation of 3D printing in the construction of patient specific bolus for electron beam radiotherapy for non-melanoma skin cancer.* Radiotherapy and Oncology, 2016. **121**(1): p. 148-153.

9. Kong, Y.H., et al., *A dosimetric study on the use of 3D-printed customized boluses in photon therapy: A hydrogel and silica gel study.* Journal of Applied Clinical Medical Physics, 2019. **20**(1): p. 348-355.

10. Lukowiak, M., et al., *Utilization of a 3D printer to fabricate boluses used for electron therapy of skin lesions of the eye canthi.* Journal of Applied Clinical Medical Physics, 2017. **18**(1): p. 76-81.

11. Zhao, Y.Z., et al., *Clinical applications of 3-dimensional printing in radiation therapy.* Medical Dosimetry, 2017. **42**(2): p. 150-155.

12. Fujimoto, K., et al., *Efficacy of patient-specific bolus created using three-dimensional printing technique in photon radiotherapy.* Physica Medica-European Journal of Medical Physics, 2017. **38**: p. 1-9.

13. Zou, W., et al., *Potential of 3D printing technologies for fabrication of electron bolus and proton compensators.* Journal of Applied Clinical Medical Physics, 2015. **16**(3): p. 90-98.

14. Kitamori, H., et al., *Evaluation of mouthpiece fixation devices for head and neck radiotherapy patients fabricated in PolyJet photopolymer by a 3D printer.* Physica Medica-European Journal of Medical Physics, 2019. **58**: p. 90-98.

15. Michiels, S., et al., *Towards 3D printed multifunctional immobilization for proton therapy: Initial materials characterization.* Medical Physics, 2016. **43**(10): p. 5392-5402.

16. Zarghami, N., et al., *Technical Note: Immunohistochemical evaluation of mouse brain irradiation targeting accuracy with 3D-printed immobilization device.* Medical Physics, 2015. **42**(11): p. 6507-6513.

17. Cunha, J.A.M., et al., *Evaluation of PC-ISO for customized, 3D printed, gynecologic Ir-192 HDR brachytherapy applicators.* Journal of Applied Clinical Medical Physics, 2015. **16**(1): p. 246-253.

18. Lee, J.H., et al., *Three-dimensional-printed vaginal applicators for electronic brachytherapy of endometrial cancers.* Medical Physics, 2019. **46**(2): p. 448-455.

19. Sethi, R., et al., *Clinical applications of custom-made vaginal cylinders constructed using three-dimensional printing technology.* Journal of Contemporary Brachytherapy, 2016. **8**(3): p. 210-216.

20. Bieniosek, M.F., B.J. Lee, and C.S. Levin, *Technical Note: Characterization of custom 3D printed multiodality imaging phantoms.* Medical Physics, 2015. **42**(10): p. 5913-5918.

21. Filippou, V. and C. Tsoumpas, *Recent advances on the development of phantoms using 3D printing for imaging with CT, MRI, PET, SPECT, and ultrasound.* Medical Physics, 2018. **45**(9): p. E740-E760.

22. Hazelaar, C., et al., *Using 3D printing techniques to create an anthropomorphic thorax phantom for medical imaging purposes.* Medical Physics, 2018. **45**(1): p. 92-100.

23. Hernandez-Giron, I., et al., *Development of a 3D printed anthropomorphic lung phantom for image quality assessment in CT.* Physica Medica-European Journal of Medical Physics, 2019. **57**: p. 47-57.

24. Kamomae, T., et al., *Three-dimensional printer-generated patient-specific phantom for artificial in vivo dosimetry in radiotherapy quality assurance.* Physica Medica-European Journal of Medical Physics, 2017. **44**: p. 205-211.

25. Lee, M., et al., *Comparing phase- and amplitude-gated volumetric modulated arc therapy for stereotactic body radiation therapy using 3D printed lung phantom.* Journal of Applied Clinical Medical Physics, 2019. **20**(2): p. 107-113.

26. Wu, C., et al., *Technical note: A 3D-printed phantom for routine accuracy check of Gamma Knife Icon HDMM system.* Journal of Applied Clinical Medical Physics, 2018. **19**(4): p. 299-301.

27. Craft, D.F. and R.M. Howell, *Preparation and fabrication of a full-scale, sagittal-sliced, 3D-printed, patient-specific radiotherapy phantom.* Journal of Applied Clinical Medical Physics, 2017. **18**(5): p. 285-292.

28. Khan, F., J. Gibbons, and P. Sperduto, *Treatment Planning in Radiation Oncology*. 4th ed. 2016, Philadelphia, PA: Lippincott Williams &Wilkins. 662.

29. *Plastic Water Phantom Materials. Team Best. Springfield Virginia, USA. 2020*. 2020.

30. Khan, F. and J. Gibbons, *The Physics of Radiation Therapy*. 5th ed. 2014, Philadelphia, PA: Lippincott Williams & Wilkins. 572.

31. Paganetti, H., *Proton Therapy Physics*. 2012, CRC Press: Boca Raton, FL. p. 651.

32. Cherry, S., J. Sorenson, and M. Phelps, *Physics in Nuclear Medicine*. 2012, Elsevier Saunders: Philadelphia, PA. p. 523.

33. Moyers, M.F., et al., *ION STOPPING POWERS AND CT NUMBERS.* Medical Dosimetry, 2010. **35**(3): p. 179-194.

34. Shirazi, S.F.S., et al., *A review on powder-based additive manufacturing for tissue engineering: selective laser sintering and inkjet 3D printing.* Science and Technology of Advanced Materials, 2015. **16**(3): p. 20.

35. Mohan, N., et al., *A review on composite materials and process parameters optimisation for the fused deposition modelling process.* Virtual and Physical Prototyping, 2017. **12**(1): p. 47-59.

36. *Ultimate 3D Printing Materials Guide*. 2020; Available from: https://www.simplify3d.com/support/materials-guide/.

37. Solc, J., T. Vrba, and L. Burianova, *Tissue-equivalence of 3D-printed plastics for medical phantoms in radiology.* Journal of Instrumentation, 2018. **13**: p. 14.

38. Lindsay, C., et al., *3D printed plastics for beam modulation in proton therapy.* Physics in Medicine and Biology, 2015. **60**(11): p. N231-N240.

39. Ricotti, R., et al., *Dosimetric characterization of 3D printed bolus at different infill percentage for external photon beam radiotherapy.* Physica Medica-European Journal of Medical Physics, 2017. **39**: p. 25-32.

40. Meyer, T., et al., *A framework for clinical commissioning of 3D-printed patient support or immobilization devices in photon radiotherapy.* Journal of Applied Clinical Medical Physics, 2018. **19**(5): p. 499-505.

41. Pilipovic, A., P. Raos, and M. Sercer, *Experimental analysis of properties of materials for rapid prototyping.* International Journal of Advanced Manufacturing Technology, 2009. **40**(1-2): p. 105-115.

42. Craft, D.F., et al., *Material matters: Analysis of density uncertainty in 3D printing and its consequences for radiation oncology.* Medical Physics, 2018. **45**(4): p. 1614-1621.

43. Ricotti, R., et al., *3D-printed applicators for high dose rate brachytherapy: Dosimetric assessment at different infill percentage.* Physica Medica-European Journal of Medical Physics, 2016. **32**(12): p. 1698-1706.

44. Madamesila, J., et al., *Characterizing 3D printing in the fabrication of variable density phantoms for quality assurance of radiotherapy.* Physica Medica-European Journal of Medical Physics, 2016. **32**(1): p. 242-247.

45. Dancewicz, O.L., et al., *Radiological properties of 3D printed materials in kilovoltage and megavoltage photon beams.* Physica Medica-European Journal of Medical Physics, 2017. **38**: p. 111-118.

46. *New affordable Fusematic 3D printer from Maker's Tool Works*. 2013 [cited 2019; Available from: https://www.3ders.org/articles/20131225-new-affordable-fusematic-3d-printer-from-maker-tool-works.html.

47. *Artillery Sidewinder X1 3D Printer, 2019 Newest V4 Version Ultra-quiet Lattice Glass Heat Bed Reset Button Filament Runout Sensor & Power Failure Recovery 3D Printing, 300x300x400mm*. [cited 2019; Available from: https://www.amazon.com/Artillery-Sidewinder-Ultra-quiet-Printering-300x300x400mm/dp/B07NRMFL8F/ref=asc_df_B07NRMFL8F/.

48. *Slic3r: Open source 3D printing toolbox*. slic3r.org.

49. Knoll, G., *Radiation Detection and Measurement*. 4th ed. 2010, Hoboken, NJ: John Wiley & Sons, Inc. 830.

50. *Gafchromic™ Dosimetry Media, Type EBT-3*. [cited 2019; Available from: http://www.gafchromic.com/documents/EBT3_Specifications.pdf.

51. *Epson Expression 10000XL-Photo. Epson America, Inc. Long Beach, CA, USA. 2020.*

52. Chan, M.F. *Best Practices with Pradiochromic Film*. in *AAPM Spring Clinical Meeting*. 2015. St. Louis, MO: AAPM.org.

53. *ImageJ: An open platform for scientific image analysis*. [cited 2019; Available from: https://imagej.net/Welcome.

54. Micke, A., D.F. Lewis, and X. Yu, *Multichannel film dosimetry with nonuniformity correction.* Medical Physics, 2011. **38**(5): p. 2523-2534.

55. *Standard Imaging Max 4000. Standard Imaging, Inc. Middleton, WI, USA. 2008.*

56. *Mevion S250i with Hyperscan proton system. Mevion Medical Systems. Littleton, MA. 2020*. Mevion.co.

57. *Detectors For Relative and Absolute Dosimetry*. [cited 2019; Available from: https://www.iba-dosimetry.com/fileadmin/user_upload/products/02_radiation_therapy/_Detectors/Detectors-RD-_-AD_Rev.3_0718_E.pdf.

58. *MP3-M 3D Water Scanning System*. [cited 2020; Available from: https://www.ptwdosimetry.com/en/products/mp1/?type=3451&downloadfile=1282&cHash=78f2467963a26481657b90331b0cf322.

59. *Adaptiiv Medical Technologies Inc. Halifax, NS, Canada. 2020.*

60. Yeo, I.J., et al., *Radiographic film dosimetry of proton beams for depth-dose constancy check and beam profile measurement.* Journal of Applied Clinical Medical Physics, 2015. **16**(3): p. 318-328.

61. van Abbema, J.K., et al., *High accuracy proton relative stopping power measurement.* Nuclear Instruments & Methods in Physics Research Section B-Beam Interactions with Materials and Atoms, 2018. **436**: p. 99-106.

62. Johnson, D., C. Ferreira, and S. Ahmad, *Feasibility of 3D Printed Radiological Equivalent Customizable Tissue Like Materials.* Medical Physics, 2015. **42**(6): p. 3431-3431.

63. Almond, P., Biggs, Peter, Coursey, B.M., Hanson, W.F., Huq, M.,Nath, Ravinder, and Rogers, D.W.O. , *AAPM's TG-51 protocol for clinical reference dosimetry of high-energy photon and electron beams*. 1999: Medical Physics. p. 1847-1870.

Appendix A

Table A.1: Printing parameters and purchasing information for all investigated materials

	Material	Abbreviation	Recommended Printing Temp (°C)	Recommended Bed Temp (°C)	2019 Price ($)/kg	Bed Adhesion
1.	Acrylonitrile Butadiene Styrene	ABS	210 - 250	80 - 110	18.99	Kapton tape/hairspray
2.	Auminum Powder infused PLA	Al Metal	190 - 200	N/A	60	N/A
3.	Algae based PLA	Algae PLA	195 - 210	50	34.99	None
4.	Amphora Polymer	Amphora	220 - 250	60 - 70	59.80	Blue painter's tape
5.	Armadillo Thermoplastic Polyurethane	Armadillo TPU	220 - 230	45	62	Glue/Blue painter's tape
6.	Acrylonitrile Styrene Acrylate	ASA	241 - 260	80 - 100	47	Hairspray
7.	Modified Butadiene	Bendlay	210 - 240	25 - 45	100	Blue painter's tape
8.	N/A	Bio Plastic	180 - 210	0 - 50	40	N/A
9.	High thermal polymer	BluPrint High Heat	265 - 270	95	87.89	N/A
10.	Carbon Fiber Polycarbonate	Carbon Fiber PC	240-260	80-100	48.99	Blue painter's tape
11.	Carbon Fiber reinforced PLA	CF PLA	200 - 220	40-60	60	Blue painter's tape
12.	Cheetah Thermoplastic Polyurethane	Cheetah TPU	235 - 245	40	85	Blue painter's tape, glass
13.	Recycled Chip Bag 80% PP + 20% PE	Chip Bag	210	110	50	N/A
14.	Brass, Bronze, Copper fill infused PLA	ColorFabb MetalFill	200 - 220	40 - 60	73.27	Glass
15.	N/A	ColorFabb nGen	240 - 260	70 - 90	53	Blue painter's tape
16.	Stainless Steel and Steel fill infused PLA	ColorFabb SteelFill	190 - 210	25 - 45	73 - 100	Blue painter's tape
17.	Conductive Carbon PLA	Conductive PLA	225 - 260	90 - 110	120	Kapton tape/hairspray
18.	Metal	Copper	195 - 220	50	25.69	Blue painter's tape
19.	Styrene-Butadiene Copolymer	Crystal Flex	215 - 240	70 - 90	90	N/A
20.	30% Cork-filled PLA	EasyCork	210 - 260	60	85.90	Blue painter's tape
21.	N/A	ETHY-LAY	150 - 170	40 - 60	350	Kapton tape/hairspray
22.	Polycaprolactone homopolymer	Facilan PCL 100	130 - 170	30 - 45	140	PEI sheets

Table A.1 continued

	Material	Abbreviation	Recommended Printing Temp (°C)	Recommended Bed Temp (°C)	2019 Price ($)/kg	Bed Adhesion
23.	Glow In The Dark PLA	GITD	185 - 205	70	28.19	Blue painter's tape
24.	Glass + PLA	Glass-Filled PLA	190 - 210	40	80	N/A
25.	Modified PETG with metallic particles	HDglass	215 - 240	None	59.93	Blue painter's tape
26.	PLA + 10% Hemp Fibers	Hemp	180 - 210	45 - 60	92	Blue painter's tape/hairspray
27.	N/A	HIGH-T-LAY	230 - 250	40 - 60	160	Kapton tape/hairspray
28.	High Impact Polystyrene	HIPS	220 - 240	90-115	20.95	Kapton tape/hairspray
29.	Various metal composites + HTPLA	HTPLA	185 - 215	40 - 60	140	Blue painter's tape/hairspray
30.	N/A	HydroPro	N/A	N/A	175	N/A
31.	N/A	LAY-CLOUD	230 - 250	40 - 60	160	Kapton tape/hairspray
32.	N/A	LAYaPVA	220 - 240	45 - 65	160	Kapton tape/hairspray
33.	Embedded Ceramic	LAYCeramic	255 - 275	25 - 45	200	Blue painter's tape
34.	Composite Iron PLA	Magnetic Iron	185	20 - 55	80	Blue painter's tape
35.	Magnetic Iron infused PLA	Magnetic Iron PLA	190 - 210	25 - 45	70	Blue painter's tape
36.	N/A	Moldlay	165 - 185	25 - 45	86.67	Blue painter's tape
37.	Polyurethane	NinjaFlex	225 - 235	40	85	Blue painter's tape, glass
38.	Polyamide	Nylon	210 - 260	60 - 80	55	PVA based glue
39.	Polyamide w/chopped cf strands	NylonX	250 - 270	50 - 70	65.99	PVA based Glue
40.	Polycaprolactone	PCL	70-140	45	45	NA
41.	Nylon + TPE	PCTPE	225 - 245	60 - 80	84.44	Kapton tape/hairspray
42.	Polyether Imide	PEI	350 - 390	120 - 160	280	N/A
43.	Polyethylene Terephthalate	PET	230 - 255	55 - 70	20.99	Blue painter's tape
44.	Polyethylene Terephthalate, G	PETG	235 - 255	50 - 70	24.99	Blue painter's tape
45.	Polyethylene Triethylene Terephthalate	PETT	210 - 230	45	65.12	Blue painter's tape
46.	Polylactic Acid	PLA	190 - 230	60 - 80	18.99	Blue painter's tape/hairspray
47.	Rubber-elastomeric polymer + PVA	PORO-LAY Series	210 - 230	40 - 60	160	Blue painter's tape
48.	PolyPropylene	PP	235 - 265	100 - 120	91	Packing tape
49.	Polyphenylene ether + Polystyrene	PPEPS	285 - 330	85 - 110	99.95	NA
50.	Polyvinyl Alcohol	PVA	180 - 230	45	80	Blue painter's tape

Table A.1 continued

	Material	Abbreviation	Recommended Printing Temp (°C)	Recommended Bed Temp (°C)	2019 Price ($)/kg	Bed Adhesion
51.	PLA + polyester	Silky PLA	200 - 220	N/A	25.69	Blue painter's tape
52.	Sandstone	SS	165 - 210	20 - 55	34.99	Blue painter's tape
53.	Glitter Flake HTPLA	Stardust	190 - 230	60 - 80	79.90	Blue painter's tape
54.	Co-polymer	T-glase	235 - 242	up to 68-80	79.20	N/A
55.	ThermoPlastic Elastomer	TPE	210 - 230	20 - 40	84.99	Blue painter's tape
56.	Thermoplastic Polyurethane	TPU	240 - 260	40 - 60	21.99	Blue painter's tape
57.	Wood particles in PLA	Wood PLA	200 - 260	90 - 110	34.99	Blue painter's tape
58.	PLA + coffee waste byproducts	Wound Up Coffee	190 - 230	60 - 80	80	N/A
59.	PETG + Fiberglass fillings	Z-Glass	N/A	N/A	62.50	N/A
60.	Marble PLA	Z-Marble PLA	180 - 220	60 - 80?	39.95	NA
61.	Gypsum infused PLA	Z-PLA Pro	N/A	N/A	69	N/A

Table A.2: Manufacturer and place to buy each investigated material.

	Abbrev.	Manufacturer	Buy
1.	ABS	Hatchbox	https://www.amazon.com/gp/product/B00J0H8EWA/ref=as_li_tl?ie=UTF8&camp=1789&creative=9325&creativeASIN=B00J0H8EWA&linkCode=as2&tag=3dprint03-20&linkId=0c87a16b94bf01d2dfa0395138baebd2
2.	Al Metal	SainSmart	https://www.amazon.com/SainSmart-Aluminum-Metal-Filament-Printing/dp/B017SGCX2G/
3.	Algae PLA	3DPrintLife	https://www.3dprintlife.com/http/www3dprintlifecom/filaments/alga
4.	Amphora	Nexeo	https://www.amazon.com/gp/product/B074FVXWVG/ref=as_li_tl?ie=UTF8&camp=1789&creative=9325&creativeASIN=B074FVXWVG&linkCode=as2&tag=3dprint03-20&linkId=d57bcc9f2ae793418d36be72a6dfb5b5
5.	Armadillo TPU	NinjaTek	https://www.amazon.com/NinjaTek-3DAR01117505-Armadillo-Filament-Midnight/dp/B078JG4665/ref=sr_1_3?s=industrial&ie=UTF8&qid=1549654014&sr=1-3&keywords=armadillo+filament+1.75
6.	ASA	Fillamentum	https://www.matterhackers.com/store/l/fillamentum-black-asa-filament-175mm/sk/ML3TU6C3
7.	Bendlay	GO-3D Print	https://www.matterhackers.com/store/l/175mm-bendlay-threequarter-kg/sk/M8VRWE8Y
8.	Bio Plastic	Biome 3D	http://3domfilaments.com/product/biome3d-natural/
9.	BluPrint High Heat	Taulman3D	https://filaments.ca/products/bluprint-high-heat-deflection-clear-1-75mm
10.	Carbon Fiber PC	Priline	https://www.amazon.com/gp/product/B074DS3986/ref=as_li_tl?ie=UTF8&camp=1789&creative=9325&creativeASIN=B074DS3986&linkCode=as2&tag=3dprint03-20&linkId=4786660d93afb1a27ed7dad277770934
11.	CF PLA	Proto-Pasta	https://www.matterhackers.com/store/l/proto-pasta-carbon-fiber-reinforced-pla-175mm-075-kg/sk/MHT446R5
12.	Cheetah TPU	Ninjatek	https://filaments.ca/products/cheetah-filament-fire-red-1-75mm
13.	Chip Bag	3D Brooklyn	https://3dbrooklyn.com/shop/3dbk-filament
14.	ColorFabb MetalFill	ColorFabb	https://www.matterhackers.com/s/store?q=ColorFabb Metal

Table A.2 continued

	Abbrev.	Manufacturer	Buy
15.	ColorFabb nGen	ColorFabb	https://www.matterhackers.com/store/l/colorfabb-white-ngen-filament-1.75mm/sk/MZST1X6W
16.	ColorFabb SteelFill	ColorFabb	https://www.matterhackers.com/s/store?q=Steel Filament
17.	Conductive PLA	Proto-Pasta	https://www.amazon.com/gp/product/B01BDL4BY0/ref=as_li_tl?ie=UTF8&camp=1789&creative=9325&creativeASIN=B01BDL4BY0&linkCode=as2&tag=3dprint03-20&linkId=ec52a1a3a1edd43a280e331b23e702c3
18.	Copper	CC3D	https://www.amazon.com/gp/product/B0761PMW3X/ref=as_li_tl?ie=UTF8&camp=1789&creative=9325&creativeASIN=B0761PMW3X&linkCode=as2&tag=3dprint03-20&linkId=5a0787a2abd6fb14226b775770cf0515
19.	Crystal Flex	Formfutura	https://filaments.ca/products/crystalflex-clear-1-75mm?variant=27874867592
20.	EasyCork	Formfutura	https://filaments.ca/products/easycork-cork-filament-1-75mm
21.	ETHY-LAY	LAY-AWAY	https://www.matterhackers.com/store/l/lay-away-ethy-lay-support-filament-1.75mm/sk/MNQSU7M8
22.	Facilan PCL 100	3D4Makers	https://www.3d4makers.com/products/facilan-pcl-100-filament?variant=9645064716335
23.	GITD	Hatchbox	https://www.amazon.com/gp/product/B00M0CS73S/ref=as_li_tl?ie=UTF8&camp=1789&creative=9325&creativeASIN=B00M0CS73S&linkCode=as2&tag=3dprint03-20&linkId=00f06f8b02ff0318b0f366844c0ba8e3
24.	Glass-Filled PLA	3D-Fuel	https://www.3dfuel.com/collections/c2renew-composites/products/glass-filled-pla
25.	HDglass	Formfutura	https://filaments.ca/products/hdglass-filament-pastel-purple-1-75mm?variant=12899966484533
26.	Hemp	Entwined	https://www.3dfuel.com/collections/c2renew-composites/products/entwined-hemp-filament
27.	HIGH-T-LAY	LAY-AWAY	https://www.matterhackers.com/store/l/lay-away-high-t-lay-support-filament-1.75mm/sk/MWNXY717
28.	HIPS	Gizmo Dorks	https://www.amazon.com/Gizmo-Dorks-1-75mm-Filament-Printers/dp/B00GU2O062?SubscriptionId=AKIAI67BV4ZPUTAKVXIQ&tag=3dpri0ca-20&linkCode=xm2&camp=2025&creative=165953&creativeASIN=B00GU2O062
29.	HTPLA		https://filaments.ca/search?q=htpla
30.	HydroPro	3DFuel	https://www.matterhackers.com/store/l/3dfuel-hydropro-support-filament-175mm-1kg/sk/MV4XV6QV
31.	LAY-CLOUD	LAY-AWAY	https://www.matterhackers.com/store/l/lay-away-lay-cloud-support-filament-1.75mm/sk/MSSU98N2
32.	LAYaPVA	LAY-AWAY	https://www.matterhackers.com/store/l/lay-away-layapva-support-filament-1.75mm/sk/MSXU1VJH
33.	LAYCeramic	LAY-AWAY	https://www.matterhackers.com/store/l/layceramic-3.00mm/sk/M7RE5J6P
34.	Magnetic Iron	Proto-Pasta	https://www.amazon.com/gp/product/B00X8BQYPS/ref=as_li_tl?ie=UTF8&camp=1789&creative=9325&creativeASIN=B00X8BQYPS&linkCode=as2&tag=3dprint03-20&linkId=98d2c31062cd37f8ab3a6388d339b09b
35.	Magnetic Iron PLA	Proto-Pasta	https://www.matterhackers.com/store/l/proto-pasta-magnetic-iron-pla/sk/M7N0SC63
36.	Moldlay	GO-3D Print	https://www.matterhackers.com/store/l/moldlay-filament-1.75mm/sk/MFN5WDLE
37.	NinjaFlex	Ninjatek	https://filaments.ca/products/ninjaflex-filament-fire-red-1-75mm
38.	Nylon	Filabot	https://www.amazon.com/gp/product/B00QRR1VIK/ref=as_li_tl?ie=UTF8&camp=1789&creative=9325&creativeASIN=B00QRR1VIK&linkCode=as2&tag=3dprint03-20&linkId=5e345e9ab5281d1f43f01d6023af8f27
39.	NylonX	MatterHackers	https://www.matterhackers.com/store/l/nylonx-carbon-fiber-nylon-filament-1.75mm/sk/MD5LDGS7

Table A.2 continued

	Abbrev.	Manufacturer	Buy
40.	PCL	Filaments.CA	https://filaments.ca/products/pcl-low-temperature-filament-natural-1-75mm
41.	PCTPE	Taulman	https://www.matterhackers.com/store/l/taulman-pctpe-1.75mm/sk/MEYNNL3D
42.	PEI	3D4Makers	https://www.3d4makers.com/collections/pei-filament-collection
43.	PET	Hatchbox	https://www.amazon.com/gp/product/B014VM9724/ref=as_li_tl?ie=UTF8&camp=1789&creative=9325&creativeASIN=B014VM9724&linkCode=as2&tag=3dprint03-20&linkId=14d1ab94d196e60b3859eb65defaa84c
44.	PETG	MH Build	https://www.matterhackers.com/store/l/petg-blue-translucent-filament-1.75mm/sk/MN0LWWS4
45.	PETT	Taulman 3D	https://www.amazon.com/gp/product/B01F954CHM/ref=as_li_tl?ie=UTF8&camp=1789&creative=9325&creativeASIN=B01F954CHM&linkCode=as2&tag=3dprint03-20&linkId=0e18456ddb762d6931965126989e6ba0
46.	PLA	Hatchbox	https://www.amazon.com/gp/product/B00J0GMMP6/ref=as_li_tl?ie=UTF8&camp=1789&creative=9325&creativeASIN=B00J0GMMP6&linkCode=as2&tag=3dprint03-20&linkId=5b68b3c12e4d526a5eadce64e003fac9
47.	PORO-LAY Series	LAY-AWAY	https://www.matterhackers.com/store/l/poro-lay-gel-lay-porous-filament-175mm/sk/MG1STLN5
48.	PP	Verbatim	https://www.amazon.com/Verbatim-Polypropylene-Filament-Natural-55950-x/dp/B01MRD78UM/ref=sr_1_1?s=industrial&ie=UTF8&qid=1549653724&sr=1-1&keywords=polypropylene+filament
49.	PPEPS	Taulman3D	https://filaments.ca/products/taulman3d-ppeps-filament-black-1-75mm
50.	PVA	eSUN	https://www.amazon.com/gp/product/B00MVIQASU/ref=as_li_tl?ie=UTF8&camp=1789&creative=9325&creativeASIN=B00MVIQASU&linkCode=as2&tag=3dprint03-20&linkId=e62a0ce6c5b5bad77572fd76e0b2c920
51.	Silky PLA	CC3D	https://www.amazon.com/Silk-Silver-Filament-Printting-Materials/dp/B06XSBFB17
52.	SS	3D Printlife	https://www.amazon.com/gp/product/B01M3NQCID/ref=as_li_tl?ie=UTF8&camp=1789&creative=9325&creativeASIN=B01M3NQCID&linkCode=as2&tag=3dprint03-20&linkId=c8458ab9678f9ebd929a81c1a0f430f3
53.	Stardust	Proto-Pasta	https://filaments.ca/products/glitter-flake-high-temp-pla-stardust-1-75mm
54.	T-glase	Taulman	https://www.matterhackers.com/store/3d-printer-filament/taulman-clear-t-glase-175mm
55.	TPE	Dupont Hytrel	https://www.matterhackers.com/store/l/dupont-hytrel-3d-filament-175mm-3d4100fl-nc010-60d/sk/M3RW62CE
56.	TPU	YOYI	https://www.amazon.com/gp/product/B01MAWJOWJ/ref=as_li_tl?ie=UTF8&camp=1789&creative=9325&creativeASIN=B01MAWJOWJ&linkCode=as2&tag=3dprint03-20&linkId=331732e752f6f934751acdbf79c9f5f9
57.	Wood PLA	Hatchbox	https://www.amazon.com/gp/product/B01092XXD4/ref=as_li_tl?ie=UTF8&camp=1789&creative=9325&creativeASIN=B01092XXD4&linkCode=as2&tag=3dprint03-20&linkId=11dbd75a40425aea1749cb21cd8c5eb2
58.	Wound Up Coffee	3D-Fuel	https://www.3dfuel.com/collections/c2renew-composites/products/wound-coffee-filled-filament
59.	Z-Glass	Zortrax	https://store.zortrax.com/us/materials/m200-z-glass
60.	Z-Marble PLA	Ziro	https://filaments.ca/products/z-marble-pla-filament-1-75mm
61.	Z-PLA Pro	Zortrax	https://store.zortrax.com/us/materials/zortrax-m200-z-pla-pro?gclid=Cj0KCQiAnY_jBRDdARIsAIEqpJ2jri09EomMyK11mmxKvrery-SKM-ArplJqFEdm0dZZI45KssXmFKAaAquYEALw_wcB

Appendix B

HU Calculations

Example 1: ABS

$$\overline{HU}_{ABS} = \frac{1}{16}[(-353.703) + (-378.075) + (-342.534) + (-427.646) + (-316.939) + (-355.529) + (-339.882) + (-346.143) + (-364.185) + (-379.644) + (-366.486) + (-380..990) + (-381.400) + (-394.055) + (-348.053) + (-335.355)] = -363.164$$

$$\sigma_{\overline{HU}_{ABS}} = \sqrt{\frac{1}{16}[\left(-353.703 + (-363.164)\right)^2 + \left(-378.075 + (-363.164)\right)^2 + \left(-342.534 + (-363.164)\right)^2 + \left(-427.646 + (-363.164)\right)^2 + \left(-316.939 + (-363.164)\right)^2 + \left(-355.529 + (-363.164)\right)^2 + \left(-339.882 + (-363.164)\right)^2 + \left(-346.143 + (-363.164)\right)^2 + \left(-364.185 + (-363.164)\right)^2 + \left(-379.644 + (-363.164)\right)^2 + \left(-366.486 + (-363.164)\right)^2 + \left(-380.990 + (-363.164)\right)^2 + \left(-381.400 + (-363.164)\right)^2 + \left(-394.055 + (-363.164)\right)^2 + \left(-348.053 + (-363.164)\right)^2 + \left(-335.355 + (-363.164)\right)^2} = 26.8479$$

Film Calculations

Example 2: Red Channel, 15 Gy, Calibration Curve

$$P_{norm,15\ Gy} = 2^{16} - 39192.337 = 26343.663$$

$$P_{final,D_{15\ Gy}} = 26343.663 - 24089.327 = 2254.3357$$

$$D_{cal} = \left(-\frac{58615310275522600 - (322204126629000\ x\ 2254.3357)}{56258887832507700 - (1435381496850\ x\ 2254.3357)}\right)^{1.07155832225439}$$

$$= 15.0962\ Gy$$

$$\sigma_{P_{final,15\ Gy}} = \sqrt{(158.138)^2 + (141.2106155)^2} = 212.00959$$

$$\sigma_{15\ Gy} =$$

$$\sqrt{1.07155832225439\left[\frac{1435381496850\left((322204126629000\ x\ 2254.3357)-58615310275522600\right)}{\left(56258887832507700\ -(1435381496850\ x\ 2254.3357)\right)^2}+\cdots\right.}$$

$$\left.\cdots+\frac{322204126629000}{\left(56258887832507700\ -(1435381496850\ x\ 2254.3357)\right)}\right]^2\cdots$$

$$\cdots\left(\left[\frac{\left((322204126629000\ x\ 2254.3357)-58615310275522600\right)}{\left(56258887832507700\ -(d\ x\ 2254.3357)\right)}\right]^{1.07155832225439-1}\right)^2 212.00959^2+\cdots$$

$$\cdots+\left(\left[\frac{(322204126629000\ x\ 2254.3357)-58615310275522600}{\left(56258887832507700\ -(1435381496850\ x\ 2254.3357)\right)}\right]^{1.07155832225439}\right)^2\cdots$$

$$\cdots\left(\log\left|\frac{(322204126629000\ x\ 2254.3357)-58615310275522600}{\left(56258887832507700\ -(1435381496850\ x\ 2254.3357)\right)}\right|\right)^2 0.006270516^2=1.7843432$$

Example 3: PLA, 9 MeV, 19.812 mm (d_{max})

$$P_{norm,1}=\ 2^{16}-24940=40596$$

$$\bar{P}_{19.812\ mm}=\frac{1}{15}(40596+40687+40511+40523+40548+34767+40571+40587$$

$$+40593+40543+40588+40518+40609+40490+40460)=40173$$

$$P_{final,19.812\ mm}=\ 40173-23086=17087$$

$$D_{red,19.812\ mm}$$

$$=\ \left(-\frac{58615310275522600\ -(322204126629000\ x\ 17087)}{56258887832507700\ -(1435381496850\ x\ 17087)}\right)^{1.07155832225439}$$

$$=248.06\ Gy$$

$$\bar{D}_{19.812\ mm}=\frac{248.06\ Gy+255.08\ Gy+262.07\ Gy}{3}=255.07\ Gy$$

$$PDD_{19.812\ mm}=\frac{255.07\ Gy}{255.07\ Gy}\ x\ 100=100\%$$

$$\sigma_{\bar{P}_{19.812\ mm}}$$

$$= \sqrt{\frac{1}{15}[(40596-40173)^2+(40687-40173)^2+(40511-40173)^2+(40523-40173)^2}$$

$$\overline{+(40548-40173)^2+(34767-40173)^2+(40571-40173)^2+(40587-40173)^2}$$

$$\overline{+(40593-40173)^2+(40543-40173)^2+(40588-40173)^2+(40518-40173)^2}$$

$$\overline{+(40609-40173)^2+(40490-40173)^2+(40490-40173)^2+(40460-40173)^2]}$$

$$= 1496.6255$$

$$\sigma_{P_{final,19.812\ mm}} = \sqrt{(1496.6)^2 + (141.21)^2} = 1503.3$$

$$\sigma_{D_{red},19.812\ mm} =$$

$$\sqrt{1.07155832225439\left[\frac{1435381496850\left((322204126629000\ x\ 17087)-58615310275522600\right)}{\left(56258887832507700\ -(1435381496850\ x\ 17087)\right)^2}+\cdots\right.}$$

$$\overline{\left.\cdots+\frac{322204126629000}{\left(56258887832507700\ -(1435381496850\ x\ 17087)\right)}\right]^2\cdots}$$

$$\overline{\cdots\left(\left[\frac{\left((322204126629000\ x\ 17087)-58615310275522600\right)}{\left(56258887832507700\ -(d\ x\ 17087)\right)}\right]^{1.07155832225439-1}\right)^2 1503.3^2+\cdots}$$

$$\overline{\cdots+\left(\left[\frac{(322204126629000\ x\ 17087)-58615310275522600}{\left(56258887832507700\ -(1435381496850\ x\ 17087)\right)}\right]^{1.07155832225439}\right)^2\cdots}$$

$$\overline{\cdots\left(\log\left|\frac{(322204126629000\ x\ 17087)-58615310275522600}{\left(56258887832507700\ -(1435381496850\ x\ 17087)\right)}\right|\right)^2 0.006270516^2 = 41.673\ Gy}$$

$$\sigma_{\bar{D}_{19.812\ mm}} = \sqrt{\left(\frac{1}{3}\right)^2(41.673\ Gy)^2+\left(\frac{1}{3}\right)^2(3.8305\ Gy)^2+\left(\frac{1}{3}\right)^2(6.9063\ Gy)^2} = 14.138\ Gy$$

$$\sigma_{PDD_{19.812\ mm}} = 100\%\sqrt{\left(\frac{14.138\ Gy}{255.07\ Gy}\right)^2+\left(\frac{14.138\ Gy}{255.07\ Gy}\right)^2} = 7.8388\%$$

Photon Calculations

Example 4: Algae PLA, 6 MV

$$\bar{M}_{Algae\ PLA,2cm} = \frac{1}{3}(686.03\ nC + 686.5\ nC + 686.02\ nC) = 686.18\ nC$$

$$TMR_{2cm} = \frac{686.18\ nC}{705.75\ nC} = 0.97228$$

$$\%\ Difference = \frac{705.75\ nC - 686.18\ nC}{705.75\ nC} = 2.772\ nC$$

$$\sigma_{M_1} = 0.013\ x\ 686.03\ nC = 8.9184\ nC$$

$$\sigma_{\bar{M}_{Algae\ PLA,2cm}} = \sqrt{\left(\frac{1}{3}\right)^2 (8.9184\ nC)^2 + \left(\frac{1}{3}\right)^2 (8.9245\ nC)^2 + \left(\frac{1}{3}\right)^2 (8.9183\ nC)^2}$$

$$= 5.1502\ nC$$

$$\sigma_{TMR_{2cm}} = 0.97228\sqrt{\left(\frac{5.1502\ nC}{686.18\ nC}\right)^2 + \left(\frac{9.1748\ nC}{705.75\ nC}\right)^2} = 0.014595\ nC$$

$$\sigma_{Diff} = \sqrt{(9.1748\ nC)^2 + (5.1502\ nC)^2} = 10.521\ nC$$

$$\sigma_{\%\ Diff} = 2.772\%\sqrt{\left(\frac{10.521\ nC}{19.57\ nC}\right)^2 + \left(\frac{9.1748\ nC}{705.75\ nC}\right)^2} = 1.491\%$$

Proton Calculations

Example 5: Wood PLA, 70.7 MeV

$$\bar{t}_{Wood\ PLA} = \frac{1}{4}(10.31\ mm + 10.33\ mm + 10.27\ mm + 10.27\ mm) = 10.30\ mm$$

$$RSP = \frac{42.6\ mm - 35.3\ mm}{10.295\ mm} = 0.706\ mm$$

$$\sigma_{\bar{t}_{Wood\ PLA}} = \sqrt{\frac{1}{4}[(10.31\ mm - 10.30\ mm)^2 + (10.33\ mm - 10.30\ mm)^2}$$

$$\overline{(10.27\ mm - 10.30\ mm)^2 + (10.27\ mm - 10.30\ mm)^2} = 0.03$$

$$R_{90,Wood\ PLA} = 36\ mm + (0.9 - 0.842)\left(\frac{35\ mm - 36\ mm}{0.929 - 0.842}\right) = 35.3\ mm$$

$$D_{0.842} = \frac{4.37\ nC}{5.19\ nC} = 0.842$$

$$\sigma_D = 0.013(4.37\ nC) = 0.0568\ nC$$

$$\sigma_{D_{0.842}} = 0.842\sqrt{\left(\frac{0.0568\ nC}{4.37\ nC}\right)^2 + \left(\frac{0.06747\ nC}{5.19\ nC}\right)^2} = 0.01548$$

$$\sigma_{R_{90,Wood\ PLA}} =$$

$$\sqrt{\left(\frac{0.842 - 0.9}{0.842 - 35\ mm}\right)^2 0.01^2 + \left(\frac{(0.842 - 0.9)(36\ mm - 0.929)}{0.842 - 35\ mm}\right)^2 0.01^2 + \cdots}$$

$$\overline{\ldots + \left(\frac{(35\ mm - 0.9)(36\ mm - 0.929)}{(0.842 - 35\ mm)^2}\right)^2 0.0155^2 + \left(\frac{35\ mm - 0.9}{35\ mm - 0.842}\right)^2 0.0171^2}$$

$$= 0.207\ mm$$

$$\sigma_{RSP_{Wood\ PLA}} =$$

$$\sqrt{\left(\frac{1}{10.30\ mm}\right)^2 (0.173\ mm)^2 + \left(-\frac{1}{10.30\ mm}\right)^2 (0.207\ mm)^2 + \left(\frac{42.6\ mm - 35.3\ mm}{(10.30\ mm)^2}\right)^2 (0.03\ mm)^2}$$

$$= 0.113\ mm$$

Density Calculations

Example 6: TPU

$$\bar{m}_{TPU,1} = \frac{1}{3}(67.40\ g + 67.50\ g + 67.95\ g) = 67.62\ g$$

$$\bar{m}_{TPU} = \frac{1}{24}(67.40\ g + 67.50\ g + 67.95\ g + 61.50\ g + 61.55\ g + 61.10\ g + 62.90\ g$$

$$+63.20\ g + 62.70\ g + 59.85\ g + 59.70\ g + 59.95\ g + 59.85\ g + 60.00\ g + 59.90\ g$$

$$+63.65\ g + 64.05\ g + 63.40\ g + 62.20\ g + 62.20\ g + 61.90\ g + 65.00\ g + 65.30\ g$$

$$+65.10\ g) = 62.83\ g$$

$$V_{TPU,1} = \pi(20.25cm)^2(0.65\ cm) = 88.95\ cm^3$$

$$\bar{V}_{TPU} = \frac{1}{8}(88.95\ cm^3 + 88.95\ cm^3 + 88.95\ cm^3 + 88.95\ cm^3 + 82.11\ cm^3 + 95.79\ cm^3$$

$$+88.95\ cm^3 + 88.95\ cm^3) = 88.95\ cm^3$$

$$\rho_{TPU,1} = \frac{67.62\ g}{88.95\ cm^3} = 0.7602\ \frac{g}{cm^3}$$

$$\bar{\rho}_{TPU} = \frac{1}{8}(0.7602\ \frac{g}{cm^3} + 0.6901\ \frac{g}{cm^3} + 0.7075\ \frac{g}{cm^3} + 0.6727\ \frac{g}{cm^3} + 0.7297\ \frac{g}{cm^3}$$

$$+0.6650\ \frac{g}{cm^3} + 0.6981\ \frac{g}{cm^3} + 0.7322\ \frac{g}{cm^3}) = 0.7069\ \frac{g}{cm^3}$$

$$\sigma_{TPU,1} = \frac{1}{3}[(67.40\ g - 67.62\ g)^2 + (67.50\ g - 67.62\ g)^2 + (67.95\ g - 67.62\ g)^2]$$

$$= 0.2930\ g$$

$$\sigma_{\bar{m}_{TPU}} = \sqrt{\frac{1}{24}[(67.40g - 62.83\ g)^2 + (67.50\ g - 62.83\ g)^2 + (67.95\ g - 62.83\ g)^2}$$

$$\overline{+(61.50\ g - 62.83\ g)^2 + (61.55\ g - 62.83\ g)^2 + (61.10\ g - 62.83\ g)^2}$$

$$\overline{+(62.90\ g - 62.83\ g)^2 + (63.20\ g - 62.83\ g)^2 + (62.70\ g - 62.83\ g)^2}$$

$$\overline{+(59.85\ g - 62.83\ g)^2 + (59.70\ g - 62.83\ g)^2 + (59.95\ g - 62.83\ g)^2}$$

$$\overline{+(59.85\ g - 62.83\ g)^2 + (60.00\ g - 62.83\ g)^2 + (59.90\ g - 62.83\ g)^2}$$

$$\overline{+(63.65\ g - 40173)^2 + (64.05\ g - 62.83\ g)^2 + (63.04\ g - 62.83\ g)^2}$$

$$\overline{+(62.20\ g - 62.83\ g)^2 + (62.20\ g - 62.83\ g)^2 + (61.90\ g - 62.83\ g)^2}$$

$$\overline{+(65.00\ g - 62.83\ g)^2 + (65.30\ g - 62.83\ g)^2 + (65.10\ g\ - 62.83\ g)^2}$$

$$\overline{+(40490 - 62.83\ g)^2}] = 2.537\ g$$

$$\sigma_{V_{TPU,1}} = \sqrt{\left(2\pi\left(\frac{20.75\ cm}{\pi}\right)(0.65\ cm)\right)^2 (0.025\ cm)^2 + \left(\pi\left(\frac{20.75cm}{\pi}\right)^2\right)^2 (0.05\ cm)^2}$$

$$= 6.875cm^3$$

$$\sigma_{\bar{V}_{TPU}} = \sqrt{\frac{1}{8}[(88.95\ cm^3 - 88.95\ cm^3)^2 + (88.95\ cm^3 - 88.95\ cm^3)^2}$$

$$\overline{+(88.95\ cm^3 - 88.95\ cm^3)^2 + (88.95\ cm^3 - 88.95\ cm^3)^2 + (82.11\ cm^3 - 88.95\ cm^3)^2}$$

$$\overline{+(95.79\ cm^3 - 88.95\ cm^3)^2 + (88.95\ cm^3 - 88.95\ cm^3)^2 + (88.95\ cm^3 - 88.95\ cm^3)^2}$$

$$= 3.657\ cm^3$$

$$\sigma_{\rho_{TPU,1}} = 0.7602\ \frac{g}{cm^3}\sqrt{\left(\frac{0.29297\ g}{67.62\ g}\right)^2 + \left(\frac{6.875\ cm^3}{88.95\ cm^3}\right)^2} = 0.05885\ \frac{g}{cm^3}$$

$$\sigma_{\bar{\rho}_{TPU}} = \sqrt{\frac{1}{8}[\left(0.7602\ \frac{g}{cm^3} - 0.7069\ \frac{g}{cm^3}\right)^2 + \left(0.6901\ \frac{g}{cm^3} - 0.7069\ \frac{g}{cm^3}\right)^2}$$

$$\overline{+\left(0.7075\ \frac{g}{cm^3} - 0.7069\ \frac{g}{cm^3}\right)^2 + \left(0.6727\ \frac{g}{cm^3} - 0.7069\ \frac{g}{cm^3}\right)^2}$$

$$\overline{+\left(0.7297\ \frac{g}{cm^3} - 0.7069\ \frac{g}{cm^3}\right)^2 + \left(0.6650\ \frac{g}{cm^3} - 0.7069\ \frac{g}{cm^3}\right)^2}$$

$$\overline{+\left(0.6981\ \frac{g}{cm^3} - 0.7069\ \frac{g}{cm^3}\right)^2 + \left(0.7322\ \frac{g}{cm^3} - 0.7069\ \frac{g}{cm^3}\right)^2} = 0.03227\ \frac{g}{cm^3}$$